INSTITUTE OF FUNDAMENTAL AND APPLIED RESEARCH

UDC: 530.12:531.51

KHAMIDOV TURSUNALI OLIMJON UGLI

ASTROPHYSICAL PROCESSES AROUND BLACK HOLES IN EXTENDED THEORIES OF GRAVITY

01.04.02 – Theoretical Physics

DISSERTATION OF THE DOCTOR OF PHILOSOPHY (PhD) IN PHYSICS AND MATHEMATICS

Scientific supervisor: Shaymatov Sanjar Ruzimurotovich
doctor of sciences in physics and mathematics

Tashkent – 2025

Contents

Abbreviations

GR	**G**eneral **R**elativity
BH	**B**lack **H**ole
KRZ	**K**onoplya **R**ezzolla **Z**hidenko
AGN	**A**ctive **G**alactic **N**ucleus
EHT	**E**vent **H**orizon **T**elescope
EM	**E**lectro**m**agnetic
ISCO	**I**nnermost **S**table **C**ircular **O**rbit
RN	**R**eissner-**N**ordström
BZ	**B**landford-**Z**najek
Sgr A*	**S**a**g**itta**r**ius **A***
PP	**P**enrose **P**rocess
QPO	**Q**uasi-**P**eriodic **O**scillations
MPP	**M**agnetic **P**enrose **P**rocess
LQG	**L**oop **Q**uantum **G**ravity
LQBH	**L**oop **Q**uantum **B**lack **H**ole
QCBH	**Q**uantum **C**orrected **B**lack **H**ole

Physical constants & other definitions

Speed of Light	$c = 2.998 \times 10^{10}$ cm s^{-1}
Gravitational constant	$G = 6.672 \times 10^{-8}$ cm^3 g^{-1} s^{-2}
Mass of the Sun	$M_\odot = 1.989 \times 10^{33}$ g
Mass of Sgr A*	$M_* = 4.14 \times 10^6 M_\odot = 8.23 \times 10^{39}$ g
Schwarzschild radius of the Sun	$r_S = 2GM_\odot/c^2 = 2.95 \times 10^5$ cm
Schwarzschild radius of Sgr A*	$R_S = 2GM_*/c^2 = 1.22 \times 10^{12}$ cm

1 parsec = 1 pc = 3.26 ly = 3.08×10^{18} cm

1 eV = 1.6×10^{-19}J = 1.6×10^{-12} erg

1 Gauss = 1 G = 10^{-4} T

Introduction

Relevance and necessity of the topic. As gravitational wave astronomy and Event Horizon Telescope observations continue to provide unprecedented views of black holes and their surroundings, the role of quantum effects in black hole dynamics may become increasingly important. These modern observations are crucial for finding new generalized solutions in extended theories of gravity and for investigating issues related to the singularity problem and the quantum nature of spacetime. Additionally, while Einstein's theory of general relativity is a significant and main theory, it does not fully address the unique singularity and dark matter problems of black holes. Therefore, the development of promising alternative theories of gravity, such as loop quantum gravity models, offers promising pathways to better understand these issues that were once thought to be the domain of general relativity alone, as well as to obtain precise constraints on model parameters through astrophysical tests. With this in view, it is increasingly important to explore whether the quantum parameters can leave any observational signatures for the current/or forthcoming observations, so the quantum effects on the black hole spacetime can be directly tested or constrained by observations.

It is important to note that in recent years, our country has been increasingly focused on advancing both fundamental and applied research areas. The advancement of theoretical astrophysical research, a promising field, is particularly important today. The primary areas of fundamental research and development, as well as their practical applications are detailed in the Strategy for the Further Development of the Republic of Uzbekistan for 2022–2026 [1]. The study of the energetics of astrophysical objects remains one of the important issues in the field of fundamental research.

This research aligns with the objectives outlined in the following state regulatory documents: Presidential Decree No. DP-4947 of February 7, 2017, on the Strategy for the Further Development of the Republic of Uzbekistan, and the "Roadmap of Key Structural Reform Directions in Uzbekistan for 2019–2021," issued by the Government of Uzbekistan on November 29, 2018.

Conformity of the research to the main priorities of science and technology development of the Republic. The research has been conducted in line with the priority areas of science and technology in the Republic of Uzbekistan, specifically under the category II: "Power, Energy, and Resource-Saving."

Connection of the topic of the research topic to the scientific works of higher education and research institutions, where the dissertation is carried out. The dissertation was done within the framework of scientific project funded by the Ministry of Innovative Development: FL-7923051796 “Modeling of Scalar Field Dynamics and Quantum Emitters in Spherically Symmetric Gravitational Fields”.

The aim of the research is to develop a theoretical framework for constraining black hole parameters in extended gravity theories using astrophysical processes and high-precision observations.

The tasks of the research:

To investigate the particle motion around parametrized KRZ black hole and determine how its deformation parameters modify innermost stable circular orbit

[1] Decree No. PF-60 of the President of the Republic of Uzbekistan dated January 1, 2022 “On the Development Strategy of New Uzbekistan for 2022-2026”

parameters.

To study how the KRZ deformation parameters affect energy extraction via the MPP.

To estimate the energy of protons escaping through the MPP in a KRZ spacetime and provide an analysis associated with constraints on the BH mass and the strength of the magnetic field.

To analyse how the quantum-correction parameter modifies the horizon, ergosphere, particle dynamics, and MPP efficiency when the LQBH is located in an asymptotically uniform magnetic field.

To estimate the particle-acceleration capability of the LQBH by computing the energy of escaping protons accelerated via the MPP

To constrain the quantum-correction parameter of QCBHs using high-frequency QPOs from X-ray binaries together with the perihelion shifts of Mercury and the S2 star.

The object of the research are astrophysical compact objects, energy extraction mechanisms from astrophysical compact objects, the perihelion shift, QPOs.

The subject of the research are the QCBH, the energetics of LQBH and KRZ black hole, properties of quantum corrections, particle dynamics around astrophysical compact objects, analytical and numerical methods for solving differential equations of the motion of particles.

The methods of the research are the approaches involve theoretical physics and astrophysics, modern methods of theoretical astrophysics and mathematical physics, as well as analytical and numerical techniques for solving differential equations associated with field and particle dynamics.

The scientific novelty of the research is the following:

For the first time, the quantum correction parameter ξ of QCBHs has been constrained as $\xi \leq 0.01869$ from Solar System tests, $\xi \leq 0.73528$ from the orbit of the S2 star around Sgr A*, and $\xi \leq 2.086$ from QPOs observations of X-ray binaries.

For the first time, it has been shown that the efficiency of the MPP for the LQBH is 19.3% (compared to 20.7% for the Kerr case). It was also found that the efficiency of the MPP can exceed 100%, as in the Kerr black hole, and can even surpass 140% for the quantum correction parameter value of $\epsilon = 0.2$.

For the first time, it has been shown that for the quantum correction parameter ϵ of the LQBH, $\epsilon = 0.2$, the energy of an escaping proton from M87* can reach $E_p^{\mathrm{M87}} = 1.89 \times 10^{18}\,\mathrm{eV}$, corresponding to the ankle region of the cosmic-ray spectrum ($10^{18} - 10^{19}\,\mathrm{eV}$).

For the first time, it has been found that the energy efficiency of the MPP for the KRZ black hole approaches $\eta \sim 23.3\%$, which is greater than in the Kerr case.

For the first time, it has been shown that for the deformation parameter of the KRZ black hole, $\delta_2 = 0.2$, the energy of an escaping proton from Sgr A* can reach $E_p^{\mathrm{SgrA*}} = 6.27 \times 10^{15}\,\mathrm{eV}$, corresponding to the knee region of the cosmic-ray spectrum ($10^{15} - 10^{16}\,\mathrm{eV}$).

The practical results of the research are the following:

The upper bounds on the quantum correction parameter ξ of QCBHs have been determined as $\xi \leq 0.01869$ for Solar System tests, $\xi \leq 0.73528$ for Sgr A*, and $\xi \leq 2.086$ in strong gravitational fields.

It has been shown that with an increase in the LQG parameter ϵ, the horizon and the static limit surface shrink, unstable orbits shift inward, and the stable orbit shifts outward. The efficiency of the MPP has been found to be 19.3% (not 20.7% as in the Kerr case) when $\epsilon = 0.3$ and the spin parameter $\alpha = a_{\mathrm{extremal}}$.

The energy of protons accelerated around the KRZ black hole has been found to strongly depend on the external magnetic field B and the deformation parameter δ_2. For $\delta_2 = 0.2$, the proton energy for Sgr A* reaches $E_p^{\mathrm{SgrA}*} = 6.27 \times 10^{15}\,\mathrm{eV}$. This corresponds to the knee energy region of the cosmic-ray spectrum: $10^{15} - 10^{16}\,\mathrm{eV}$.

The reliability of the research results is supported by the use of standard mathematical and theoretical physics methods in the dissertation, including modern methods of relativistic astrophysics, highly effective numerical methods and software. The results were derived strictly within the mathematical framework of general relativity and theoretical physics. Modern numerical and analytical calculation methods are also applied, with results compared to existing observational data and findings from other researchers. The structured conclusions of the dissertation align with the fundamental principles of astrophysics concerning compact objects.

The scientific and practical significance of the research results.

The scientific significance of the research results is that the development of promising alternative theories (e.g., loop quantum gravity) offers a fundamental understanding of unique singularity problems and quantum aspects of spacetime at microscopic scales.

The practical significance of the research results is that our proposed model in the dissertation may provide new insights into the role of the quantum correction parameter in quantum corrected black holes and advance our understanding of quantum gravitational phenomena.

Implementation of the research results.

The findings presented in this dissertation—particularly those concerning the energetics of compact astrophysical objects—have attracted attention from international researchers and have been cited in peer-reviewed journals with high impact factors: Physics Letters B, Volume 864, article id. 139398 Web-Sc, IF: 4.3, The European Physical Journal C, Volume 85, article number 26, (2025), Web-Sc, IF: 4.2, The European Physical Journal C, Volume 85, article number 725, (2025), Web-Sc, IF: 4.2, The European Physical Journal C, Volume 85, № 726, (2025), Web-Sc, IF: 4.2.

These scientific results were used within the framework of programs supported by the Vellore Institute of Technology (based on an official letter provided by Dr. Pankaj Sheoran).

Volume and structure of the dissertation.

The dissertation consists of an introduction, three chapters, conclusion and a bibliography. The size of the dissertation is 106 pages.

Approbation of the research results

The dissertation results have been discussed in 2 international and 2 local conferences.

List of published papers [1–5].

Part I.

1. Xamidov T., Shaymatov S., Sheoran P., Ahmedov B., Astrophysical insights into magnetic Penrose process around parameterized Konoplya–Rezzolla–Zhidenko black hole // The European Physical Journal C, Volume 84, article number 1300, (2024) (№1 Web of Science, IF: 4.2).

2. Xamidov T., Sheoran P., Shaymatov S., Zhu T., Energy extraction from Loop Quantum Black Holes: the role of magnetic Penrose process and quantum gravity effects with astrophysical insights // Journal of Cosmology and Astroparticle Physics, Volume 2025, article id. 03(2025)053 (№1 Web of Science, IF: 5.3).

3. Xamidov T., Uktamov U., Shaymatov S., Ahmedov B., Quasiperiodic oscillations around a Schwarzschild black hole surrounded by a Dehnen type dark

matter halo // Physics of the Dark Universe, Volume 47, article id. 101805 (2025) (№1 Web of Science, IF: 5.0).

4. Xamidov T., Alloqulov M., Shaymatov S., Electric Penrose process and collisions of particles near five-dimensional weakly charged Schwarzschild black hole // The European Physical Journal Plus, Volume 140, article number 182, (2025) (№1 Web of Science, IF: 2.8).

5. Xamidov T., Shaymatov S., Wu Q., Zhu T., Probing the Schwarzschild black hole immersed in a dark matter halo through astrophysical tests // The European Physical Journal C, Volume 85, article number 1193, (2025) (№1 Web of Science, IF: 4.2),//

Part II.

6. Xamidov T., "Probing quantum corrected black hole through solar system tests", Fundamental and Applied Research in Physics, NUUz, May 16-17, 2025, p. 94-95.

7. Lutfulloyev Sh., Xamidov T., "Kvant tuzatilgan qora oʻralarda kvazi-davriy tebranishlar", Fundamental and Applied Research in Physics, NUUz, May 16-17, 2025, p.130-131.

Chapter I

Probing black holes in loop quantum gravity

1.1 Introduction

Albert Einstein's theory of GR revolutionized our understanding of space and time by showing that gravity arises from the curvature of spacetime [6]. This framework provides a robust foundation for describing the macroscopic structure of BHs, successfully explaining phenomena such as the event horizon, gravitational waves [7, 8], and the imaging of the supermassive BHs at the center of the M87* [9, 10] and SgrA* [11, 12] galaxy. The direct detection of gravitational waves, along with the observation and analysis of the supermassive BH image through these instruments, provides explanations for astrophysical phenomena in a strong gravitational field regime. Furthermore, GR explains effects that Newtonian mechanics cannot, including the bending of light by massive objects, the perihelion precession of Mercury, and gravitational redshift. However, despite its success in explaining large-scale gravity, GR cannot describe the quantum nature of spacetime at microscopic scales. This limitation leaves fundamental questions unanswered. Although GR is a significant and main theory, it does not fully address singularity problems and quantum aspects of spacetime at microscopic scales [13]. Therefore, testing is required for the development of promising alternative theories that offer a fundamental understanding of these issues.

One of the main open problems is the existence of spacetime singularities [14, 15], which pose a fundamental challenge to classical . A promising way to address this issue involves modifying BH solutions to include quantum effects. A particularly notable framework for such modifications is the Hamiltonian constraints approach [16, 17], which has played a significant role in the canonical quantization of GR. Using the Hamiltonian formulation, two BH models were introduced in [18] to address an issue related to general covariance in spherically symmetric gravity, which arises when canonical quantum gravity is applied to develop a semiclassical BH model. These two models differ in their choice of a quantum parameter.

While the above considerations focus on quantum-corrected BH models derived from the Hamiltonian constraints approach, it is equally important to examine other approaches that aim to incorporate quantum effects into BH spacetimes.

Another prominent framework for quantum gravity is LQG. As one of the leading approaches in the field, LQG postulates that spacetime is discrete at the Planck scale, consisting of quantized loops of gravitational fields. LQG modifies the classical description of BHs by introducing quantum corrections to their internal structure [19–21]. These corrections affect the geometry near the event horizon and the singularity, offering the possibility of a *regularized* BH [22–24] that avoids the classical singularity problem.

One such effective quantum BH, which is derived from the mini-superspace approach in quantizing the Schwarzschild BH spacetime using the polymerization procedure in LQG, was explored in Ref. [25]. This LQBH has no curvature singularity and its regularity is determined by two parameters arising from LQG: the polymeric parameter (δ) and the Barbero-Immirzi parameter γ [26, 27]. This LQBH is also known as a self-dual BH since it exhibits a T-duality symmetry (for details see, e.g., Refs. [26,27]). The introduction of parameters such as the Immirzi parameter (γ) and the polymeric parameter (δ) within LQG [28, 29] offers a novel framework for understanding the dynamical behavior of BHs, including their mass, spin, and magnetic properties. The corresponding rotating LQBH was obtained in Ref. [30] using the modified Newman-Janis procedure. It is interesting to explore the quantum effects of LQBH in a wide range of astrophysical environments, see Refs. [27, 30–40] and references therein.

The detection of gravitational waves and the imaging of the supermassive BHs at the centers of M87* and SgrA* are pivotal. Therefore, these observations are crucial not only for discovering new solutions in alternative theories of gravity but also for rigorously testing GR in the strong field regime and exploring various gravity theories through precise measurements of spacetime geometry parameters. High-frequency QPOs in X-ray flux from BHs and neutron stars in X-ray binaries offer another promising avenue for testing gravity near BHs. Detected as narrow peaks in power density spectra, these QPOs originate within a few gravitational radii of the central object, depending solely on spacetime geometry and orbital radius. Analyzing QPOs in X-ray data from BH accretion disks [41] can thus reveal valuable insights into spacetime geometry within different gravity theories [42–44]. QPOs provide a powerful probe of astrophysical BH candidates in strong gravitational fields, offering valuable insights into the innermost regions of accretion disks and the masses, radii, and spin periods of white dwarfs, neutron stars, and BHs.

It is important to explore whether the quantum parameters can leave any observational signatures for the current/or forthcoming observations, so the quantum effect on the BH spacetime can be directly tested or constrained by observations. With this motivation, several observational or phenomenological implications of the QCBH spacetime have already been investigated [45, 45–55]. In particular, the light ring and BH shadow are useful for estimating BH parameters, including mass, spin, the surrounding external field, and other physical properties. By analyzing the shadows of M87* and SgrA*, constraints on the quantum correction parameter ξ have been established [45, 46]. In addition, the quasinormal modes of the QCBH have also been explored in [45, 47].

Throughout this dissertation, we use a spacetime metric signature $(-, +, +, +)$ and adopt geometric units with $G = c = 1$.

1.2 Exploring quantum corrected black hole through astrophysical tests

1.2.1 The Spacetime metric and timelike geodesics

In the Hamiltonian formulation of GR, the dynamics are governed by two sets of constraints: the diffeomorphism constraint and the Hamiltonian constraint. The diffeomorphism constraint generates spatial coordinate transformations on each hypersurface, thereby preserving spatial diffeomorphism invariance, while the Hamiltonian constraint governs the evolution of spatial geometry in "time" and ensures the preservation of general covariance. Recently, the problem of maintaining general covariance in spherically symmetric gravity was examined in Ref. [18], particularly in the construction of semiclassical black hole models from canonical quantum gravity. The analysis preserves the kinematical structure of spherically symmetric GR. The study assumes that the classical diffeomorphism constraint remains unchanged, while introducing an effective Hamiltonian constraint, H_{eff}, along with an arbitrary function that defines the effective metric. The effective Hamiltonian is defined as follows [18]

$$\begin{aligned} H_{\text{eff}} = & -\frac{E^2}{2\sqrt{E^1}} - \frac{K_1 E^1}{2\xi} \sin\left(\frac{2\xi K_2}{\sqrt{E^1}}\right) - \frac{3\sqrt{E^1}E^2}{2\xi^2} \sin^2\left(\frac{\xi K_2}{\sqrt{E^1}}\right) \\ & + \frac{K_2 E^2}{2\xi} \sin\left(\frac{2\xi K_2}{\sqrt{E^1}}\right) + \frac{(\partial_x E^1)^2}{8\sqrt{E^1}E^2} e^{\frac{2i\xi K_2}{\sqrt{E^1}}} + \frac{\sqrt{E^1}}{2} \partial_x \left(\frac{\partial_x E^1}{E^2}\right) e^{\frac{2i\xi K_2}{\sqrt{E^1}}} \\ & + \frac{i\xi E^2}{4} \left(\frac{\partial_x E^1}{E^2}\right)^2 \left(\frac{K_1}{E^2} - \frac{K_2}{E^1}\right) e^{\frac{2i\xi K_2}{\sqrt{E^1}}}, \end{aligned} \tag{1.1}$$

where E^1 and E^2 are the densitized triad components encoding the spatial geometry, while K_1 and K_2 are their conjugate extrinsic-curvature variables. The parameter ξ is the quantum correction parameter. The effective Hamiltonian constraint deviates from the classical form due to quantum gravity effects.The constraint algebra is assumed to remain the same as in the classical case, but with an additional correction factor μ that represents quantum gravity effects. As in the classical case, the existence of a Dirac observable associated with the black hole mass is assumed. Based on these assumptions, the authors set up conditions for this observable and derive the corresponding equations that maintain spacetime covariance. The conditions connect the effective Hamiltonian, the Dirac observable for the black hole mass, and the free function. The solution of these equations produces two families of effective Hamiltonian constraints, each characterized by a distinct quantum parameter. In the limit where these parameters vanish, the classical constraints are recovered. Thus, the effective Hamiltonian constraints generate two distinct black hole configurations, each characterized by its own quantum correction parameter.

The spacetime metric describing one of the QCBHs is given by [18]

$$ds^2 = -f(r)dt^2 + f(r)^{-1}dr^2 + r^2(d\theta^2 + \sin^2\theta d\phi^2), \tag{1.2}$$

where

$$f(r) = \left(1 - \frac{2M}{r}\right)\left[1 + \frac{\xi^2}{r^2}\left(1 - \frac{2M}{r}\right)\right], \tag{1.3}$$

and M and ξ are the mass of the BH and the quantum correction parameter, respectively. For further analysis, we shall for simplicity normalize the quantum correction parameter $\xi \to \xi/M$. The quantum correction parameter ξ encodes quantum-gravity effects in spacetime, and its normalized form can be written as $\xi = \gamma\sqrt{A}/M$, where γ and A are the Barbero–Immirzi parameter of loop quantum gravity (LQG) and the minimal area gap A associated with holonomy quantization. The area gap, given by $A = 4\sqrt{3}\pi\gamma\ell_p^2$, corresponds to the smallest non-zero eigenvalue of the area operator in LQG, where ℓ_p denotes the Planck length [56]. The parameter ξ indicates the scale at which quantum-gravity effects become more apparent. In the limit $\xi \to 0$, the quantum corrections vanish and the Schwarzschild solution is recovered. Because the Barbero–Immirzi parameter γ is not fixed from fundamental principles in LQG [57, 58], ξ is regarded as a free parameter in our analysis. This allows us to explore possible quantum modifications to black-hole spacetimes arising from LQG.

The Hamiltonian of a neutral particle moving around the QCBH is expressed as follows [59]

$$H = \frac{1}{2}g^{\alpha\beta}p_\alpha p_\beta\ , \tag{1.4}$$

where p^α is the four-momentum of the neutral particle. In the spherical coordinate system, α and β denote the indices of the (t, r, θ, ϕ) coordinates. The relationship between four-momentum and four-velocity is expressed by the equation $p^\alpha = mu^\alpha$, where m represents the mass of the neutral particle, $u^\alpha = dx^\alpha/d\tau$ is the four-velocity. Furthermore, τ defines the proper time. Since the spacetime metric (1.2) does not explicitly depend on the t and ϕ coordinates, the following conserved quantities can be written [59]

$$\frac{p_t}{m} = g_{tt}\frac{dt}{d\tau} = -\mathcal{E}\ , \qquad \frac{p_\phi}{m} = g_{\phi\phi}\frac{d\phi}{d\tau} = \mathcal{L}\ , \tag{1.5}$$

where $\mathcal{E}$ and $\mathcal{L}$ are the specific energy and the specific angular momentum of the particle. Knowing that the Hamiltonian for a massive particle is $H = -m^2/2$ and for a photon is $H = 0$, we can write the following equation using Eq. (1.5)

$$\frac{1}{2}\left(g^{rr}p_r^2 + g^{\theta\theta}p_\theta^2\right) + \frac{m^2}{2}\left(g^{tt}\mathcal{E}^2 + g^{\phi\phi}\mathcal{L}^2\right) = -\frac{m^2}{2}. \tag{1.6}$$

After defining $\mathcal{H}$ as:

$$\mathcal{H} = \frac{1}{2}\left(g^{tt}\mathcal{E}^2 + g^{\phi\phi}\mathcal{L}^2 + 1\right), \tag{1.7}$$

and using

$$p_r = g_{rr}p^r = g_{rr}m\frac{dr}{d\tau},$$
$$p_\theta = g_{\theta\theta}p^\theta = g_{\theta\theta}m\frac{d\theta}{d\tau},$$

we rewrite Eq. (1.6) as:

$$g_{rr}\left(\frac{dr}{d\tau}\right)^2 + g_{\theta\theta}\left(\frac{d\theta}{d\tau}\right)^2 = -2\mathcal{H}\ . \tag{1.8}$$

We consider the motion of a particle confined to the equatorial plane, where $\theta = \pi/2 = const$. Under this assumption, the second term in Eq. (1.8) vanishes, and the equation simplifies to the following form:

$$g_{rr}\left(\frac{dr}{d\tau}\right)^2 = -2\mathcal{H}\ . \tag{1.9}$$

Using the conservation of angular momentum Eq. (1.5) and Eq. (1.9), we can derive the following equation of motion:

$$\left(\frac{dr}{d\phi}\right)^2 = -\frac{2g_{\phi\phi}^2\mathcal{H}}{g_{rr}\mathcal{L}^2}\,. \tag{1.10}$$

Substituting Eq. (1.7) into Eq. (1.10) yields the following equation:

$$\left(\frac{dr}{d\phi}\right)^2 = \frac{r^4}{\mathcal{L}^2}\left(\mathcal{E}^2 - f(r)\left(1+\frac{\mathcal{L}^2}{r^2}\right)\right) . \tag{1.11}$$

In the case of the particle moving in a circular orbit $r = const$, the first term of the same equation becomes zero, and the equation takes the following form

$$g_{\theta\theta}\left(\frac{d\theta}{d\tau}\right)^2 = -2\mathcal{H} . \tag{1.12}$$

The following conditions hold for the circular motion of a particle with the radius $r = r_c$ in the plane $\theta = \theta_c$:

$$\mathcal{H}(r_c) = 0\,, \qquad \partial_r\mathcal{H}|_{r_c} = 0\,, \tag{1.13}$$

and

$$\mathcal{H}(\theta_c) = 0\,, \qquad \partial_\theta\mathcal{H}|_{\theta_c} = 0\,. \tag{1.14}$$

If we solve Eq. (1.7) using Eq. (1.5) along with conditions (1.13) and (1.14), we obtain the following expressions for the specific energy $\mathcal{E}$ and specific angular momentum $\mathcal{L}$

$$\mathcal{E} = -\frac{g_{tt}}{\sqrt{-g_{tt} - g_{\phi\phi}\Omega^2}}, \tag{1.15}$$

$$\mathcal{L} = \frac{g_{\phi\phi}\Omega}{\sqrt{-g_{tt} - g_{\phi\phi}\Omega^2}} , \tag{1.16}$$

where $\Omega = d\phi/dt$ represents the angular velocity of the particle measured by distant observers. It can be calculated using the following expression [60, 61]:

$$\Omega = \frac{d\phi}{dt} = \pm\sqrt{-\frac{g_{tt,r}}{g_{\phi\phi,r}}}\,. \tag{1.17}$$

We can easily define Ω from the metric (1.2) using the above expression as

$$\Omega = \pm\sqrt{\frac{Mr^3 - \xi^2\left(8M^2 - 6Mr + r^2\right)}{r^6}\csc^2(\theta)}\ . \tag{1.18}$$

Thus, the following expressions for $\mathcal{E}$ and $\mathcal{L}$ can be written

$$\mathcal{E} = \frac{(2M-r)\left(2M\xi^2 - r\left(\xi^2+r^2\right)\right)}{r^2\sqrt{(r-3M)\left(2\xi^2(r-2M)+r^3\right)}}, \tag{1.19}$$

$$\mathcal{L} = \sqrt{\frac{r^2\left(Mr^3 - \xi^2\left(8M^2-6Mr+r^2\right)\right)}{(r-3M)\left(2\xi^2(r-2M)+r^3\right)}\sin^2(\theta)}\,. \tag{1.20}$$

After making the following transformation

$$u = \frac{1}{r}, \quad \frac{du}{d\phi} = -\frac{1}{r^2}\frac{dr}{d\phi}\,, \tag{1.21}$$

Eq. (1.11) becomes:

$$\left(\frac{du}{d\phi}\right)^2 = \frac{\mathcal{E}^2}{\mathcal{L}^2} - \frac{f(u)}{\mathcal{L}^2}\left(1+\mathcal{L}^2u^2\right)\,, \tag{1.22}$$

where

$$f(u) = (1-2Mu)(1+\xi^2u^2(1-2Mu))\,. \tag{1.23}$$

By differentiating Eq. (1.22) with respect to ϕ, we obtain the geodesic equation for a massive test particle moving around the QCBH

$$\begin{aligned}\frac{d^2u}{d\phi^2} &= \frac{M}{\mathcal{L}^2} - u + 3Mu^2 \\ &-\xi^2u(1-2Mu)\left(\frac{1-4Mu}{\mathcal{L}^2}+2u^2-6Mu^3\right).\end{aligned} \tag{1.24}$$

1.2.2 The perihelion shift

To determine the perihelion shift of the test particle's orbit, we rewrite Eq. (1.24)

$$\frac{d^2u}{d\phi^2} = \frac{M}{\mathcal{L}^2} - u + \frac{g(u)}{\mathcal{L}^2}\,, \tag{1.25}$$

where

$$\frac{g(u)}{\mathcal{L}^2} = 3Mu^2 - \xi^2u(1-2Mu)\left(\frac{1-4Mu}{\mathcal{L}^2}+2u^2-6Mu^3\right)\,.$$

Following the method presented in [62], we define the perihelion shift after a full revolution as:

$$\Delta\varphi = \frac{\pi}{\mathcal{L}^2}\left|\frac{dg(u)}{du}\right|_{u=\frac{1}{b}} , \tag{1.26}$$

where b is defined as $b = a(1-e^2)$. Here, a and e denote the semi-major axis and eccentricity of the orbit, respectively. Additionally, we define M as $M \Rightarrow GM/c^2$, and L^2 as $L^2 \Rightarrow GMa(1-e^2)/c^2$ in SI units. After this transformation, the expression takes the following form:

$$\begin{aligned} \Delta\phi &= \frac{6\pi GM}{ac^2(1-e^2)} - \frac{\pi GM\xi^2}{ac^2(1-e^2)}\Bigg(1 - \frac{6GM}{ac^2(1-e^2)} - \\ &- \frac{16G^2M^2}{a^2c^4(1-e^2)^2} + \frac{60G^3M^3}{a^3c^6(1-e^2)^3}\Bigg) . \end{aligned} \tag{1.27}$$

For a numerical application, we consider the example of Mercury and use the following parameters

$$\begin{aligned} \frac{2GM_\odot}{c^2} &= 2.95325008 \times 10^3\,[\mathrm{m}] , \\ a &= 5.7909175 \times 10^{10}\,[\mathrm{m}] , \\ e &= 0.20563069 . \end{aligned}$$

With these parameters, we derive the following numerical result for Mercury's perihelion shift

$$\Delta\phi = 2\pi \times (7.98744 \times 10^{-8}) - 2\pi \times (1.33124 \times 10^{-8})\xi^2 . \tag{1.28}$$

The first and second terms correspond to the prediction of and the influence of the quantum correction parameter, respectively. The measured perihelion shift of Mercury is expressed as [63–66]

$$2\pi\times(7.98734-0.00037)\times10^{-8}\frac{\mathrm{rad}}{\mathrm{rev}} \leq \Delta\phi_{\mathrm{obs}} \leq 2\pi\times(7.98734+0.00037)\times10^{-8}\frac{\mathrm{rad}}{\mathrm{rev}} . \tag{1.29}$$

Using Eq. (1.28) and Eq. (1.29), we can estimate the possible value of the quantum correction parameter ξ for Mercury

$$\xi \leq 0.01869 \,. \tag{1.30}$$

The influence of metric-affine geometry on particle motion becomes significant in strong gravitational regimes. One such scenario occurs in high-density astrophysical environments, such as near a supermassive BH. High-precision astrometric observations near the compact source Sgr A* and the S2 star, which orbits this supermassive BH and has an estimated mass between 10 and $15 M_\odot$, allow us to estimate the quantum correction parameter ξ [67]. The S2 star can be treated as a test body moving along a geodesic trajectory. For this estimation, we adopt the following parameters

$$\begin{aligned}
G &= 6.6743 \times 10^{-11}\,[\mathrm{m}^3/(\mathrm{kg}\cdot\mathrm{s}^2)]\,,\\
c &= 299,792,458\,[\mathrm{m/s}]\,,\\
M_\odot &= 1.988416 \times 10^{30}\,[\mathrm{kg}]\,,\\
M_{\mathrm{Sgr\ A}^*} &= 4.260 \times 10^{6} M_\odot\,,\\
a_{\mathrm{S2}} &= 970\,[\mathrm{au}]\,,\\
1\ \mathrm{au} &= 1.495978707 \times 10^{11}\,[\mathrm{m}]\,,\\
e_{\mathrm{S2}} &= 0.884649\,,\\
T_{\mathrm{S2}} &= 16.052\,[\mathrm{years}]\,.
\end{aligned}$$

Using these parameters, we obtain the following numerical result for the perihelion shift of the S2 star

$$\Delta\phi = 48.298 - 8.040\,\xi^2 \Big[\,''/\mathrm{year}\Big]\,. \tag{1.31}$$

The observed perihelion shift of the S2 star orbiting Sgr A* is given by

$$48.298\, f_- \,\Big[\,''/\mathrm{year}\Big] \leq \Delta\phi_{\mathrm{obs}} \leq 48.298\, f_+ \,\Big[\,''/\mathrm{year}\Big]\,, \tag{1.32}$$

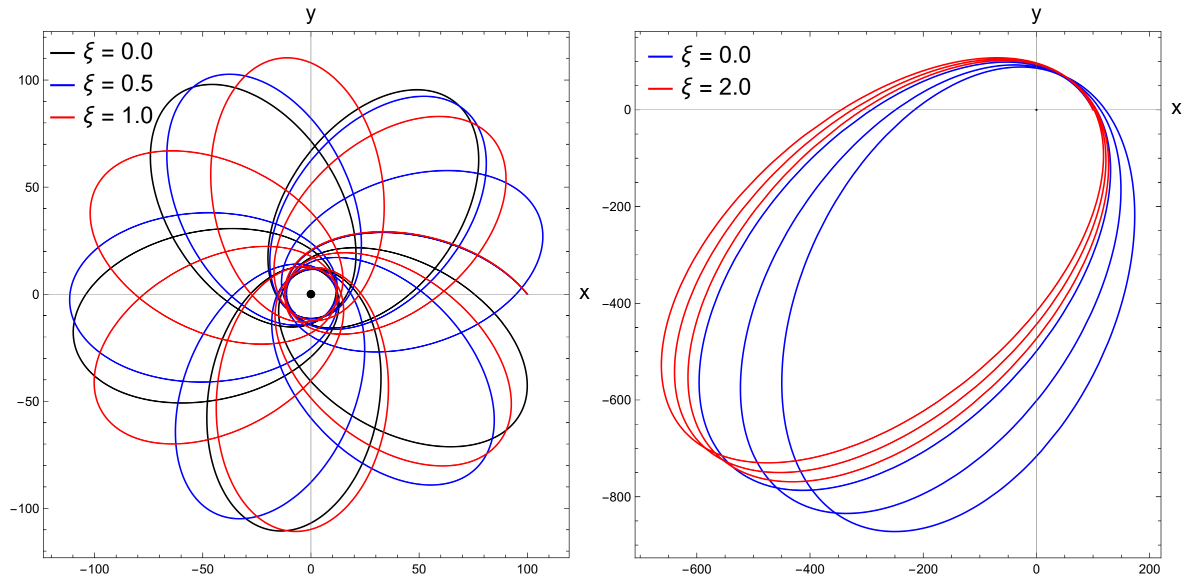

Figure 1.1: The trajectories of a test particle moving in the equatorial plane ($z = 0$) of a QCBH spacetime are shown for different values of the quantum correction parameter ξ. Left panel: The orbital motion of a particle with specific energy $\mathcal{E} = 0.992$, specific angular momentum $\mathcal{L} = 5$, and initial inverse radial coordinate $u = 1/r = 0.01$ around a BH of mass $M = 1$. Right panel: The effect of ξ on the perihelion shift of a particle with $\mathcal{E} = 0.999$, $\mathcal{L} = 12.5$, and $u = 1/r = 0.01$. As ξ increases, the perihelion shift decreases, highlighting the impact of quantum corrections on the orbital dynamics.

where $f_{\pm} = 1.10 \pm 0.19$ [67]. By utilizing Eqs. (1.31) and (1.32), we can determine the possible value of the quantum correction parameter ξ for the S2 star

$$\xi \leq 0.73528\,. \tag{1.33}$$

Fig. 1.1 illustrates the effect of the quantum correction parameter ξ on the trajectory of a particle orbiting a QCBH. The left panel of Fig. 1.1 illustrates the trajectory of a particle for different values of ξ, while keeping the initial conditions energy, angular momentum, and initial position constant. The black trajectory represents the classical motion of a particle orbiting a Schwarzschild BH ($\xi = 0.0$). As ξ increases, the trajectories deviate significantly from the classical case, demonstrating the impact of quantum corrections on the particle's motion. The right panel of Fig. 1.1 depicts the effect of the quantum correction parameter on the perihelion shift of the particle. The graph shows that as ξ increases, the perihelion shift decreases. This trend is in agreement with the analytical result given by Eq. (1.27), confirming that quantum corrections reduce the relativistic precession of the orbit.

1.2.3 The dynamics of epicyclic motion

Suppose that a particle is moving in a circular orbit of radius $r = r_c$ in the equatorial plane $\theta = \pi/2$. If the particle deviates from its stable circular orbit by small perturbations δr and $\delta\theta$, it begins to oscillate around the circular orbit at r_c. These oscillations, characterized by radial and latitudinal frequencies, are collectively referred to as epicyclic frequency. We can write the following expressions for r and θ for this perturbations:

$$r = r_c + \delta r \quad \text{and} \quad \theta = \pi/2 + \delta\theta\,. \tag{1.34}$$

The change in $\mathcal{H}$ due to this perturbation can be determined by expanding $\mathcal{H}$ in a Taylor series about $r = r_c$ and $\theta = \pi/2$

$$\begin{aligned}\mathcal{H}(r,\theta) &= \mathcal{H}(r_c,\frac{\pi}{2}) + \delta r\partial_r\mathcal{H}(r,\theta)\Big|_{r_c,\frac{\pi}{2}} + \delta\theta\partial_\theta\mathcal{H}(r,\theta)\Big|_{r_c,\frac{\pi}{2}} + \\ &+ \delta r\delta\theta\partial_r\partial_\theta\mathcal{H}(r,\theta)\Big|_{r_c,\frac{\pi}{2}} + \frac{1}{2}\delta r^2\partial_r^2\mathcal{H}(r,\theta)\Big|_{r_c,\frac{\pi}{2}} + \frac{1}{2}\delta\theta^2\partial_\theta^2\mathcal{H}(r,\theta)\Big|_{r_c,\frac{\pi}{2}} + \\ &+ \mathcal{O}\left(\delta r^3,\delta\theta^3\right)\ .\end{aligned} \tag{1.35}$$

According to conditions (1.13) and (1.14) for circular motion, the first four terms in the above expression vanish. Additionally, since they are very small, terms of $\mathcal{O}(\delta r^3,\delta\theta^3)$ and higher can be neglected. As a result, the expression simplifies to the following form:

$$\mathcal{H}(r,\theta) = \frac{1}{2}\delta r^2\partial_r^2\mathcal{H}(r,\theta)\Big|_{r_c,\frac{\pi}{2}} + \frac{1}{2}\delta\theta^2\partial_\theta^2\mathcal{H}(r,\theta)\Big|_{r_c,\frac{\pi}{2}}\ . \tag{1.36}$$

Substituting expressions (1.34) and (1.36) into Eq. (1.8), we obtain the following equation:

$$g_{rr}\delta\dot{r}^2 + g_{\theta\theta}\delta\dot{\theta}^2 = -\delta r^2\partial_r^2\mathcal{H}(r,\theta)\Big|_{r_c,\frac{\pi}{2}} - \delta\theta^2\partial_\theta^2\mathcal{H}(r,\theta)\Big|_{r_c,\frac{\pi}{2}} . \tag{1.37}$$

Here, since d and δ commute, we have made the substitutions $d\delta r/d\tau = \delta\dot{r}$ and $d\delta\theta/d\tau = \delta\dot{\theta}$. Taking the first derivative of both sides of the above equation with respect to proper time τ, we obtain

$$\delta\dot{r}\left[g_{rr}\delta\ddot{r} + \partial_r^2\mathcal{H}(r,\theta)\Big|_{r_c,\frac{\pi}{2}}\delta r\right] + \delta\dot{\theta}\left[g_{rr}\delta\ddot{\theta} + \partial_\theta^2\mathcal{H}(r,\theta)\Big|_{r_c,\frac{\pi}{2}}\delta\theta\right] = 0 . \tag{1.38}$$

The solutions $\delta\dot{r} = 0$ and $\delta\dot{\theta} = 0$ are not satisfactory, as they indicate the absence of oscillations. In this case, the equation has a solution only if the expressions within the brackets are zero [68, 69]

$$\delta\ddot{r} + \Omega_r^2\delta r = 0 \quad \text{and} \quad \delta\ddot{\theta} + \Omega_\theta^2\delta\theta = 0\,, \tag{1.39}$$

where

$$\Omega_r^2 = \frac{\partial_r^2\mathcal{H}(r,\theta)|_{r_c,\frac{\pi}{2}}}{g_{rr}} , \tag{1.40}$$

$$\Omega_\theta^2 = \frac{\partial_\theta^2\mathcal{H}(r,\theta)|_{r_c,\frac{\pi}{2}}}{g_{\theta\theta}} . \tag{1.41}$$

By substituting Eq. (1.19), (1.20) and (1.7) into Eq. (1.40) and (1.41), we obtain the following expressions for Ω_r and Ω_θ

$$\Omega_r^2 = \frac{3M\xi^2 r^3\left(12M^2 - 8Mr + r^2\right) + Mr^6(r-6M)}{r^6(r-3M)\left(2\xi^2(r-2M) + r^3\right)} - \\ - \frac{2\xi^4(r-2M)^2\left(24M^2 - 13Mr + 2r^2\right)}{r^6(r-3M)\left(2\xi^2(r-2M) + r^3\right)} , \tag{1.42}$$

$$\Omega_\theta^2 = \frac{Mr^3 - \xi^2\left(8M^2 - 6Mr + r^2\right)}{r^2(r-3M)\left(2\xi^2(r-2M) + r^3\right)} . \tag{1.43}$$

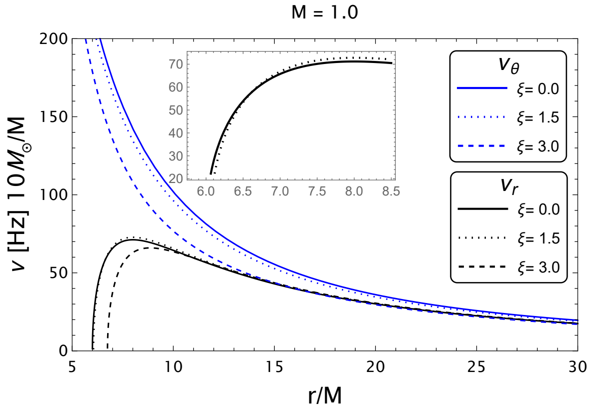

Figure 1.2: The radial profile of the frequencies ν_θ and ν_r measured by a distant observer is shown as a function of r/M for different values of the quantum correction parameter ξ.

Usually, it is not the local value of the epicyclic frequency that is important but the value measured by a distant observer, as many astronomical objects are located far away. The following equation gives the relationship between local and distant epicyclic frequencies:

$$\omega_{distant} = \frac{\Omega_{local}}{u^t} \ , \tag{1.44}$$

where $u^t = dt/d\tau$, which can be determined by substituting Eq. (1.15) into Eq. (1.5)

$$u^t = \frac{1}{\sqrt{-g_{tt} - g_{\phi\phi}\Omega^2}} \ . \tag{1.45}$$

Thus, the expression for the epicyclic frequencies measured by a distant observer is given as follows

$$\begin{aligned} \omega_r^2 = {} & \frac{3M\xi^2 r^3\left(12M^2 - 8Mr + r^2\right) + Mr^6(r - 6M)}{r^{10}} - \\ & - \frac{2\xi^4(r - 2M)^2\left(24M^2 - 13Mr + 2r^2\right)}{r^{10}} \ , \end{aligned} \tag{1.46}$$

$$\omega_\theta^2 = \frac{Mr^3 - \xi^2\left(8M^2 - 6Mr + r^2\right)}{r^6} \ . \tag{1.47}$$

To express the frequency in SI units (Hz), the following transformation is required

$$\nu_i = \frac{\omega_i}{2\pi}\frac{c^3}{GM} \ . \tag{1.48}$$

	GRS 1915 + 105 [72]	H1743-322 [73,74]	XTE J1550 - 564 [75,76]	GRO J1655 - 40 [77]
$M[M_\odot]$	$12.4^{+2.0}_{-1.8}$	$11.21^{+1.65}_{-1.96}$	$9.1^{+0.61}_{-0.61}$	$5.4^{+0.3}_{-0.3}$
$\nu_U[Hz]$	$168^{+3.0}_{-3.0}$	$240^{+3.0}_{-3.0}$	$276^{+3.0}_{-3.0}$	$441^{+2.0}_{-2.0}$
$\nu_L[Hz]$	$113^{+5.0}_{-5.0}$	$165^{+9.0}_{-5.0}$	$184^{+5.0}_{-5.0}$	$298^{+4.0}_{-4.0}$

Table 1.1: The mass, upper, and lower frequencies of the QPOs from the X-ray binaries selected for analysis.

Fig. 1.2 presents the epicyclic frequencies ν_r and ν_θ as a function of r/M, as measured by a distant observer, for different values of the quantum correction parameter ξ. Both ν_r and ν_θ decrease as r/M increases. Higher values of the quantum correction parameter ξ result in lower oscillation frequencies, shifting ν_θ to the left and ν_r to the right.

1.2.4 Constrains on the parameters of the quantum corrected black hole through the astrophysical quasiperiodic oscillations's data

In this section, we analyze four distinct QPO sources from various X-ray binaries, using validated observational data, as presented in Table 1.1 to constrain the effects of the quantum correction parameter ξ in QCBH. We adopt the forced resonance model as the theoretical framework to constrain the quantum correction parameter ξ of QCBH [66, 70, 71]. Within this model, the upper (ν_U) and lower (ν_L) frequencies are defined as follows.

$$\nu_U = \nu_\theta + \nu_r \, , \, \nu_L = \nu_\theta \; . \tag{1.49}$$

In Fig. 1.2.4, we plot the upper and lower frequencies of a particle near $r_{\rm isco}$ as a function of the BH mass M for various values of ξ. The left panel of the figure illustrates the effect of ξ on the upper frequencies. Clearly, the upper frequency $f_{\rm UP}$ decreases as both ξ and M increase. As the mass M increases, the gravitational force that pulls the particle toward the BH also becomes stronger. Consequently, the innermost stable circular orbit expands, causing the QPO to occur farther from the BH. As a result, the QPO frequency decreases, as indicated by Eqs. (1.42) and (1.43). In the right panel of Fig. 1.2.4, the upper and lower frequencies of a particle near the innermost stable circular orbit $r_{\rm isco}$ are plotted as functions of $M/M_\odot$ using the best-fit values of the quantum correction parameter ξ. The best-fit values of ξ for these QPO sources are $\xi = 2.74 \pm 0.01$ for the upper frequency and $\xi = 2.68 \pm 0.03$ for the lower frequency. It is worth, however, noting that the errors in the best-fit values of ξ result from the observational uncertainties incorporated into the fitting procedure (as seen in Table 1.1). It should be emphasized that these best-fit values do not imply a discovery of a non-zero ξ, since their determination is based on the simplifying assumption that QPOs are generated at the innermost stable circular orbit ($r_{\rm ISCO}$). In realistic scenarios, this assumption may not always hold. Nevertheless, the obtained best-fit values suggest the possible existence of a unique ξ that remains consistent across those mentioned black hole candidates.

To estimate the limiting value of ξ for each QPO source, we used the *emcee* Python package [78], which employs the Markov Chain Monte Carlo (MCMC) method to constrain the physical parameters. The posterior probability distribution, based on Bayes' theorem, is expressed as:

$$P(\Theta|D,\mathcal{M}) = \frac{L(D|\Theta,\mathcal{M})\mathcal{P}(\Theta|\mathcal{M})}{P(D|\mathcal{M})}\,, \tag{1.50}$$

where $P(\Theta|D,\mathcal{M})$ represents the *posterior probability*, $L(D|\Theta,\mathcal{M})$ is the *likelihood function*, $\mathcal{P}(\Theta|\mathcal{M})$ is the *prior probability*, and $P(D|\mathcal{M})$ serves as a *normalizing constant*. To specify the priors, we assume a Gaussian prior distribution for the model parameters within specified boundaries:

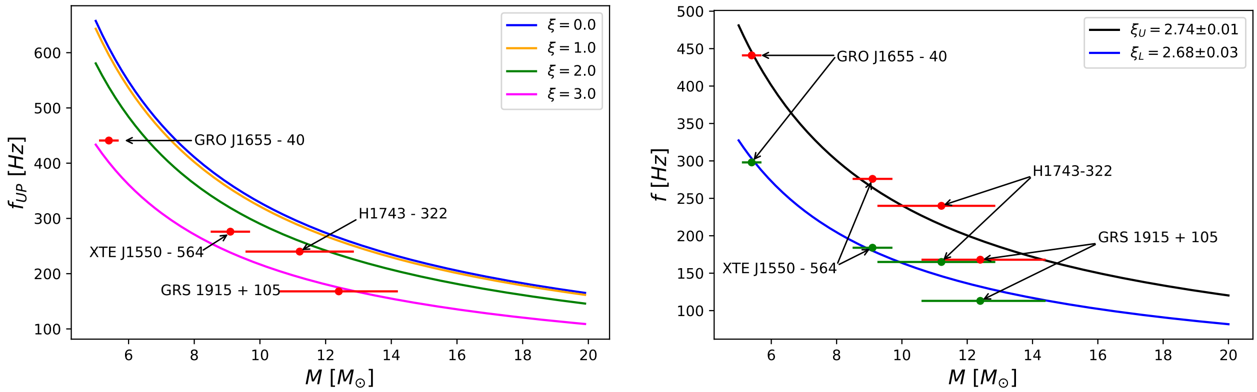

Figure 1.3: Left: The upper ν_U frequency is depicted as functions of the mass M for different values of ξ, analyzed near the ISCO radius $r_{\rm isco}$. Red horizontal lines indicate the observational data for various QPO sources, with the width of these lines representing the uncertainty in the mass of the sources. Right: The upper and lower frequencies of a particle near the ISCO radius $r_{\rm isco}$ are plotted as function of $M/M_\odot$ for the best-fit values of ξ. The black solid curve represents the best-fit curve of the upper frequency f_U, while the blue solid curve corresponds to the lower frequency f_L. Red lines indicate the upper frequency and green lines represent the lower frequency. The width of these horizontal lines reflects the uncertainty in the mass estimates of the sources.

$$\mathcal{P}(\theta_i) \sim \exp\left[\frac{1}{2}\left(\frac{\theta_i - \theta_{0,i}}{\sigma_i}\right)^2\right], \quad \theta_{low,i} < \theta_i < \theta_{high,i}\,, \tag{1.51}$$

where $\theta_i = [M, r, \xi]$ and σ_i are their corresponding standard deviations. The prior values for these parameters are adopted as presented in Table 1.2.

For the quantum correction parameter ξ, we assume a uniform prior distribution over a specified range:

$$\mathcal{P}(\xi) = 1, \quad \text{for } \xi \in [0, 5]\,, \tag{1.52}$$

otherwise, we set $\mathcal{P}(\xi) = 0$. This choice ensures that the parameter space remains constrained within a physically meaningful range.

Based on the upper and lower frequency expressions in Eqs. (1.49), our MCMC analysis incorporates data from both the upper and lower frequencies (see Ta-

Parameters	GRS 1915 + 105		H1743-322		XTE J1550 - 564		GRO J1655 - 40	
	μ	σ	μ	σ	μ	σ	μ	σ
$M/M_{\odot}$	12.4	0.6	11.21	0.6	9.1	0.6	5.4	0.3
r/M	7.4	0.3	7.26	0.3	7.2	0.3	7.3	0.3
ξ/M	Uniform [0, 5)		Uniform [0, 5)		Uniform [0, 5)		Uniform [0, 5)	

Table 1.2: Gaussian priors for the selected X-ray binaries used in the MCMC analysis of QPOs occurring around QCBH.

ble 1.1). Consequently, the likelihood function L is expressed as:

$$\log L = \log L_U + \log L_L \,, \tag{1.53}$$

where $\log L_U$ denotes the likelihood of the upper frequencies,

$$\log L_U = -\frac{1}{2}\sum_i \frac{(\nu^i_{U,obs} - \nu^i_{U,model})^2}{(\sigma^i_{U,obs})^2} \,, \tag{1.54}$$

and $\log L_L$ represents the likelihood of the lower frequencies,

$$\log L_L = -\frac{1}{2}\sum_i \frac{(\nu^i_{L,obs} - \nu^i_{L,model})^2}{(\sigma^i_{L,obs})^2} \,. \tag{1.55}$$

Here, $\nu^i_{U,obs}$ and $\nu^i_{L,obs}$ represent the measured values of the upper and lower frequencies, while $\nu^i_{U,model}$ and $\nu^i_{L,model}$ correspond to their predicted values from the theoretical model. The terms $\sigma^i_{U,obs}$ and $\sigma^i_{L,obs}$ represent the statistical uncertainties associated with the measured upper and lower frequencies, respectively. Following the above setup, we perform an MCMC analysis to investigate the three-dimensional parameter space $\{r, M, \xi\}$ associated with the QCBH. The best-fit values for these parameters are summarized in Table 1.3, while Fig. 1.4 presents the MCMC posterior distributions for four selected astronomical objects. The

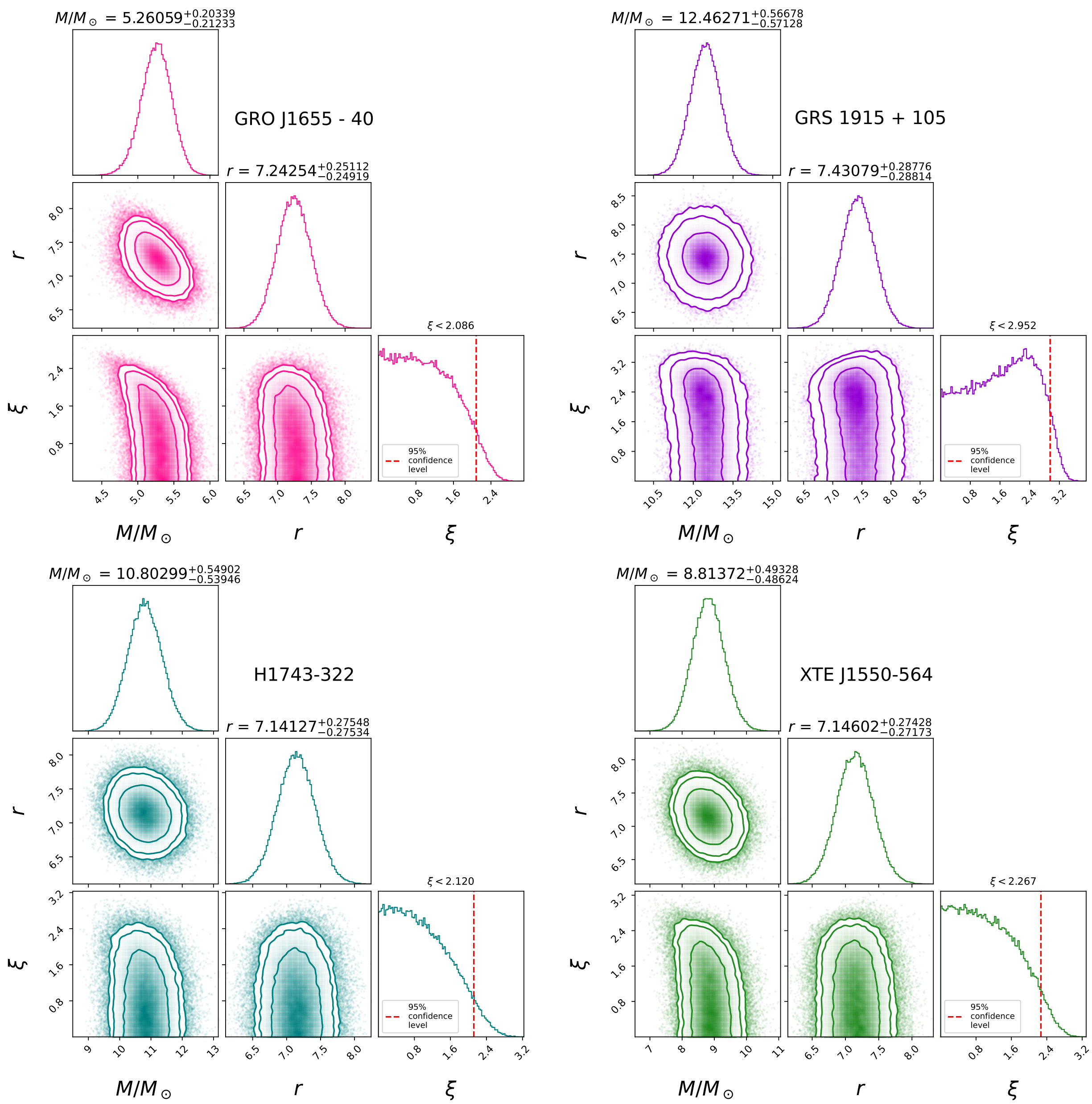

Figure 1.4: Constraints on the parameters of QCBH from QPO observations of GRO J1655-40, GRS 1915+105, H1743-322, and XTE J1550-564 using the MCMC method. The plots show the posterior distributions for the BH mass M, the dimensionless radius r/M, and the quantum correction parameter ξ within the forced resonance mode. The vertical dashed red lines indicate the 95% confidence level for ξ.

Parameters	GRS 1915 + 105	H1743-322	XTE J1550 - 564	GRO J1655 - 40
$M/M_\odot$	$12.45908^{+0.56642}_{-0.56419}$	$10.80299^{+0.54902}_{-0.53946}$	$8.81372^{+0.49328}_{-0.48624}$	$5.26059^{+0.20339}_{-0.21233}$
r/M	$7.43238^{+0.28877}_{-0.28595}$	$7.14127^{+0.27548}_{-0.27534}$	$7.14602^{+0.27428}_{-0.27173}$	$7.24254^{+0.25112}_{-0.24919}$
ξ/M	< 2.952	< 2.120	< 2.267	< 2.086

Table 1.3: The best-fit values of QCBH parameters derived from QPOs in X-ray binaries.

shaded regions in the Fig. 1.4 correspond to the 68%, 90%, and 95% confidence levels, offering insight into the statistical uncertainties of the inferred parameters.

The results indicate that the best-fit value of the quantum correction parameter ξ is obtained from GRO J1655-40, with an upper limit of $\xi \leq 2.086$ at the 95% confidence level. GRO J1655-40 was selected due to its higher measurement accuracy compared to other QPO sources (see Table 1.1). XTE J1550-564 and H1743-322 produced constraints close to that of GRO J1655-40, while GRS 1915+105 yielded a slightly higher upper limit. Therefore, we conclude that the quantum correction parameter is constrained to

$$\xi \leq 2.086 \; . \tag{1.56}$$

In this study, we obtained an upper limit of $\xi \leq 2.086$, which provides a tighter constraint compared to the limit $\xi \leq 2.304$ obtained from the M87 BH shadow [46] and the limit $\xi \leq 2.866$ derived from the Sgr A* shadow [45]. Unlike previous works that relied on BH shadow observations to constrain ξ, our approach utilizes QPO data from X-ray binaries, offering an alternative and complementary method for testing QCBHs in strong gravitational regimes.

1.3 Exploring rotating loop quantum black hole

1.3.1 The spacetime metric and electromagnetic field of rotating loop quantum black hole

Here, we examine the key properties of an intriguing model of rotating LQBHs [28, 29] immersed in a uniform external magnetic field (B), including the event horizon, static-limit-surface, and ergosphere. The LQBH spacetime arises through a polymer-like quantization procedure within LQG, which introduces a polymeric function P associated with the polymeric parameter δ (or δ_b). In this framework, the Schwarzschild interior is quantized by employing two parameters, δ_b and δ_c, which serve to replace the corresponding canonical variables:

$$b \to \frac{\sin(\delta_b b)}{\delta_b} \text{ and } c \to \frac{\sin(\delta_c c)}{\delta_c}\,. \tag{1.57}$$

It should be emphasized that δ_b and δ_c define the lengths of the paths along which holonomies are constructed, thereby setting the scales at which quantum effects become relevant. In the limit $(\delta_b, \delta_c) \to 0$, the classical Schwarzschild solution is recovered. Nevertheless, due to the absence of a complete theory of quantum gravity, no definitive prescription exists for fixing these parameters. As a result, multiple proposals have been suggested in the literature, each motivated by distinct physical or mathematical considerations. However, the self-dual spacetime considered in this work is constructed from a particular choice of fixing δ_b and δ_c as constants, corresponding to the μ_0-scheme in LQG [79, 80]. This choice yields the effective quantum-corrected interior of the Schwarzschild black hole. By identifying the minimum area in the solution with the fundamental minimum area $A_{\min}$ of the LQG, the two free parameters can be reduced. The remaining undetermined constant, δ_b, represents the dimensionless polymeric parameter, which must be constrained by experiments or observations.

By applying the Newman-Janis algorithm—specifically modified via Azreg-Aïnou's non-complexification method—a static solution is extended to include rotation. The metric for this LQBH is presented in Boyer-Lindquist coordinates as follows [30]:

$$\begin{aligned} ds^2 &= -\frac{\Delta}{\Sigma}\left(dt - a\sin^2\theta d\phi\right)^2 + \frac{\Sigma}{\Delta}dr^2 + \Sigma d\theta^2 \\ &+ \frac{\sin^2\theta}{\Sigma}\left(adt - \left(k^2 + a^2\right)d\phi\right)^2, \end{aligned} \tag{1.58}$$

with

$$\begin{aligned} \Delta &= \tfrac{(r-r_+)(r-r_-)(r^2)}{(r+r_*)^2} + a^2 \ , \\ \Sigma &= k^2(r) + a^2\cos^2\theta \ , \\ k^2 &= \tfrac{r^4+a_0^2}{(r+r_*)^2} \ , \end{aligned} \tag{1.59}$$

where a is the spin parameter of the BH. The two horizons of the non-rotating LQBH are given by $r_+ = 2M/(1+P)^2$ and $r_- = 2MP^2/(1+P)^2$. Additionally, $r_* = \sqrt{r_+ r_-} = 2MP/(1+P)^2$, where M denotes the ADM (Arnowitt-Deser-Misner) mass of the solution. P is the polymeric function and can be expressed as follows:

$$P = \frac{\sqrt{1+\epsilon^2}-1}{\sqrt{1+\epsilon^2}+1}, \tag{1.60}$$

where ϵ is the product of the Immirzi parameter γ and the polymeric parameter δ, and it must satisfy the condition $\epsilon = \gamma\delta \ll 1$. The Immirzi parameter measures the size of the quantum of area in Planck units. Its value is currently fixed by matching the semiclassical BH entropy, as calculated by Stephen Hawking, and the counting of microstates in LQG. The polymeric parameter δ characterizes the scale of quantum discreteness. Their small product $\gamma\delta \ll 1$ ensures that quantum corrections remain negligible at large scales but become significant near the BH core, thereby regularizing the geometry.

$$a_0 = \frac{A_{\min}}{8\pi}, \tag{1.61}$$

where $A_{\min}$ corresponds to the minimum area gap in LQG. In addition, $A_{\min}$ is connected to the Planck length l_{P} by the expression

$$A_{\min} \simeq 4\sqrt{3}\pi\gamma l_{\mathrm{P}}^2 \ . \tag{1.62}$$

The rotating LQBH metric describes a geodesically complete spacetime that remains regular at the core [30] and can represent a regular BH, an extremal BH, or even a horizonless compact object, depending on the values of the spin parameter a and the polymeric function P. the Kretschmann scalar in the limit $r \to 0$ and $\theta = \pi/2$,

$$K = R^{\mu}{}_{\nu\sigma\rho} R^{\nu\sigma\rho}{}_{\mu} \simeq \frac{64M^4P^4\left[a_0^2(1+P)^4 + 4a^2P^2M^2\right]}{a_0^8(1+P)^{16}} + \mathcal{O}(r). \tag{1.63}$$

It is clear that the rotating LQBH is regular, because of the presence of the minimal area $a_0 = A_{\min}/(8\pi)$ arising from LQG.

From Eq. (1.62), a_0 scales with the Planck length l_{P} and is anticipated to be extremely small. Thus, the influence of a_0 on spacetime should be negligible at observable scales. We will therefore set $a_0 = 0$ in this research.

Let's explore how the parameter ϵ affects the horizon and ergo-surface in the context of LQBH. Horizons and static-limit-surface are defined by the conditions $g^{rr} = 0$ and $g_{tt} = 0$, respectively. Based on these conditions, we can write the equations for the horizons and ergo-surfaces as follows,

$$r_{H\pm} = \frac{1}{4}(r_+ + r_-) + r_{H1} \pm r_{H2} \ , \tag{1.64}$$

$$r_{s\pm} = \frac{1}{4}(r_+ + r_-) + r_{s1} \pm r_{s2} \ . \tag{1.65}$$

Here, r_{H1}, r_{H2}, r_{s1}, and r_{s2} are expressed as:

$$
\begin{aligned}
r_{H1} &= \frac{1}{2}\left[\frac{1}{3}\left(a^2+r_+r_-\right)-a^2+\frac{1}{4}\left(r_++r_-\right)^2-r_+r_-+\frac{A}{3\sqrt[3]{2}}+B\right]^{\frac{1}{2}}, \qquad (1.66)\\
r_{H2} &= \frac{1}{2}\left[\frac{-4\left(r_++r_-\right)\left(a^2+r_+r_-\right)-16a^2r_*+\left(r_++r_-\right)^3}{8r_{H1}}\right.\\
&- \left.\frac{1}{3}\left(a^2+r_+r_-\right)-a^2+\frac{1}{2}\left(r_++r_-\right)^2-r_+r_--\frac{A}{3\sqrt[3]{2}}-B\right]^{\frac{1}{2}}, \qquad (1.67)
\end{aligned}
$$

where

$$
\begin{aligned}
A &= \sqrt[3]{C+D},\\
B &= \frac{\sqrt[3]{2}E}{3A},\\
C &= \sqrt{D^2-4E^3},\\
D &= 108a^4r_*^2-72a^2r_*^2\left(a^2+r_+r_-\right)+18a^2\left(r_++r_-\right)r_*\left(a^2+r_+r_-\right)\\
&\quad +2\left(a^2+r_+r_-\right)^3+27a^2\left(r_++r_-\right)^2r_*^2,\\
E &= 12a^2r_*^2+6a^2\left(r_++r_-\right)r_*+\left(a^2+r_+r_-\right)^2.
\end{aligned}
$$

The expressions for r_{s1} and r_{s2} are given by

$$
\begin{aligned}
r_{s1} &= \frac{1}{2}\left[-a^2\cos^2\theta+\frac{1}{3}\left(a^2\cos^2\theta+r_+r_-\right)+\frac{1}{4}\left(r_++r_-\right)^2-r_+r_-\right.\\
&+ \left.\frac{\mathcal{C}}{3\sqrt[3]{\mathcal{A}+\mathcal{B}}}+\frac{\sqrt[3]{\mathcal{A}+\mathcal{B}}}{3\sqrt[3]{2}}\right]^{\frac{1}{2}}, \qquad (1.68)\\
r_{s2} &= \frac{1}{2}\left[\frac{1}{8r_{s1}}\left(\left(r_++r_-\right)^3-4\left(r_++r_-\right)\left(a^2\cos^2\theta+r_-r_+\right)-16a^2r_*\cos^2\theta\right)\right.\\
&\quad -a^2\cos^2\theta-\frac{1}{3}\left(a^2\cos^2\theta+r_+r_-\right)-r_+r_-+\frac{1}{2}\left(r_++r_-\right)^2\\
&\quad \left.-\frac{\mathcal{C}}{3\sqrt[3]{\mathcal{A}+\mathcal{B}}}-\frac{\sqrt[3]{\mathcal{A}+\mathcal{B}}}{3\sqrt[3]{2}}\right]^{\frac{1}{2}}, \qquad (1.69)
\end{aligned}
$$

where

$$\mathcal{A} = \sqrt{\mathcal{B}^2 - 2\mathcal{C}^3},$$

$$\mathcal{B} = 108a^4 r_*^2 \cos^4\theta + 27a^2\left(r_+ + r_-\right)^2 r_*^2 \cos^2\theta - 72a^2 r_*^2 \cos^2\theta\left(a^2\cos^2\theta + r_+ r_-\right) \\ +2\left(a^2\cos^2\theta + r_+ r_-\right)^3 + 18a^2\left(r_+ + r_-\right) r_* \cos^2\theta\left(a^2\cos^2\theta + r_+ r_-\right),$$

$$\mathcal{C} = \sqrt[3]{2}\left[12a^2 r_*^2\cos^2\theta + 6a^2\left(r_+ + r_-\right) r_*\cos^2\theta + \left(a^2\cos^2\theta + r_+ r_-\right)^2\right].$$

It should be noted that when $\epsilon = 0$, Eq. (1.64) reduces to the horizon of the Kerr solution $r_{H\pm} = M \pm \sqrt{M^2 - a^2}$. Fig. 1.5 shows the effect of ϵ on the outer horizon (*top right*) and outer static-limit-surface (*left panel*). As ϵ increases, both the outer horizon and outer static-limit-surface shrink. However, it is important to note that for a fixed value of the spin parameter a, the overall ergosphere region (i.e. the space between the outer event horizon and outer static-limit-surface) increases as epsilon increases (see Fig. 1.5 left panel). The bottom right panel of Fig. 1.5 presents the permissible (shaded) values of parameters ϵ and a for which LQBH exits.

In astrophysics, studying the effect of magnetic fields on the properties of BHs is crucial. Previous studies have shown that the magnetic field strongly influences the properties of a BH's accretion disk [81, 82]. In this study, we assume the BH is surrounded by a weak magnetic field. Theoretical studies and observational data indicate that magnetic field strengths vary across different BHs; in some, the field is around 10^4 G , while in others, it can reach up to 10^8 G (see, e.g., in Refs. [83–85]). For example, the magnetic field strength in NGC1052 is in the range of $B \sim 200$ G $- 8\times10^4$ G, while in M87, it ranges from 1 G to 30 G (see, e.g., in Refs. [84, 86, 87]). Although the magnetic field is weak, it has a

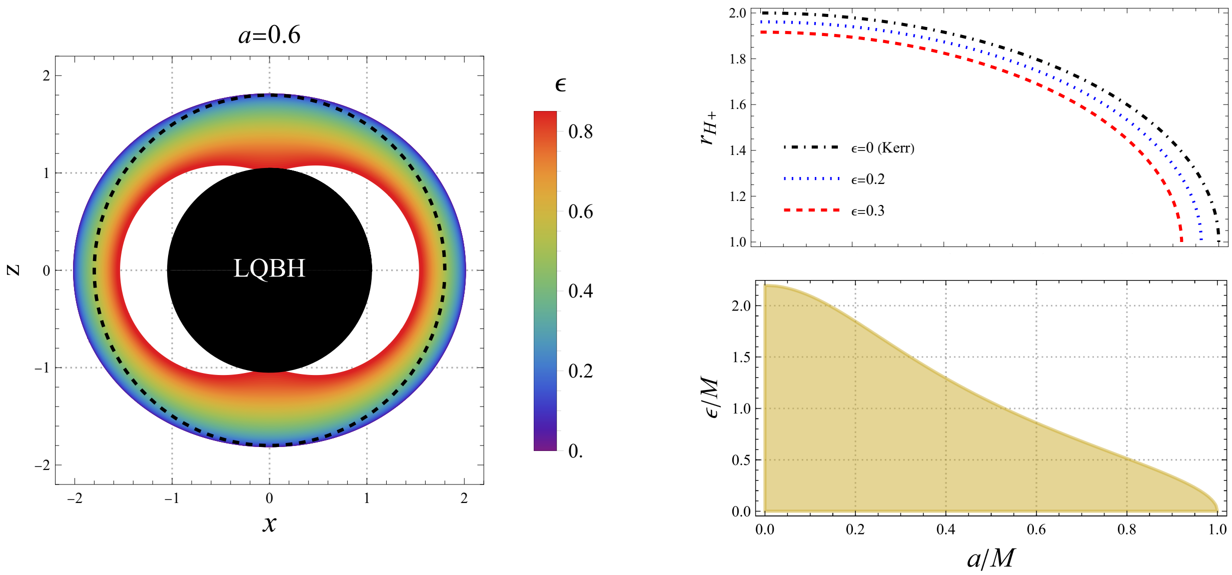

Figure 1.5: *Left panel:* Variation of the outer ergo-sphere r_{s+} with θ for different values of the parameter ϵ. The dotted line represents the event horizon r_{H+} for $\epsilon = 0$, while the inner black disk corresponds to the event horizon in the extremal case. *Right top panel:* Dependence of r_{H+} on the spin parameter a/M for various values of ϵ. *Right bottom panel:* Parameter space between the deformation parameter ϵ and the spin parameter a/M. The shaded region represents the theoretically allowed values of parameters ϵ and a for which LQBHs exist.

strong effect on the motion of charged particles around the BH. Therefore, the motion of particles in the magnetic field surrounding a BH has been extensively studied, and various models have been developed to address different scenarios (see, e.g., [60, 68, 88–95]).

For simplicity, we assume the magnetic field is uniform and aligned with the BH's symmetry axis [90, 96]. To determine the corresponding vector potential of the electromagnetic field, we apply the Wald method [97], which makes use of the Killing vectors of the spacetime. The Killing vector field ξ^{μ}, as the infinitesimal generator of an isometry, satisfies

$$\xi_{\alpha;\beta} + \xi_{\beta;\alpha} = 0 \tag{1.70}$$

They also satisfy the wave-like equations in vacuum spacetime, $\Box\xi^{\alpha} = 0$. This allows us to write the solution of the vacuum Maxwell equations, $\Box A^{\mu} = 0$, for the electromagnetic four-potential in the Lorentz gauge in the form:

$$A^\alpha = C_1 \xi^\alpha_{(t)} + C_2 \xi^\alpha_{(\varphi)} \,, \tag{1.71}$$

The constants related to the Killing vectors can be found easily — the constant $C_2 = B/2$, if we have the gravitational source immersed in the uniform magnetic field $\mathbf{B}$ that is parallel to the axis of rotation corresponding to the axial symmetry of the spacetime. The remaining constant C_1 can be easily calculated from the asymptotic properties of the spacetime at the infinity. Finally, the covariant components of the four-vector potential of the electromagnetic field can be written in the form

$$A_t = -\frac{aB}{2\Sigma}\Big(2\Delta + \big[k(r)^2 - a^2 - \Delta\big]\sin^2\theta\Big) \,, \tag{1.72}$$

$$A_\phi = -\frac{B\sin^2\theta}{2\Sigma}\Big(a^4 - k(r)^4 - 2a^2\Delta + a^2\sin^2\theta\Delta\Big) \,. \tag{1.73}$$

In the following section, we focus on analyzing the motion of charged particles near the LQBH, which is placed in a uniform external magnetic field.

1.3.2 Dynamics of Charged Particle in the Vicinity of LQBH

Here, we investigate a charged particle motion around the LQBH using the Hamiltonian, which is defined by (see, for example [59])

$$H = \frac{1}{2} g^{\alpha\beta}\left(P_\alpha - qA_\alpha\right)\left(P_\beta - qA_\beta\right) \,, \tag{1.74}$$

where P_α is the canonical momentum of a charged particle and A_α the four-vector potential of electromagnetic field. One can then connect the charged particle's four-momentum and its canonical momentum via the following equation

$$p^\alpha = g^{\alpha\beta}\left(P_\beta - qA_\beta\right) \,. \tag{1.75}$$

We can express the equation of motion for the charged particle using the Hamiltonian as follows:

$$\frac{dx^\alpha}{d\lambda} = \frac{\partial H}{\partial P_\alpha} \quad \text{and} \quad \frac{dP_\alpha}{d\lambda} = -\frac{\partial H}{\partial x^\alpha}\,, \tag{1.76}$$

where $(\lambda = \tau/m)$ denotes the affine parameter associated with (τ) describing the proper time of the particle. From the Eq. (1.76), the constants of motion can be written as shown below:

$$P_t - qA_t \;=\; g_{tt}p^t + g_{t\phi}p^\phi\,, \tag{1.77}$$

$$P_\phi - qA_\phi \;=\; g_{\phi t}p^t + g_{\phi\phi}p^\phi\,, \tag{1.78}$$

where P_t and P_ϕ correspond to the energy and angular momentum of a charged test particle, respectively, such that $P_t = -E$ and $P_\phi = L$. The equation governing the timelike radial motion of a charged particle in the equatorial plane $(\theta = \pi/2)$ can be expressed in the standard form (see, e.g., [1, 98])

$$\left(\frac{dr}{d\tau}\right)^2 + V_{\text{eff}}(r) = E^2, \tag{1.79}$$

where V_{eff} denotes the effective potential. Using the constants of motion (Eqs. 1.77, 1.78) together with the normalization condition $(g_{\alpha\beta}p^\alpha p^\beta = -m^2)$, the explicit expression for the effective potential in the present case takes the form

$$V_{\text{eff}} = -\frac{q}{m}A_t - \frac{g_{t\phi}}{g_{\phi\phi}}\left(\mathcal{L} - \frac{q}{m}A_\phi\right) + \left[(-g_{tt} - \omega g_{t\phi})\left(1 + \frac{\left(\mathcal{L} - \frac{q}{m}A_\phi\right)^2}{g_{\phi\phi}}\right)\right]^{1/2} \tag{1.80}$$

In our case, $V_{\rm eff}$ takes the following form

$$
\begin{aligned}
V_{\rm eff} &= \frac{a\,\beta\big(2r^2 - r(r_- + r_+) + r_- r_+\big)}{2r^2} \\
&+ \frac{a\big(r(r_- + r_+) - r_- r_+\big)(r + rs)^2}{r^6 + a^2\big(r^2 - r_- r_+ + r(r_- + r_+)\big)(r + r_\star)^2} \cdot K \\
&+ \sqrt{\frac{(r - r_-)(r - r_+)}{r^2} - \frac{a^2(r + r_\star)^2\big(r_- r_+ - r(r_- + r_+)\big)^2}{a^2 r^2 (r + r_\star)^2\big(r^2 + r(r_- + r_+) - r_- r_+\big) + r^8}} \\
&\times \sqrt{1 + K^2\Big(\frac{a^2\big(r^2 + r(r_- + r_+) - r_- r_+\big)}{r^2} + \frac{r^4}{(r + r_\star)^2}\Big)^{-1}}\,, \qquad (1.81)
\end{aligned}
$$

where K is

$$
K = \mathcal{L} - \beta \cdot \left(\frac{a^2(r - r_-)(r - r_+)}{2r^2} + \frac{r^4}{2(r + r_\star)^2}\right)\,,
$$

with $\mathcal{L} = L/m$ and $\beta = qBGM/(mc^4)$ being the angular momentum per unit mass of the particle and a dimensionless magnetic field parameter.

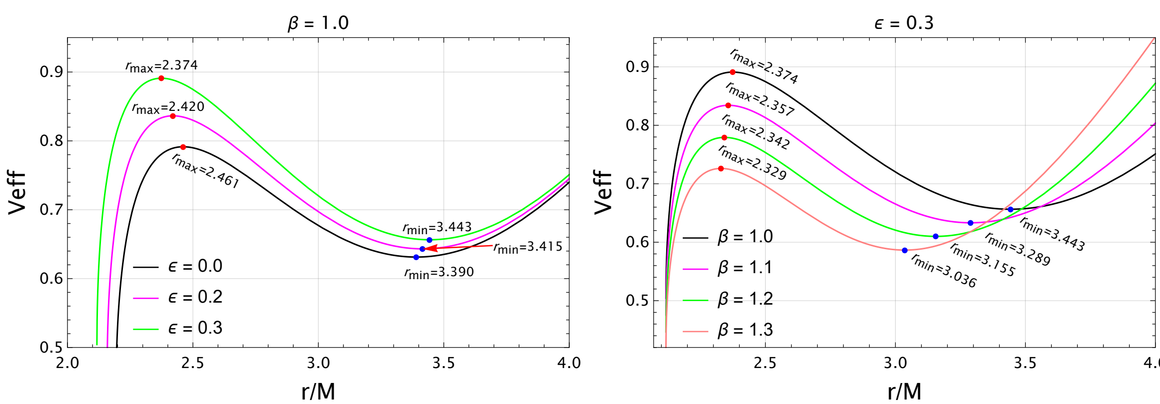

Figure 1.6: The effective potential $V_{\rm eff}$ is plotted as a function of r/M for different values of ϵ (left panel) and the magnetic field parameter β (right panel). In these plots, the spin parameter is set to $a = 0.8$.

The effective potential V_{eff} is a key tool for examining particle motion around a BH. The effective potential for a particle moving around the LQBH in the presence of an external magnetic field is shown in Fig. 1.6. The left and right panels of Fig. 1.6 depict the radial variation of the effective potential for different values of ϵ and the magnetic field parameter β, where one parameter is fixed while the other varies. In the figure, $r_{\rm min}$ and $r_{\rm max}$ correspond to the stable and unstable circular orbits of the particle, respectively. The left panel of the figure depicts how variations in ϵ affect the effective potential of the system when β is fixed. It is evident that as ϵ increases, the unstable orbit shifts to the left, i.e., to smaller values of r/M, while the stable orbit shifts to the right. In addition, increasing ϵ raises the height of the effective potential. This occurs because ϵ reduces the horizon radius r_H (see Fig. 1.5). As ϵ increases, the horizon r_H shrinks, enhancing the gravitational influence of the BH. This results in the formation of unstable orbits $r_{\rm max}$ closer to the BH's center, as well as unstable orbits $r_{\rm min}$ at greater distances. The right panel depicts the effect of the magnetic field on the effective potential. As β increases, both the stable orbit $r_{\rm min}$ and the unstable orbit $r_{\rm max}$ shift to the left, while the height of the effective potential decreases. This is a well-known effect of the magnetic field, indicating that a stronger magnetic field causes the particle to be more tightly confined towards the center of the BH.

Let us then analyze the motion of a charged particle on a stable circular orbit. In such motion, the radius vector r remains constant, and the following condition must be satisfied for circular motion:

$$V_{eff}(r) = \frac{\partial V_{eff}(r)}{\partial r} = 0. \tag{1.82}$$

For circular motion in the equatorial plane (r = const and θ = const), the four-velocity of the particle can be expressed as $\mathbf{u} \sim \xi_{(t)} + \Omega \xi_{(\phi)}$, where

$$\Omega = \frac{d\phi}{dt} = \frac{u^\phi}{u^t}\,, \tag{1.83}$$

represents the angular velocity of the particle as measured by a distant observer at infinity. The angular velocity Ω of a timelike particle is bounded by the angular velocities of the inner and outer photon circular orbits, satisfying $\Omega_- < \Omega < \Omega_+$

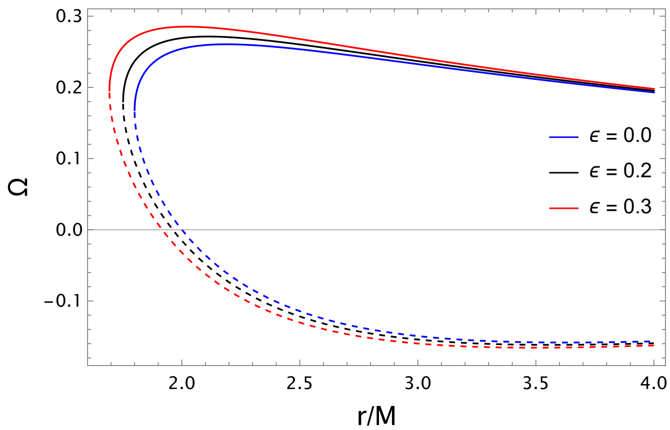

Figure 1.7: The angular velocity components Ω_+ (solid lines) and Ω_- (dashed lines) are plotted against r/M for different values of ϵ, with the spin parameter fixed at $a = 0.6$. For simplicity, we set $\theta = \pi/2$.

(see details, e.g., in Refs. [99, 100]), where

$$\Omega_\pm = \frac{-g_{t\phi} \pm \sqrt{(g_{t\phi})^2 - g_{tt}g_{\phi\phi}}}{g_{\phi\phi}} = \frac{\left(a(r_- + r_+)r - ar_\star^2 \pm r^2\sqrt{\Delta}\right)}{a^2\left(r^2 - r_\star^2 + r(r_- + r_+)\right) + \frac{r^6}{(r+r_\star)^2}}. \quad (1.84)$$

$$\begin{aligned} \Omega \;=\; & \frac{r^3\sqrt{p_t^2\left[\,(p_t^2-1)\,r^2 + r(r_- + r_+) - r_\star^2\right]\Delta}}{a^2\left[p_t^2 r^2\left[r^2 + r(r_- + r_+) - r_\star^2\right] + \left[r_\star^2 - r(r_- + r_+)\right]^2\right] + \frac{p_t^2 r^8}{(r+r_\star)^2}} \\ & + \frac{a\left[r(r_- + r_+) - r_\star^2\right]\left[\,\left(p_t^2-1\right)r^2 + r(r_- + r_+) - r_\star^2\right]}{a^2\left[p_t^2 r^2\left[r^2 + r(r_- + r_+) - r_\star^2\right] + \left[r_\star^2 - r(r_- + r_+)\right]^2\right] + \frac{p_t^2 r^8}{(r+r_\star)^2}} \end{aligned} \quad (1.85)$$

We can examine the effect of ϵ on the angular velocity by referring to Fig. 1.7. The figure shows that Ω_+ always remains positive, while Ω_- can take both positive and negative values. Moreover, it is clear that as ϵ increases, Ω_+ increases, while Ω_- decreases. For the timelike circular orbit, we can write the four momentum as $p_\pm^\alpha = p^t(1, 0, 0, \Omega_\pm)$. The equation governing the circular motion of a timelike particle is derived by applying the normalization condition together with the expression for the particle's four momentum

$$\left(g_{\phi\phi}p_t^2 + g_{t\phi}^2\right)\Omega^2 \;+\; 2g_{t\phi}\left(p_t^2 + g_{tt}\right)\Omega + g_{tt}\left(p_t^2 + g_{tt}\right) = 0\,, \quad (1.86)$$

where we have denoted $p_t = -(\mathcal{E} + qA_t/m)$. Solving the above equation for Ω gives the angular velocity of the timelike particle (see details, for example [99,101])

1.4 Conclusion

In this chapter, we constrained the quantum correction parameter ξ for QCBHs using QPO observations from X-ray binaries, along with the perihelion shifts of Mercury in the Solar System and the S2 star in SgrA* SMBH environment.

We analyzed the effect of the quantum correction parameter ξ on the motion of a particle moving in the equatorial plane around the QCBH. We derived an analytical expression for the perihelion shift in the case of elliptical motion. Our results indicate that the perihelion shift decreases as the parameter ξ increases (see Fig. 1.1). By calculating the perihelion shifts of Mercury and the S2 star and comparing the results with observational data, we evaluated the upper bounds of ξ to be $\xi \leq 0.01869$ for Mercury and $\xi \leq 0.73528$ for the S2 star.

We utilized QPOs to estimate the parameter ξ in strong gravitational field regime conditions. We derived expressions for the radial (ν_r) and latitudinal (ν_θ) frequencies of a test particle in the QCBH spacetime.Our analysis showed that these frequencies decrease the parameter as ξ increases (see Figs. 1.2 and 1.2.4). Using the Markov Chain Monte Carlo (MCMC) method, we constrained the limiting values of the parameter ξ for four X-ray binaries. As a result, we obtained an upper limit of the parameter $\xi \leq 2.086$, providing tighter constraints compared to previous studies based on BH shadows, such as those for M87 ($\xi \leq 2.304$) and Sgr A* ($\xi \leq 2.866$) [45, 46].

We also investigated the effects of LQG corrections on particle motion around LQBHs. By placing an LQBH in an external asymptotically uniform magnetic field, we analyzed the impact of the quantum (correction) parameter ϵ on the dynamics of particles in its vicinity. We analyzed the impact of the parameter ϵ on the horizon and ergosphere of the LQBH, showing that both the outer event horizon and the outer static limit surface contract as ϵ increases for a fixed spin parameter a (see Fig. 1.5). However, the ergosphere region expands under these conditions. A similar trend is observed for the ergosphere when ϵ is held constant, and a increases. To investigate the effect of ϵ on the dynamics of charged particle, we defined the effective potential V_{eff}. Our analysis revealed that as ϵ increases, unstable orbits contract, stable orbits expand, and the height of the effective potential increases. Conversely, under the influence of a magnetic field, the height of the effective potential decreases, and both stable and unstable orbits are compressed closer to the center (see Fig. 1.6).

These findings suggest that quantum gravitational effects are less significant in weak gravitational fields, where the parameter ξ is smaller. In contrast, the influence of the quantum correction parameter becomes more pronounced in strong gravitational fields, as evidenced by the larger upper bound of the parameter ξ obtained from QPO observations.

From an astrophysical perspective, understanding what properties distinguish LQBHs from classical BHs is crucial. This requires examining the effects of quantum corrections on the BH horizon, ergosphere, and the dynamics of particles in its vicinity. However, due to the vast distances to BHs, distinguishing between classical and quantum effects through direct observations remains a significant challenge. Our results provide new insights into the role of the quantum corrections. Future high-precision observations, particularly with next-generation telescopes, are expected to refine these constraints further, advancing our understanding of quantum gravitational phenomena.

Chapter II

Energetics of black holes in loop quantum gravity

2.1 Introduction

One of the most intriguing phenomena surrounding BHs is the Penrose process [102, 103], which was first proposed by Roger Penrose in 1971 as a mechanism for extracting energy from BHs. In the classical version of the process, a particle near the event horizon of a rotating BH splits into two parts: one falls into the BH, while the other escapes. The particle falling into the BH carries negative energy, which reduces the BH's spin, while the particle escaping the BH can carry away positive energy, resulting in net energy extraction [104]. This process is thought to occur in the ergosphere, a region outside the event horizon where the BH's rotation drags spacetime itself, facilitating such particle interactions [105–107]. On the other hand, the magnetic Penrose process (MPP) [100, 108–111], a variant of this mechanism, occurs in the presence of a magnetic field and plays a crucial role in the energy dynamics of astrophysical BHs. It is particularly relevant in the context of BH accretion disks and relativistic jets observed in Active Galactic Nuclei (AGN), where strong magnetic fields are believed to assist in the extraction of energy from the BH [112]. The efficiency of the MPP, which is influenced by factors such as the BH's spin and the magnetic field configuration, is thought to be responsible for some of the most energetic phenomena observed in the universe, such as high-energy particle acceleration [113] and relativistic jets [114].

However, much of the current understanding of the MPP relies on a classical description of BHs. The role of quantum effects, specifically those predicted by gravity theories motivated by quantum mechanics such as LQG, in modifying these energy extraction mechanisms remains largely unexplored. Given that LQG proposes a fundamentally different description of BHs, particularly in the region near the event horizon, it is essential and interesting to investigate how quantum gravitational effects might alter the MPP. In this context, the Immirzi and polymeric parameters in LQG could potentially influence the geometry of the BH, modifying both the ergosphere and the event horizon, and thereby affecting the efficiency of energy extraction. For instance, quantum corrections to the Schwarzschild geometry can significantly impact geodesic motion and energy extraction processes [115]. Similarly, the spinning LQG BH model, which is singularity-free and allows for spins greater than those of Kerr BHs, shows promise as a cosmic particle accelerator, further emphasizing the influence of quantum gravity parameters on particle dynamics and energy extraction mechanisms [116].

Additionally, the astrophysical relevance of this study is significant, as it could provide new insights into the energy dynamics of astrophysical BHs, such as those found at the centres of galaxies. By constraining the mass and magnetic field of LQGBHs for well-known BH candidates such as Sgr $A^\star$ [117,118], M87* [86], NGC 1052 [84], and BZ [81], we examine the potential for these objects to accelerate high-energy protons and power relativistic jets. Furthermore, we explore the variation in energy for accelerated protons from Sgr $A^\star$ post-beta decay as a function of the quantum parameter ϵ and the magnetic field strength B, highlighting the observable signatures of LQG in astrophysical environments.

The motivation for this research lies in the possibility that LQG may significantly alter our understanding of highly energetic phenomena (such as AGNs, relativistic jet particle acceleration, etc.) in the vicinity of a BH. If quantum gravity effects impact the Penrose process, we may gain new insights into the observable properties of BH, including energy extraction, particle acceleration, and the role of magnetic fields in these processes. The exploration of Loop Quantum BHs (LQBHs) and their energy extraction mechanisms opens up a new avenue for theoretical and observational studies in BH physics, with potential implications for future experiments in observational astrophysics.

This study is also highly relevant in the context of current and future advancements in modern astrophysics. As gravitational wave astronomy [119–121] and Event Horizon Telescope (EHT) [122–125] observations continue to provide unprecedented views of BHs and their surroundings, the role of quantum effects in BH dynamics may become increasingly important. The growing interest in the study of BH mergers, the nature of BH horizons, and the behavior of accretion disks and relativistic jets necessitates an understanding that goes beyond classical . Quantum gravity models, like LQG, offer promising pathways to better understand phenomena that were once thought to be the domain of classical physics alone. The results of this study could inform the interpretation of future observations, such as the detection of gravitational waves from BH mergers or the imaging of BH shadows, and may provide key insights into the fundamental nature of spacetime itself.

The Penrose process has also been applied in the context of Buchdahl stars [111] and higher dimensional rotating black holes [105,107,110]. The extraction of more energy from black hole strongly depends on the case for which the incident particle must be relativistic [126, 127]. For that, the PP was reformulated as the magnetic Penrose process, which allows an escaping particle to surpass the constraint velocity for being relativistic. This mechanism significantly enhances the efficiency of energy extraction from rotating black holes [128, 129]. This mechanism addresses purely magnetic field effects on the energy extraction process from black holes. On these lines, an extensive analysis has since been implemented in various contexts [130–136]). It is important to note that the energy extraction process through these mechanism can require the presence of the ergoregion and can only take place inside this region of rotating black holes. However, the Penrose process can also be extended to non-rotating black holes, i.e., the electric Penrose process using electric field to serve as a high-energy emission astrophysical phenomena (see, for example, [137–143]). The chapter is structured as follows: In Section 2.2, we explore the energetic properties of black holes in LQG. We analyze energy extraction from LQBHs via the Magnetic Penrose Process. In Section 3.5, The astrophysical implications of LQBHs are studied by comparing theoretical predictions with observational data from M87*, Sgr A*, NGC 1052, and Blandford-Znajek (BZ) jet power estimates.

2.2 The energy etraction from LQBH via Magnetic Penrose Process

In the ergoregion of a rotating BH, a particle can have negative energy, which allows for the possibility of extracting energy from the BH. The process was first theoretically described by Penrose [102], who proposed that a particle in the ergoregion could split into two parts. One part falls into the BH, while the other escapes. As a result, the energy of the escaping particle is greater than the energy of the original particle, effectively extracting energy from the BH. Further, we focus on the MPP [100,108,110] to analyze the purely magnetic field effect on the energy extraction from LQBHs.

Consider a neutral particle $q_1 = 0$ that falls into a BH and splits into two particles within the ergoregion. Let us denote the energies and charges of the initial particle and the two resulting particles as (E_1, q_1), (E_2, q_2) and (E_3, q_3), respectively. We assume that the second particle, with mass m_2, falls into the BH carrying energy $E_2 < 0$, while the third particle, with mass m_3, escapes the BH with energy $E_3 = E_1 - E_2$, which exceeds the energy of the original particle, i.e., $E_3 > E_1$. The following conservation laws can be written for this process:

$$\begin{aligned} E_1 &= E_2 + E_3\,, && (2.1)\\ L_1 &= L_2 + L_3\,, && (2.2)\\ m_1 &= m_2 + m_3\,, && (2.3)\\ q_1 &= q_2 + q_3\,. && (2.4) \end{aligned}$$

Following [81,101], the four-momentum can yield as

$$m_1 u_1^\alpha = m_2 u_2^\alpha + m_3 u_3^\alpha\,, \tag{2.5}$$

satisfying the conservation laws. Using Eq. (1.83), we can express the relation $u_i^\phi = \Omega\, u_i^t = -\Omega\Lambda_i/\Gamma_i$ for four-velocity components of the particles. Consequently, Eq. (2.5) can be rewritten in the following form

$$\Omega_1 m_1 \Lambda_1 \Gamma_2 \Gamma_3 = \Omega_2 m_2 \Lambda_2 \Gamma_3 \Gamma_1 + \Omega_3 m_3 \Lambda_3 \Gamma_2 \Gamma_1\,, \tag{2.6}$$

where $\Lambda_i = \mathcal{E}_i + q_i A_t/m_i$ and $\Gamma_i = g_{tt} + g_{t\phi}\Omega_i$. After performing some simplifications, we arrive at the following equation:

$$\frac{E_3 + q_3 A_t}{E_1 + q_1 A_t} = \left(\frac{\Omega_1\Gamma_2 - \Omega_2\Gamma_1}{\Omega_3\Gamma_2 - \Omega_2\Gamma_3}\right)\frac{\Gamma_3}{\Gamma_1}\,. \tag{2.7}$$

From the above equations, one can write the escaping particle's energy E_3 as follows

$$E_3 = \chi \left(E_1 + q_1 A_t \right) - q_3 A_t \,, \tag{2.8}$$

where we define χ as

$$\chi = \left(\frac{\Omega_1 - \Omega_2}{\Omega_3 - \Omega_2} \right) \frac{\Gamma_3}{\Gamma_1} \,, \tag{2.9}$$

with $\Omega_1 = \Omega$, $\Omega_2 = \Omega_-$ and $\Omega_3 = \Omega_+$. Now, we move on to determine the expression of efficiency:

$$\eta = \frac{E_{gain}}{E_{initial}} = \frac{E_3 - E_1}{E_1} \,. \tag{2.10}$$

Taking the initial condition $q_1 = q_2 + q_3 = 0$ and Eq. (2.8) into account, Eq. (2.10) can be written as follows:

$$\eta = \left(\frac{\Omega - \Omega_-}{\Omega_+ - \Omega_-} \right) \left(\frac{g_{tt} + \Omega_+ g_{t\phi}}{g_{tt} + \Omega \, g_{t\phi}} \right) - 1 - \frac{q_3 A_t}{E_1} \,. \tag{2.11}$$

The closer the splitting process occurs to the horizon, the higher the efficiency. When the splitting happens at the horizon (r_H), the efficiency reaches its maximum value

$$\eta_{max} \;=\; \frac{1}{2} \left(\sqrt{1 - \frac{(r_H - r_-)(r_H - r_+)}{r_H^2}} - 1 \right) + \beta \frac{a \left(2r_H^2 - r_H(r_- + r_+) + r_- r_+ \right)}{2r_H^2}, \tag{2.12}$$

where we have denoted

$$\beta = \frac{q_3 BGM}{c^2 E_1} \sim \frac{qBGM}{mc^4} \,, \tag{2.13}$$

which, as stated earlier, represents the dimensionless magnetic field parameter. Here, we normalize the spin parameter as $a \to a/M$.

Let us now examine how the parameters a, β, and ϵ affect the efficiency. The top row of Fig. 2.1 shows the efficiency η as a function of a for various values of β,

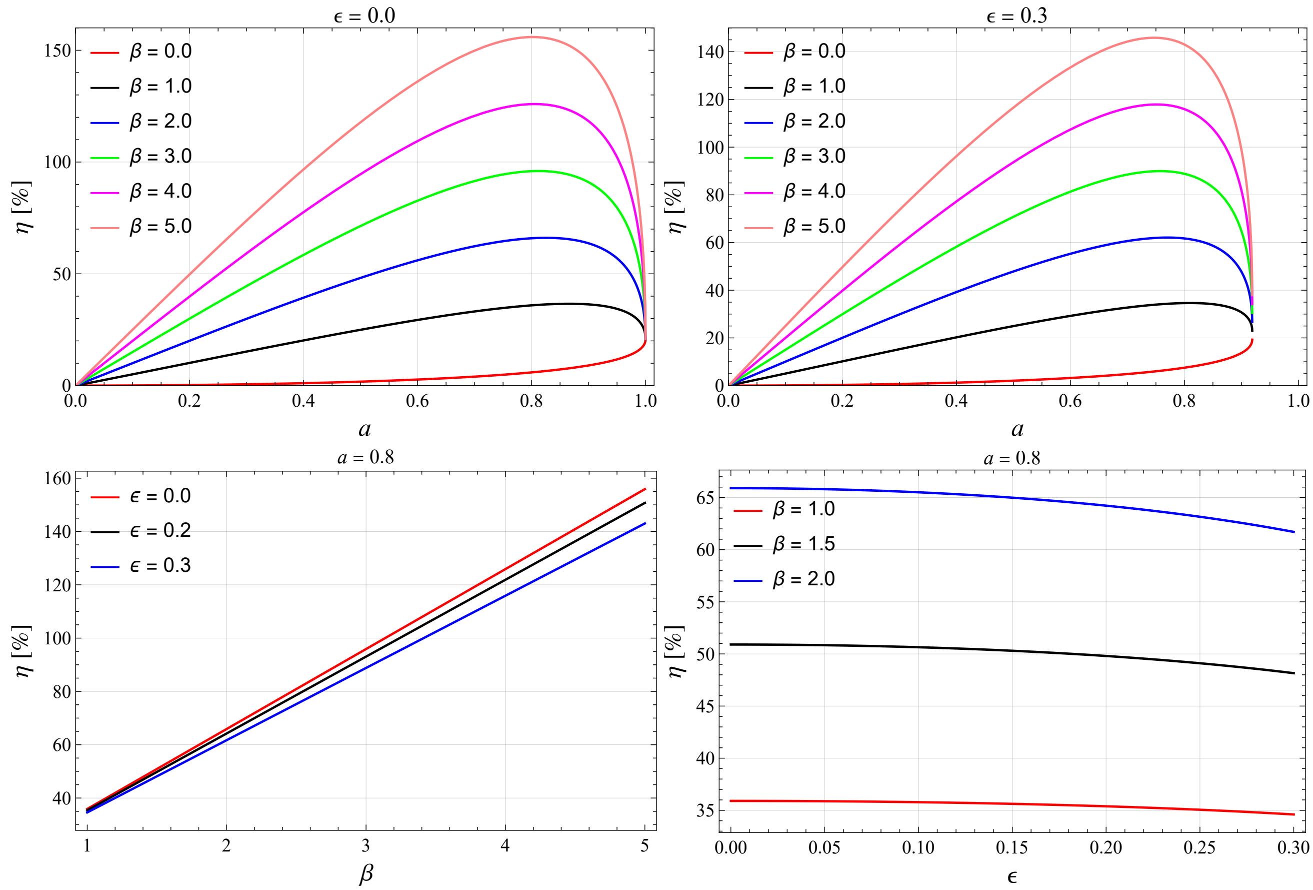

Figure 2.1: The graphs show the impact of ϵ on the efficiency. The top row shows the relationship between the efficiency η and the spin parameter a for the two cases $\epsilon = 0.0$ and $\epsilon = 0.3$. In the bottom row, η is plotted as a function of the magnetic field parameter β for various possible values of ϵ (left), and as a function of ϵ for different values of β (right) with fixed $a = 0.8$.

under the conditions $\epsilon = 0.0$ and $\epsilon = 0.3$. The bottom row illustrates efficiency as a function of both ϵ and β, considering different values of these parameters. As shown in the top-right figure, the efficiency of the Magnetic Penrose Process increases with BH spin due to stronger frame-dragging and magnetic interactions, but drops near maximal spin as magnetic field lines are expelled from the horizon [144]. When the spin parameter a approaches its maximum value, $a \to a_{\max}$ (approximately $a = 0.919$ in the top right), the efficiency is about 19.3%. This is slightly lower than the 20.7% efficiency observed in the Kerr case at $a = 1$ (as seen in the top-left figure). From the top row of the figure, it is evident that when $\epsilon = 0$, the maximum efficiency reaches approximately 150%. In contrast, for $\epsilon = 0.3$, the efficiency decreases to around 140%. Thus, an increase in ϵ leads to a reduction in both the maximum efficiency and the spin parameter. This trend is more apparent in the bottom row of Fig. 2.1. In the bottom-left figure, efficiency is plotted as a function of the magnetic parameter β for various values of ϵ. It is evident that as β increases, efficiency also increases; however, as ϵ increases, the slope of the lines decreases. Similarly, in the bottom-right figure, efficiency is shown as a function of ϵ for different values of β. Here, we observe that efficiency increases with β but decreases as ϵ becomes larger. The decrease in efficiency and spin parameters with increasing ϵ is attributed to the impact of ϵ on the ergosphere and horizon. This relationship, illustrating the reduction of horizon and ergosphere with increasing ϵ, is depicted in Fig. 1.5.

2.3 Astrophysical applications of LQBHs Using M87*, SgrA*, NGC 1052, and BZ Observations

In this section, we explore the astrophysical applications of the MPP around LQBHs. Here, we focus on the amount of energy it can transfer to protons via MPP. This investigation offers valuable insights into the potential sources responsible for accelerating protons observed in cosmic rays. Suppose a neutron experiences beta decay very close to the surface of LQBH's horizon. This process can be described as follows [145–147]:

$$n^0 \to p^+ + W^- \to p^+ + e^- + \overline{\nu}_e \,. \tag{2.14}$$

In this process, the initial particle is a neutron n^0, and the escaping particle is a proton p^+. Let's calculate the energy of the escaping proton. From Eqs. (2.10) and (2.12), we can define the maximum energy of the escaping proton as follows

$$\begin{aligned} E^{p^+}_{max} &= \frac{1}{2}\left(\sqrt{1-\frac{(r_H-r_-)(r_H-r_+)}{r_H^2}}+1\right)m_n c^2 \\ &+ \frac{eBGM}{c^2}\cdot\frac{a\,(2r_H^2-r_H(r_-+r_+)+r_-r_+)}{2r_H^2}, \end{aligned} \tag{2.15}$$

where r_H is the horizon of the LQBH.

Let us now explore how ϵ influences the energy of the escaping particle. To illustrate this, Table 2.1 presents the calculated energy of the escaping proton for various values of epsilon across different BH candidates. From the Table 2.1, we observe that the acceleration capabilities of these BHs depend on their mass, the magnetic field strength in their vicinity, and the parameter ϵ. As the mass and magnetic field strength increase, the energy of the accelerated particle also increases. However, an increase in ϵ reduces the particle's energy.

Source	Mass $[M_\odot]$	B [G]	E_{p^+} [eV]				
			$\epsilon = 0.0$	$\epsilon = 0.1$	$\epsilon = 0.2$	$\epsilon = 0.3$	
SgrA*	4.0×10^6	100	4.094	4.088	4.071	4.041	$\times 10^{15}$
M87*	6.2×10^9	30	1.904	1.901	1.893	1.879	$\times 10^{18}$
BZ	1.0×10^9	10^4	1.024	1.022	1.018	1.010	$\times 10^{20}$
NGC 1052	1.6×10^8	8×10^4	1.297	1.296	1.291	1.281	$\times 10^{20}$

Table 2.1: The table shows the impact of ϵ to the energy of escaping protons accelerated by different BHs. The energy of protons are calculated for various values of ϵ. In this calculations, we set $a = 0.5$, which is the dimensionless spin parameter.

For a more in-depth analysis of the contribution of BH candidates to the cosmic ray spectrum through the production of high-energy cosmic rays, the top left panel of Fig. 2.2 presents the current constraints on their masses and magnetic field strengths, along with the critical energy points in the cosmic ray spectrum. The vertical green lines in the figure represent the range of magnetic field strengths inferred from observational data for various BH candidates (see, e.g., [84, 86, 118, 148]). The solid black, blue and pink lines shows the energy of the escaping particle when $\epsilon = 0$, indicating the transition of the LQBH to a Kerr BH.

The red lines indicate the Greisen-Zatsepin-Kuzmin (GZK) limit, commonly known as the cutoff effect. This limit defines the maximum energy that protons can achieve while traveling across the intergalactic medium from distant galaxies to our galaxy. Theoretically, this cutoff energy is estimated to be approximately 5×10^{19} eV [149]. This limit arises from interactions between high-energy protons and the cosmic microwave background radiation over large-scale intergalactic

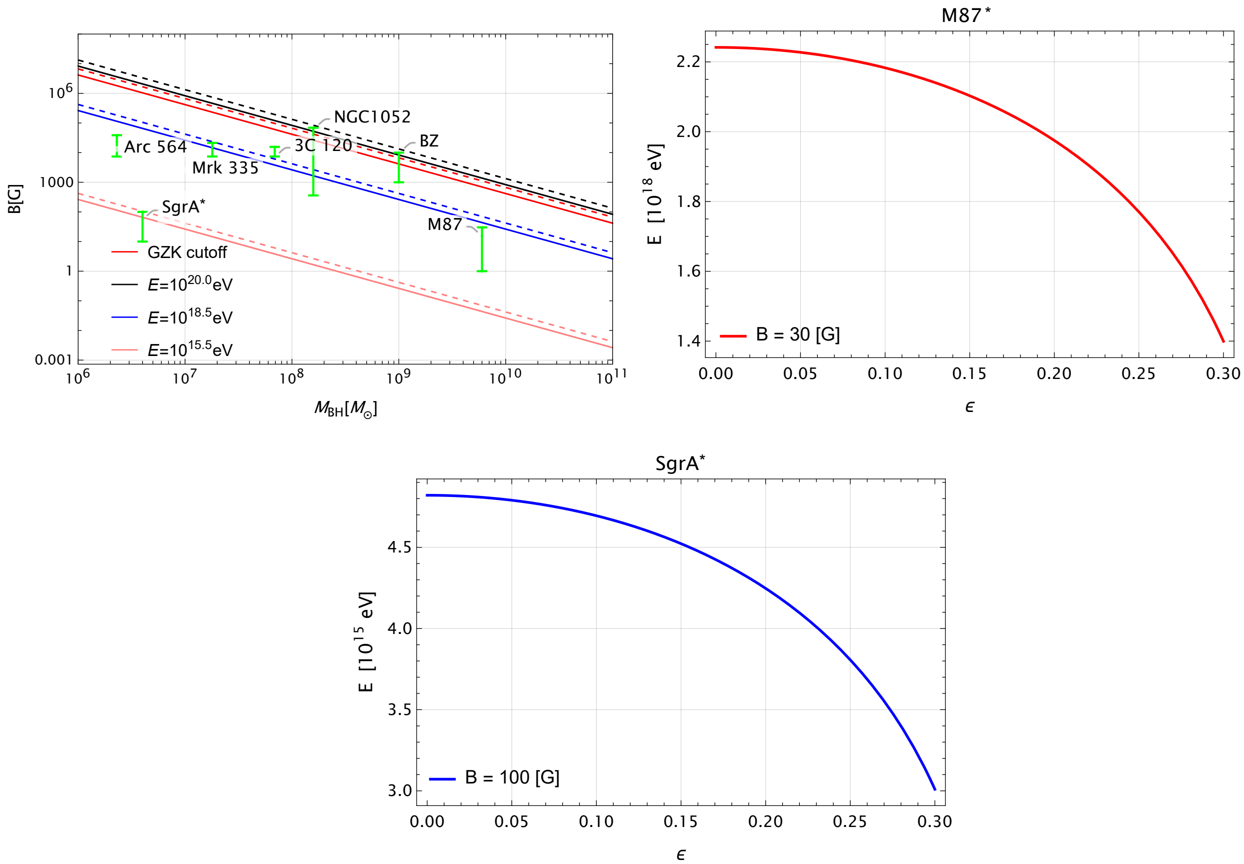

Figure 2.2: The top left panel shows the constraint plot of BH mass $M_{\rm BH}$ and magnetic field B for selected BH candidates, which could serve as sources of high-energy protons at different energy levels. The source labeled as BZ corresponds to a supermassive BH with a mass $10^9 M_\odot$ and a magnetic field strength ranging from 10^3 G to 10^4 G, consistent with the Blandford & Znajek model of relativistic jets [81]. The lines depict various proton energies along with the GZK cutoff limit. The solid lines correspond to $\epsilon = 0$, representing a Kerr BH, while the dashed lines represent $\epsilon = 0.3$ case. The top right and bottom panel display the energy E of protons accelerated by M87* and SgrA* after beta decay as a function of ϵ, plotted for the corresponding mass $M = 6.2 \times 10^9\, M_\odot$ and $M = 4 \times 10^6\, M_\odot$, respectively. In all plots, the spin parameter is set to $a = 0.9$.

distances. The dashed lines illustrate the case of $\epsilon \neq 0$, showing the mass and magnetic field strength required for a BH to accelerate particles to these energies as an LQBH. The figure demonstrates that as ϵ increases, a stronger magnetic field is required to accelerate a particle to the given energy. Additionally, it highlights that SgrA* serves as a source of cosmic rays at the knee energy, while NGC 1052 is associated with cosmic rays at the ankle energy or in the ultra-high-energy range.

These energy lines signify critical features in the cosmic ray spectrum. For instance, beyond the knee energy (10^{15}–10^{16} eV), the flux of cosmic ray particles drops significantly, indicating a sharp transition in the spectrum. In contrast, beyond the ankle energy ($10^{18.5}$ eV), the spectrum flattens, reflecting a change in the dominant sources. The top right and bottom panel of Fig. 2.2 show the effect of ϵ on the energy of protons accelerated by SgrA* and M87*. It can be seen from the figure that as ϵ increases, the energy of the protons decreases.

2.4 Conclusion

By placing an LQBH in an external asymptotically uniform magnetic field, we analyzed the impact of the quantum (correction) parameter ϵ on the efficiency of the MPP in its vicinity. Furthermore, we explored the particle acceleration capabilities of the MPP by calculating the energy of accelerated protons for various BH candidates, considering current observational constraints on their magnetic field strengths and masses.

From an astrophysical perspective, LQBHs are considered important objects for studying quantum effects in strong gravitational fields. Therefore, studying their energetic properties, such as particle acceleration, energy extraction, and the influence of magnetic fields on these processes, is crucial for understanding the nature and observable parameters of LQBHs. This research can provide a foundation for future studies on the observation and detection of LQBHs. Therefore, we utilized the MPP to explore the energetic properties of LQBHs. For the LQBH, the efficiency of the MPP can also exceed 100%; however, we have demonstrated that increasing ϵ slightly reduces the efficiency. In the extreme spin case, we found that when $\epsilon = 0$, i.e., for a Kerr BH, the efficiency is the well-known 20.7%, whereas, for $\epsilon = 0.3$, it decreases to 19.3%. But, with the increasing of magnetic field, the efficiency always increases (see Fig. 2.1).

Additionally, we explored the acceleration properties of the MPP and evaluated the energy of escaping protons for various BHs (see Table 2.1). To illustrate the role of various BHs in producing high-energy cosmic rays, we estimated their cosmic ray-producing capacity at key points in the cosmic ray spectrum, based on current constraints on their masses and magnetic fields (see, e.g., [84,86,118,148]). We demonstrated that these BHs, as LQBHs, would require a stronger magnetic field to accelerate particles to the energies achieved by Kerr BHs (see the left panel in Fig. 2.2). Furthermore, a stronger magnetic field is also necessary to generate energy at the GZK cutoff limit under the influence of ϵ. We analyzed the effect of ϵ on the capability of the BH SgrA* at the center of our Milky Way Galaxy to accelerate protons and found that the energy of the accelerated protons decreases as ϵ increases (see the right panel in Fig. 2.2).

From an astrophysical perspective, understanding what properties distinguish LQBHs from classical BHs is crucial. This requires examining the effects of quantum corrections on the BH horizon, ergosphere, and the energetic processes occurring in its vicinity. However, due to the vast distances to BHs, distinguishing between classical and quantum effects through direct observations remains a significant challenge.

Building on these theoretical foundations, the approach adopted in this study is critical for uncovering the unique characteristics of LQBHs. By analyzing the influence of the LQG correction parameter ϵ on the MPP, our work provides deeper insights into the distinctive energetic properties of LQBHs. This research not only enhances our understanding of quantum gravity effects in astrophysical observations but also lays the groundwork for future studies on the detectability and observational signatures of LQBHs. Given the importance of high-energy processes around astrophysical BHs, our findings are astrophysically significant because they do not preclude the influence of LQBHs, which could be sources of highly energetic phenomena and play a crucial role in explaining these powerful events.

Chapter III

Astrophysical insights into energetics of parameterized Konoplya-Rezzolla-Zhidenko black hole spacetime

3.1 Introduction

Theoretical models and simulations have shown that BHs can act as cosmic engines, converting gravitational energy into electromagnetic radiation and kinetic energy [150]. Among the various mechanisms proposed to explain these extraordinary energy outputs, the geometric Penrose process (PP) is particularly noteworthy. Initially theorized by Roger Penrose in the 1960s, this process describes how energy can be extracted from a rotating BH through the disintegration of particles within the ergosphere [102]. The ergosphere, a region outside the event horizon where spacetime is dragged by the BH's rotation, allows for particle interactions that can result in one particle falling into the BH with negative energy while the other escapes with more energy than the original particle [151]. The gravitomagnetic monopole charge can also influence the ergosphere region, contributing to the energy extraction via the PP [106]. Later, the energy extraction process was considered for higher-dimensional BHs using the PP [107]. Additionally, recent studies have explored the energy-extraction process in the context of quantum Schwarzschild geometry, where the process can violate the null energy condition [115]. This violation opens up new possibilities for understanding the underlying physics of BHs and the mechanisms of energy extraction. Further research has also investigated superradiant energy extraction from rotating hairy Horndeski BHs [152] and harvesting energy driven by the magnetic reconnection process from rotating BHs [153–158], providing additional insights into the diverse mechanisms of energy extraction in different BH models.

The presence of a magnetic field around a BH significantly amplifies the energy extraction mechanism known as the MPP [159]. This magnetic Penrose process leverages the interaction between the BH's rotational energy and external magnetic fields to produce extraordinary energy outputs [128, 131, 132, 160, 161]. The reconnection and twisting of magnetic fields accelerate particles to relativistic speeds, forming powerful jets that can stretch thousands of light-years from the BH's poles [162]. These jets not only impact the interstellar medium but also play a role in the evolution of galaxies [163]. By explaining ultra-high-energy cosmic rays and high-energy gamma-ray bursts, the MPP provides insights into some of the universe's most energetic phenomena [164, 165]. Additionally, recent research highlights that magnetic fields can significantly boost the efficiency of the MPP, leading to substantial energy extraction manifesting as high-energy radiation or particle emissions [101, 110, 111]. This underscores the MPP's importance in understanding high-energy astrophysical events.

Understanding the MPP requires a comprehensive analysis of the BH's spacetime geometry and the behavior of charged particles in the presence of strong gravitational and electromagnetic fields. In this chapter, we focus on a specific BH solution: the parameterized Konoplya-Rezzolla-Zhidenko (KRZ) BH. This solution describes a rotating parameterized KRZ BH [28,29] subjected to an external magnetic field. By examining this scenario, we aim to uncover the conditions and regions where significant energy extraction can occur, thereby enhancing our understanding of high-energy astrophysical processes.

The parameterized KRZ BH, characterized by *six deformation parameters*, provides a unique environment for studying the effects of magnetization on energy extraction processes [166]. Recent investigations into the parameters of the spherically symmetric parametrized Rezzolla-Zhidenko spacetime have provided critical insights through solar system tests, the orbit of the S2 star about Sgr $A^{\star}$, and quasiperiodic oscillations, highlighting the broader applicability and accuracy of this parameterized model in various astrophysical contexts [167]. In the presence of an external magnetic field, the dynamics of charged particles around such a BH become increasingly complex. These particles can experience significant accelerations and energy gains, leading to potential high-energy phenomena observable from Earth [168,169]. Investigating these dynamics helps elucidate magnetic fields' role in BH environments and their impact on surrounding astrophysical processes. In this chapter, we consider the MPP in the parameterized KRZ BH spacetime. By shedding light on the MPP, we aim to contribute to the broader understanding of high-energy phenomena in the vicinity of the parameterized KRZ BHs and the fundamental mechanisms driving these cosmic events. Our study not only advances theoretical knowledge but also lays the groundwork for future observational and experimental efforts to explore the extreme environments around BHs.

3.2 The parameterized Konoplya-Rezzolla-Zhidenko BH spacetime metric and its electromagnetic field

Here, we consider an interesting parameterized BH metric, usually referred to as the parameterized Konoplya-Rezolla-Zhidenko (KRZ) spacetime, which in Boyer-Lindsquist coordinates is given by [28, 29].

$$\begin{aligned} ds^2 = &-\frac{N^2 - W^2\sin^2\theta}{K^2}dt^2 - 2Wr\sin^2\theta dt d\phi + \\ &+K^2r^2\sin^2\theta d\phi^2 + \frac{\Sigma Z^2}{N^2}dr^2 + \Sigma r^2 d\theta^2 \ , \end{aligned} \tag{3.1}$$

where

$$\begin{aligned} N^2 = &\left(1 - \frac{r_0}{r}\right)\left(1 - \frac{\epsilon_0 r_0}{r} + (k_{00} - \epsilon_0)\frac{r_0^2}{r^2} + \frac{\delta_1 r_0^3}{r^3}\right) + \\ &+ \left(\frac{a_{20}r_0^3}{r^3} + \frac{a_{21}r_0^4}{r^4} + T\right)\cos^2\theta, \end{aligned} \tag{3.2}$$

$$Z = 1 + \frac{\delta_4 r_0^2}{r^2} + \frac{\delta_5 r_0^2}{r^2}\cos^2\theta, \tag{3.3}$$

$$W = \frac{1}{\Sigma}\left(\frac{\omega_{00}r_0^2}{r^2} + \frac{\delta_2 r_0^3}{r^3} + \frac{\delta_3 r_0^3}{r^3}\cos^2\theta\right), \tag{3.4}$$

$$K^2 = 1 + \frac{aW}{r} + \frac{1}{\Sigma}\left(\frac{k_{00}r_0^2}{r^2} + \left(\frac{k_{20}r_0^2}{r^2} + T\right)\cos^2\theta\right), \tag{3.5}$$

$$T = \frac{k_{21}r_0^3}{r^3\left(1 + \frac{k_{22}\left(1 - \frac{r_0}{r}\right)}{1 + k_{23}\left(1 - \frac{r_0}{r}\right)}\right)}, \tag{3.6}$$

$$\Sigma = 1 + \frac{a^2}{r^2}\cos^2\theta, \tag{3.7}$$

with the dimensionless spin parameter $a = J/M^2$ and the event horizon $r_0 = 1 + \sqrt{1 - a^2}$. We also defined following parameters

$$\epsilon_0 = \frac{2 - r_0}{r_0}, \qquad a_{20} = \frac{2a^2}{r_0^3}, \qquad a_{21} = -\frac{a^4}{r_0^4} + \delta_6,$$
$$\omega_{00} = \frac{2a}{r_0^2}, \qquad k_{00} = k_{23} = \frac{a^2}{r_0^2}, \qquad k_{21} = \frac{a^4}{r_0^4} - \frac{2a^2}{r_0^3} - \delta_6,$$
$$k_{20} = 0, \qquad k_{22} = -\frac{a^2}{r_0^2}. \tag{3.8}$$

It is to be emphasized that the parameterized Konoplya-Rezolla-Zhidenko (KRZ) spacetime metric can deviate from the Kerr metric. We then consider these deviations, which can be further introduced by six deformation parameters denoted as $\{\delta_i\}$ (where $i = 1, 2, ..., 6$) that characterize the deviations. From physical point of view, these deformation parameters can be interpreted as follows:

- $\delta_1 \rightarrow$ corresponds to deformations of g_{tt},
- $\delta_2, \delta_3 \rightarrow$ correspond to rotational deformations of the metric,
- $\delta_4, \delta_5 \rightarrow$ correspond to deformations of g_{rr},
- $\delta_6 \rightarrow$ correspond to deformations of the event horizon.

It is evident from the KRZ metric that it reduces to the Kerr metric exactly when considering all $\delta_i \rightarrow 0$. We note that the sign of the spin parameter a can be incorporated into the first two parameters $\{\delta_2, \delta_3\}$ and by redefining the time coordinate t, we only consider $a > 0$. Notably, among the six deformation parameters, the first two parameters $\{\delta_1, \delta_2\}$ we aim to explore are the most crucial parameters for gaining a deeper understanding of their unique aspects and nature. Note that in the equatorial plane, all parameters are reduced, leaving only δ_1 andδ_2. Therefore, for simplicity and further analysis, we shall restrict motion to the equatorial plane (i.e., $\theta = \pi/2$) and only focus on these two parameter, δ_1

and δ_2. Based on the reports of the x-ray observations for the supermassive BH in Ark 564, δ_1 and δ_2 vary in the following range (see details [170])

$$-0.27 < \delta_1 < 0.28 \quad \text{and} \quad -0.37 < \delta_2 < 0.22\,. \tag{3.9}$$

Examining the role of magnetic fields near a BH is crucial from an astrophysical perspective. We further consider the magnetic field surrounding the parameterized KRZ BH. For that, the BH is considered to be immersed in an external magnetic field that is supposed to be uniform at large distances and a weak test field, satisfying the following strengths of the order of $B_1 \sim 10^8$ G and $B_2 \sim 10^4$ G for stellar and supermassive BHs, respectively (see, e.g., in Refs. [83–85]). The point to note is that observational analysis through the binary BH system $V404$ Cygni [171] provided estimates of the magnetic field strength of the order of $B \sim 33.1 \pm 0.9$ G. Additionally, it is worth noting that, recently, the EHT collaborations provided the estimates of the average magnetic field strength, which is of the order of $B \sim 1 - 30$ G with observations at 230 GHz through the polarized synchrotron radiation around the supermassive BH at the center of the M87 galaxy (see, e.g., in Refs. [86,87]). The magnetic field plays a pivotal role in altering a charged particle's geodesics, even though it is too small [172], thus causing a drastic change to the charged particles' motion. The magnetic field's influence on the motion of charged particles has since been widely developed as a well-established formalism in various scenarios(see, e.g. [60, 68, 88–95]). For our purposes, the magnetic field can be considered a weak test field in the curved background spacetime, uniform, and oriented along the axis of the BH's symmetry as that of its asymptotic properties [90, 96, 97]. Using Eq. (1.71), the four-vector potentials for the parameterized

KRZ BH spacetime can be obtained as follows:

$$A_t = B\Bigg(- a\cdot\frac{r^4-r^3+a^2\left(-2+r+r^2-rr_0\right)+rr_0^2\left(2+r_0(-1+\delta_1)\right)-r_0^4\delta_1}{r^4+a^2r(2+r)+ar_0^3\delta_2}+$$
$$+\frac{ar_0^6\delta_2^2-rr_0^3\delta_2\left(a^2(-4+r)+r^3\right)}{2r^2[r^4+a^2r(2+r)+ar_0^3\delta_2]}\Bigg)\,, \tag{3.10}$$

$$A_\phi = \frac{1}{2}Br^2\Bigg(1+\frac{a^2}{r^2}+\frac{a}{r}\Big(\frac{2a}{r^2}+\frac{r_0^3}{r^3}\delta_2\Big)\Bigg)-aBr\Big(\frac{2a}{r^2}+\frac{r_0^3}{r^3}\delta_2\Big)\,. \tag{3.11}$$

where $r_0 = 1+\sqrt{1-a^2}$ is the event horizon of the BH.

3.3 Charged particle dynamics around the parameterized Konoplya-Rezzolla-Zhidenko BH

We further consider charged-particle dynamics around the parameterized KRZ BH immersed in the presence of an external uniform magnetic field. This is what we intend to examine here.

Using Eq. 1.80, the following equation for the timelike radial motion of the charged particle in the equatorial plane (i.e., $\theta = \pi/2$) can be defined by the effective potential

$$V_{\rm eff} = \sqrt{\frac{R\left(H+a^2\beta^2\delta_2^2r_0^6-2a\delta_2rr_0^3\left(\beta\left(a^2\beta(r-2)+\beta r^3-2Lr\right)-2r\right)\right)}{4r^4\left(a^2(r+2)r+a\delta_2r_0^3+r^4\right)^2}}-$$
$$-\frac{\left(2ar+\delta_2r_0^3\right)\left(a^2\beta(r-2)r-a\beta\delta_2r_0^3+\beta r^4-2Lr^2\right)}{2r^2\left(a^2(r+2)r+a\delta_2r_0^3+r^4\right)} \tag{3.12}$$

where

$$\begin{aligned} R &= r^2\left(a^2\left(r^2-rr_0-8\right)+r^4-2r^3+rr_0^2((\delta_1-1)r_0+2)-\delta_1r_0^4\right)\\ &- 8a\delta_2rr_0^3-2\delta_2^2r_0^6\,, \end{aligned} \tag{3.13}$$

$$\begin{aligned} H &= r^2\left[a^4\beta^2(r-2)^2+2a^2r\left(\beta(r-2)\left(\beta r^2-2L\right)+2(r+2)\right)\right]\\ &+ r^2\left[\beta^2r^6-4r^4(\beta L-1)+4L^2r^2\right]\,, \end{aligned} \tag{3.14}$$

with the angular momentum per unit mass of particle $\mathcal{L} = L/m$ and the angular frame dragging velocity $\omega = -g_{t\phi}/g_{\phi\phi}$ for a particle with zero angular momentum.

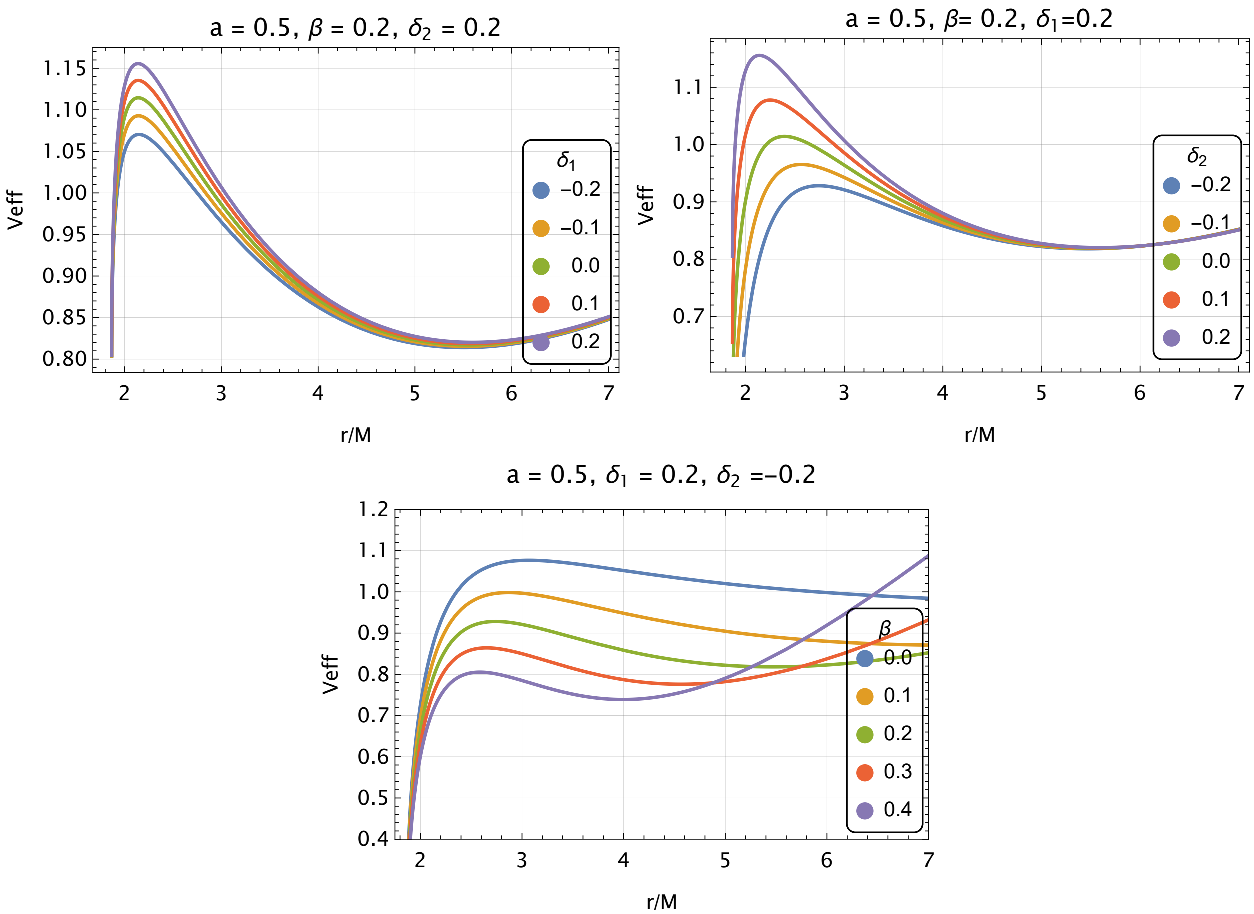

Figure 3.1: The radial profile of the effective potential V_{eff} for different values of the deformation parameters δ_1 (Top left panel), δ_2 (Top right panel), and the magnetic field parameter $\beta = qB/m$ (Bottom panel). Note that we shall for simplicity restrict motion to the equatorial plane, i.e., $\theta = \pi/2$. In all cases, we have set $\delta_3 = \delta_4 = \delta_5 = \delta_6 = 0$.

It is worth noting that the effective potential plays an important role acting as a powerful tool for studying a particle motion around a BH. Based on Eq. (3.12), we further analyze the effective potential for nongeodesic motion of charged test particles around the parameterized KRZ BH in the presence of an external uniform magnetic field. In Fig. 3.1, we show the radial profile of the effective potential for a charged particle orbiting the parameterized KRZ BH for various possible cases of the given magnetic field parameter β and deformation parameters δ_1 and δ_2. In Fig. 3.1, the top left and right panels demonstrate the impact of the deformation parameters, $\delta_{1,2}$, on the radial profile of V_{eff} the effective potential, while the bottom panel depicts the impact of the magnetic field parameter for keeping $\delta_{1,2}$ fixed. As can be seen from the top row of Fig. 3.1, there exist two extreme points, the minimum r_{min} and the maximum r_{max}, in the effective potential, which correspond to stable and unstable circular orbits for particles around the parameterized KRZ BH. It is evident from Fig. 3.1 that the shape of the effective potential is shifted upward towards higher values, but the stable orbits are shifted slightly to the left to smaller r as the deformation parameters $\delta_{1,2}$ increase. Similarly, there is the same behavior for unstable orbits. Unlike the impact of $\delta_{1,2}$, the shape of the effective potential or the maximum is shifted downward towards smaller values, causing the potential barrier to reduce. Stable orbits are significantly shifted to the right to towards the central object as a consequence of the combined effects of the magnetic field parameter and deformation parameters. This results in charged particles not escaping from the pull of gravity but instead being trapped under the gravitational and electromagnetic influences in the close vicinity of the BH.

We now examine the specific energy and angular momentum of the charged particles orbiting on the stable circular orbits, i.e., $\mathcal{E}$ and $\mathcal{L}$. To determine these quantities one needs to solve $V_{eff} = \partial V_{eff}/\partial r = 0$ simultaneously. Additionally, we further consider the innermost stable circular orbits (ISCOs) for which the following standard condition

$$\frac{\partial^2 V_{eff}}{\partial r^2} \geq 0\,, \tag{3.15}$$

must be satisfied to determine the radius of circular orbits. We now provide a more appropriate and detailed analysis for the aforementioned parameters required for charged particles to be on the stable circular orbits around the parameterized

β	$\delta_1 \backslash \delta_2$		-0.2	-0.1	0.0	0.1	0.2
0.0	-0.2	r_{ISCO}	3.9135	3.5765	3.1859	2.7584	2.4120
		$\mathcal{L}_{ISCO}$	2.7563	2.6629	2.5468	2.3963	2.2085
		$\mathcal{E}_{ISCO}$	0.9109	0.9033	0.8924	0.8756	0.8508
	-0.1	r_{ISCO}	3.7571	3.4119	3.0293	2.6597	2.3977
		$\mathcal{L}_{ISCO}$	2.6956	2.5928	2.4647	2.3041	2.1203
		$\mathcal{E}_{ISCO}$	0.9069	0.8980	0.8853	0.8666	0.8422
	0.0	r_{ISCO}	3.6054	3.2617	2.9066	2.6017	2.3969
		$\mathcal{L}_{ISCO}$	2.6312	2.5187	2.3804	2.2156	2.0402
		$\mathcal{E}_{ISCO}$	0.9024	0.8922	0.8778	0.8581	0.8351
	0.1	r_{ISCO}	3.4634	3.1329	2.8181	2.5691	2.4031
		$\mathcal{L}_{ISCO}$	2.5631	2.4417	2.2962	2.1325	1.9670
		$\mathcal{E}_{ISCO}$	0.8975	0.8860	0.8703	0.8506	0.8292
	0.2	r_{ISCO}	3.3356	3.0289	2.7573	2.5519	2.4131
		$\mathcal{L}_{ISCO}$	2.4921	2.3631	2.2143	2.0550	1.8997
		$\mathcal{E}_{ISCO}$	0.8922	0.8796	0.8632	0.8440	0.8244

Table 3.1: The table shows the numerical values of the ISCO parameters $\mathcal{L}_{ISCO}$, $\mathcal{E}_{ISCO}$, and r_{ISCO} of the test particles. They are moving around KRZ parametrized plack hole on the ISCO radius. the magnetic parameter $\beta = 0$. The data is calculated for $a = 0.8$ and $\theta = \pi/2$ case.

KRZ BH. All results are tabulated in Tables 3.1 and 3.2. It can be observed from Table 3.1 that the ISCO radius correspondingly decreases as both the deformation parameters, $\delta_{1,2}$, increase. Similarly, $\mathcal{E}$ and $\mathcal{L}$ of the test particles orbiting on the ISCO decrease due to the influence of both parameters $\delta_{1,2}$. This suggests that the particles can lose their energy and angular momentum due to these deformation parameters when orbiting the ISCO radius around the parameterized KRZ BH. The similar behavior is also observed for these the ISCO parameters when the impact of the magnetic field parameter β is included.

We further consider a particular case for the timelike particle due to a potential barrier on the equatorial plane (i.e., $\theta = \pi/2$). To this end, we assume that the motion of the timelike particle occurs at the circular orbit satisfying $r =$ const and $\theta =$ const). In Eq. (1.84), it is to be emphasized that Ω_+ and Ω_- correspond to the outer and inner photon orbit's angular velocities, respectively.

β	$\delta_1 \backslash \delta_2$		-0.2	-0.1	0.0	0.1	0.2
0.01	-0.2	r_{ISCO}	3.8995	3.5656	3.1777	2.7525	2.4075
		$\mathcal{L}_{ISCO}$	2.7249	2.6339	2.5206	2.3733	2.1888
		$\mathcal{E}_{ISCO}$	0.8978	0.8906	0.8802	0.8640	0.8400
	-0.1	r_{ISCO}	3.7446	3.4024	3.0224	2.6547	2.3935
		$\mathcal{L}_{ISCO}$	2.6654	2.5652	2.4401	2.2827	2.1022
		$\mathcal{E}_{ISCO}$	0.8941	0.8857	0.8735	0.8554	0.8317
	0.0	r_{ISCO}	3.5946	3.2537	2.9008	2.5972	2.3929
		$\mathcal{L}_{ISCO}$	2.6021	2.4925	2.3573	2.1959	2.0235
		$\mathcal{E}_{ISCO}$	0.8899	0.8802	0.8664	0.8473	0.8249
	0.1	r_{ISCO}	3.4540	3.1261	2.8131	2.5650	2.3992
		$\mathcal{L}_{ISCO}$	2.5354	2.4169	2.2747	2.1142	1.9515
		$\mathcal{E}_{ISCO}$	0.8853	0.8743	0.8592	0.8402	0.8194
	0.2	r_{ISCO}	3.3275	3.0230	2.7528	2.5481	2.4092
		$\mathcal{L}_{ISCO}$	2.4658	2.3399	2.1943	2.0381	1.8853
		$\mathcal{E}_{ISCO}$	0.8804	0.8682	0.8525	0.8339	0.8148

Table 3.2: The table shows the numerical values of the ISCO parameters $\mathcal{L}_{ISCO}$, $\mathcal{E}_{ISCO}$, and r_{ISCO} of the test particles. They are moving around KRZ parametrized plack hole on the ISCO radius. the magnetic parameter $\beta = 0.01$. The data is calculated for $a = 0.8$ and $\theta = \pi/2$ case.

Ω_+ is always positive, while Ω_- can be both positive and negative, depending on various combinations of the deformation parameters $\delta_{1,2}$, as shown in Fig. 3.2. In Fig. 3.2, we demonstrate Ω_+ and Ω_- by solid and dashed lines, respectively, for various possible combinations of deformations parameters $\delta_{1,2}$. The Eq. (1.86) then solves to give the angular velocity of the infalling timelike particle as (see details, for example [99, 101])

$$\Omega = \frac{-g_{t\phi}\left(p_t^2 + g_{tt}\right) + \sqrt{\left(p_t^2 + g_{tt}\right)\left(g_{t\phi}^2 - g_{tt}g_{\phi\phi}\right)p_t^2}}{g_{\phi\phi}p_t^2 + g_{t\phi}^2}. \tag{3.16}$$

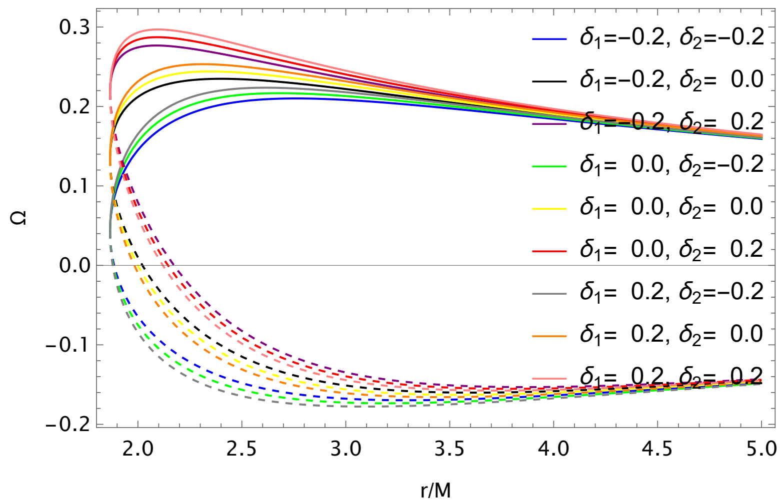

Figure 3.2: The radial behavior of the angular velocity components Ω_+ (solid lines) and Ω_- (dashed lines) for different values of the deformation parameters $\delta_{1,2}$. Note that we have used $a/M = 0.5$ and $\delta_3 = \delta_4 = \delta_5 = \delta_6 = 0$ in this case.

3.4 Energy extraction through the magnetic Penrose process

As mentioned earlier, astronomical observations have revealed high-energy cosmic rays coming from active galactic nuclei(AGN) [173–175]. In order to propose a model that explains the results of these observations, it is valuable to study the geometric PP. This process was first theoretically described by Penrose in 1969 [102]. Since then, different models have been developed to explain the energy extraction mechanisms from BHs and jets in AGNs [176]. The MPP [160] has important consequences for high-energy astrophysical events, generalizing the geometric PP and including the generation of relativistic jets observed in AGN and gamma-ray bursts (GRBs). Due to the presence of the ergoregion located outside the event horizon but inside the static radius, energy can be extracted from the rotating BH in the PP. In this scenario, a massive particle entering the ergosphere is divided into two fragments. The momentum of these fragments allows one to escape to

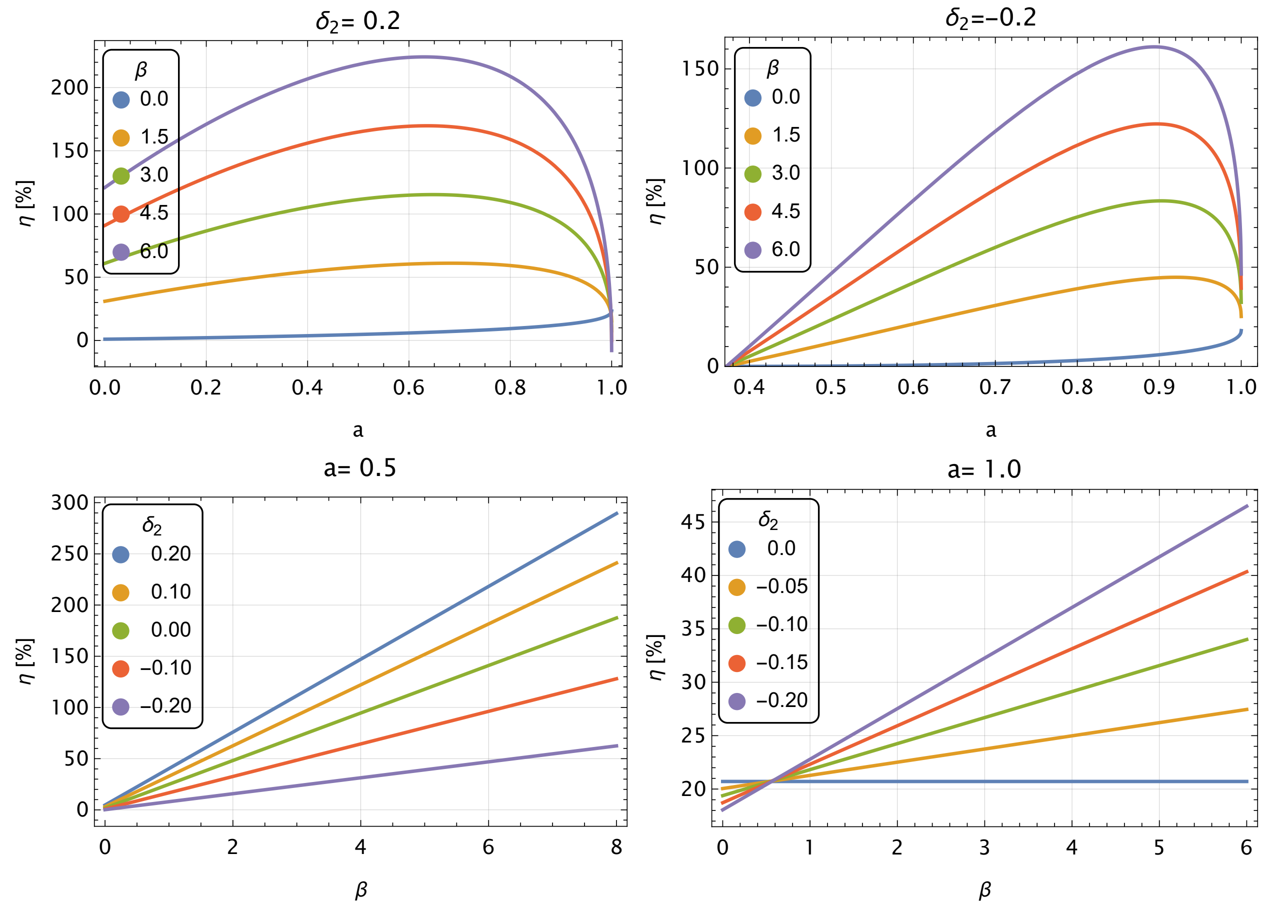

Figure 3.3: The efficiency of energy extraction from the parameterized KRZ BH using the MPP. Top row: η is plotted as a function of the rotation parameter a for positive $\delta_2 = 0.2$ (left) and negative $\delta_2 = -0.2$ (right) in the equatorial plane (i.e., $\theta = \pi/2$) of the BH. Bottom row: η is plotted as a function of the magnetic field parameter β for various possible combinations of δ_2 for fixed $a = 0.5$ (left) and the extremal value, $a = 1$ (right).

infinity, while the other is pulled into the event horizon. After this process, the escaping particle can have more energy than the initial particle. Therefore, it has been well considered energy extraction from the BH.

Using the assumptions given in Section 2.2 and Eq. (2.11), the efficiency of energy extraction form the parameterized KRZ BH via the MPP can be defined as follows

$$\eta = \frac{1}{2}\left(\sqrt{\frac{(2a+r_0^2\delta_2)^2}{r_0^4+a^2r_0(r_0+2)+ar_0^3\delta_2}+1}-1\right)+ \\ +\beta\frac{(2a+r_0^2\delta_2)[r_0^3+a^2(r_0-2)-ar_0^2\delta_2]}{2(r_0^4+a^2r_0(r_0+2)+ar_0^3\delta_2)} \tag{3.17}$$

where we have defined $\beta = q_3B/E_1 \sim qB/m$ as the magnetic parameter highlighting the impact of the MPP on the efficiency of energy extraction and $r_0 = 1+\sqrt{1-a^2}$ as the horizon radius of the parameterized KRZ BH.

We now turn to analyze the efficiency of energy extraction from the parameterized KRZ BH. In Fig. 3.3, we show the efficiency of energy extraction from the BH as a function of the spin parameter a in the top row, and the magnetic field parameter β in the bottom row. It is observed from the top row of Fig. 3.3 that the shape of the efficiency of energy extraction shifts upward toward larger values as the magnetic field parameter β increases. Therefore, the efficiency is strongly enhanced due to the influence of the magnetic field parameter, resulting in it exceeding 100%. This enhancement occurs due to the MPP and allows for arbitrarily large energy efficiency. Additionally, the point to note is that the efficiency of energy extraction with positive $\delta_2 > 0$ takes larger values than with negative $\delta_2 < 0$. Notably, it can be observed from the top left panel of Fig. 3.3 that the energy efficiency reaches $\eta \sim 23.3\%$, which is greater than the Kerr case (where it is $\eta \sim 20.7\%$) when $a \to a_{ext}$. This occurs because the MPP part goes to $\eta|_{q\neq 0} = 0$ when $a \to a_{ext}$. However, the negative values of the deformation parameter δ_2 allow the MPP part to retain its contribution even when $a \to a_{ext}$, as shown in the right column of Fig. 3.3. This is a remarkable and distinguishing nature of these positive and negative values of the deformation parameter δ_2. In the bottom row of Fig. 3.3, we demonstrate the impact of the deformation parameter δ_2 on the efficiency of energy extraction from the BH via the MPP. It is evident from the left panel of Fig. 3.3 that the curves of the efficiency of energy extraction shift upward toward larger values and surpass $\eta > 100\%$ as we increase the deformation parameter δ_2 from negative to positive values. One can also notice that the efficiency becomes larger than the Kerr case for positive values of δ_2, but less for its negative values, as depicted in the bottom left panel of Fig. 3.3. As highlighted earlier, the efficiency of energy extraction increases with the rise in the negative value of δ even in the case of $a \to a_{ext}$; see the bottom right panel of Fig. 3.3. This is one of the unique aspects of the deformation parameter δ_2.

3.5 Astrophysical applications of the magnetic Penrose process

In this section, we consider astrophysical applications of the MPP. To this end, we estimate the maximum energy of a proton escaping from the ergoregion of the parameterized KRZ BH. Unlike the previous analysis of the efficiency of energy extraction, we determine the energy after the proton gets accelerated by the magnetic field in the ergoregion of the parameterized KRZ BH. This results in the MPP being considered for possible applications of the results presented in the previous section. To provide a more appropriate and quantitative analysis, we need to examine the neutron beta-decay process in the close vicinity of the parameterized KRZ BH [145–147]:

$$n^0 \to p^+ + W^- \to p^+ + e^- + \overline{\nu}_e \,. \tag{3.18}$$

We now turn to determine the energy of accelerating protons. From Eqs. (2.10) and (3.17), we obtain the analytical form of the energy for the accelerating protons:

$$E_{p^+} = \frac{1}{2}\left(\sqrt{\frac{(2a+r_0^2\delta_2)^2}{r_0^4+a^2r_0(r_0+2)+ar_0^3\delta_2}+1}-1\right)m_{n^0}c^2+ \\ + eB\frac{(2a+r_0^2\delta_2)[r_0^3+a^2(r_0-2)-ar_0^2\delta_2]}{2(r_0^4+a^2r_0(r_0+2)+ar_0^3\delta_2)}\,, \tag{3.19}$$

where m_{n^0} refers to the mass of falling neutron. Using Eq. (3.19), the energy of the escaping proton after the beta-decay of a free neutron can be determined by the following expression:

$$E_{p^+} = 1.57\times10^{20}\text{eV}\left(\frac{B}{10^4\text{G}}\right)\left(\frac{M}{10^9M_\odot}\right)\left(\frac{a}{0.5}\right)\,, \tag{3.20}$$

where we have set the rotational deformation parameter $\delta_2 = 0.2$ of the parameterized metric considered here. To be more quantitative, we estimate this energy of escaping protons. We show that it can be estimated to be E_{p^+} reaches the value $10^{20}eV$ for given the mass $M\sim10^9M_\odot$ and magnetic field strength $B\sim10^4$G provided that the beta decay occurs around the BH, especially very close to the BH's event horizon, i.e., $r_{\rm decay}\approx r_0$. This value of energy corresponds to the ultra-high-energy cosmic rays.

We now turn to estimate the accelerating power of the supermassive BH at the center of SgrA* with a mass of $4\times10^6M_\odot$ (see, for example, In Ref. [177]) and the magnetic field of nearly 1 to 200G at the event horizon scales (see, for example, in Refs. [86, 87, 118, 148]). After beta decay the maximum energy of protons accelerated by SgrA* as the parameterized KRZ BH can be estimated as follows:

$$E_{p^+}^{\text{Sgr }A^\star} = 6.27\times10^{15}\text{eV}\left(\frac{B}{10^2\text{G}}\right)\times\left(\frac{M}{4\times10^6M_\odot}\right)\left(\frac{a}{0.5}\right)\,, \tag{3.21}$$

referred to as the knee of the cosmic ray energy spectrum. The knee energy is located around energies of 10^{15}—10^{16} eV. After this point, the flux of cosmic rays

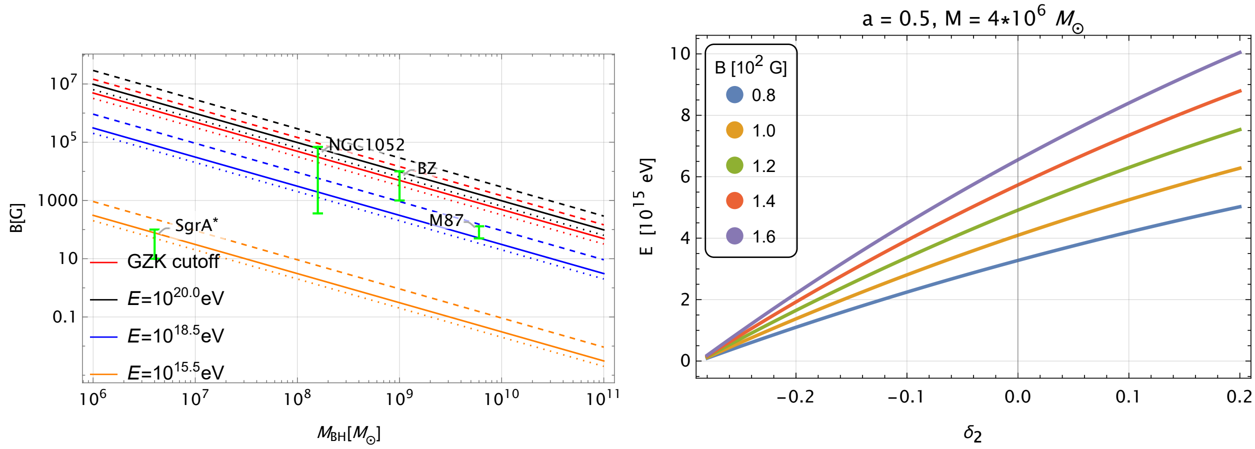

Figure 3.4: The left panel shows constraint plot of the BH mass and magnetic field for some selected BH candidates serving as sources of high-energy protons with different energies for various possible cases of the rotational deformation parameter δ_2. Solid lines correspond to $\delta_2 = 0.0$, dotted to $\delta_2 = 0.2$, and dashed to $\delta_2 = -0.2$. The right panel shows the energy of accelerated protons by SgrA* after beta decay as a function of δ_2 for various possible values of the magnetic field strength B.

suddenly decreases. It is evident from the above estimated value that the knee energy for the parameterized KRZ BH is larger than the one for the Kerr BH case [146].

We now provide a more appropriate and detailed analysis associated with constraints on the BH mass and the strength of the magnetic field existing in the surrounding environment of BHs serving as sources of highly energetic astrophysical phenomena, such as high-energy protons with various energies. In Fig. 3.4, we show how the combined effects of the magnetic field and BH mass contribute to the energy of escaping protons which can likely be considered ultra-high-energy cosmic rays. As can be seen from Fig. 3.4, the vertical green lines manifest the range of possible magnetic field strength as stated by the observational data for BH candidates. For example, measurements of magnetic fields have been conducted with precise and various confidential methods for some selected sources (see details, e.g., in Refs. [118, 148, 178, 179]). Additionally, EHT collaborations have reported very recently that the magnetic field strength is of the order of $B \sim 1-30$ G in the emission region, according to observations at 230 GHz around the supermassive BH at the center of the M87 galaxy [86, 87]. Based on these observational data for the selected sources, we utilize the range of possible magnetic field strength in our analysis, as seen in Fig. 3.4. We also note that solid black, blue and orange lines depict specific energies of the escaping particles in the limit of $\delta_2 = 0$, thus manifesting the acceleration capability of a Kerr BH. Unlike solid lines, the dashed and dotted lines depict the effect of the deformation parameter δ_2 on the acceleration capability of the parameterized KRZ BH. Interestingly, we find that for the proton to get accelerated with the same energy under the acceleration capability of the parameterized KRZ BH, it is required for a BH to have more mass and a stronger magnetic field for the negative case of the deformation parameter $\delta_2 < 0$. However, the opposite is true for the positive values of the deformation parameter $\delta_2 > 0$. The point to be noted here is that we also show the red lines to describe the Greisen-Zatsepin-Kuzmin (GZK) limit, usually referred to as cutoff effect, for various possible values of the parameter δ_2. The GZK cutoff limit delineates the maximum energy protons can have when travelling from other galaxies through the intergalactic medium to our SgrA* galaxy. This limit can be estimated theoretically to be nearly $5\times10^{19}\, eV$ [149]. The reason for the existence of this limit is due to interactions between the protons and the microwave background radiation over vast distances. In addition, in the right panel of Fig. 3.4, we demonstrate the energy of accelerated protons as a function of the deformation parameter δ_2 for various possible combinations of the magnetic field strength B. From the right panel of Fig. 3.4, the energy of accelerated protons rises as δ_2 increases for given BH parameters. It can be observed from the right panel that the curves of energy shift upward toward larger values as a consequence of the rise in the value of the magnetic field strength. One can infer from the results that the energy of accelerated protons in the ergoregion of the parameterized KRZ BH is more sensitive to the background magnetic field B and the rotational deformation parameter δ_2 as well.

3.6 Conclusion

In this chapter, we examined the parameterized KRZ black hole (BH) spacetime within an external asymptotically uniform magnetic field. By applying the MPP, we demonstrated how the deformation parameter, δ, affect the efficiency of energy extraction from the BH. Our findings provide new insights into the MPP, enhancing our understanding of high-energy phenomena near parameterized KRZ BHs and the fundamental mechanisms driving these events. This study not only advances theoretical knowledge but also lays the groundwork for future observational and experimental research, aiming to explore the extreme environments around BHs more comprehensively.

We began by deriving the field equations and found the electromagnetic four-vector potentials for the case of the parameterized KRZ BH. We then investigated the motion of charged test particles around the BH immersed in an external uniform magnetic field. We showed that the stable orbits are shifted to the left to smaller r due to the rise in the value of the deformation parameters $\delta_{1,2}$. We also showed that the deformation parameters $\delta_{1,2}$ strengthen the potential barrier. Additionally, we found that charged particles are not able to escape from the pull of gravity but instead to be trapped under the combined effects of gravitational and electromagnetic forces around the BH.

From an astrophysical point of view, astrophysical rotating BHs are considered the high-energy sources in the universe. Therefore, testing BH's energetic properties is valuable through the various methods for understanding of their rotational energy. We also considered the MPP to study the efficiency of energy extraction from the parameterized KRZ BH. We showed the efficiency of energy extraction is strongly enhanced by the MPP. This results in the energy efficiency to surpass 100%. This enhancement permits for arbitrarily large energy efficiency due to the MPP. Additionally, we observed that the efficiency of energy extraction with positive $\delta_2 > 0$ is larger than negative $\delta_2 < 0$. Interestingly, it was found that the energy efficiency approaches $\eta \sim 23.3\%$, which is greater than the Kerr case, as the MPP part goes to $\eta|_{q\neq 0} = 0$ when $a \to a_{ext}$. It is worth noting, however, that the negative values of the deformation parameter δ_2 allow the MPP part to retain its contribution regardless of the extremal value a_{ext} of the rotation parameter. This is a remarkable and distinguishing feature of these positive and negative values of the deformation parameter δ_2. Furthermore, it is observed that the efficiency of energy extraction surpasses $\eta > 100\%$ as the deformation parameter δ_2 increases from its negative to positive values. Notably, we showed that the efficiency is larger than the Kerr case for $\delta_2 > 0$, but less for $\delta_2 < 0$. It must be noted that for the negative values of δ the MPP part does not go to zero even when $a \to a_{ext}$, thereby increasing the energy efficiency, i.e.., $\eta(\delta_2 \neq 0)|_{a\to a_{ext}} > \eta(\delta_2 = 0)|_{a\to a_{ext}}$. This is one of the unique aspects of δ_2 in the parameterized KRZ BH spacetime.

We also provided a more appropriate and detailed analysis associated with constraints on the BH mass and the strength of the magnetic field around selected BHs serving as sources of high-energy protons with various energies. We showed the combined effects of the magnetic field and BH mass on the energy of escaping protons considered as ultra-high-energy cosmic rays. Based on the observational data for some selected sources, we used the range of possible magnetic field strengths in our analysis. We demonstrated deviations from the acceleration capability of a

Kerr BH due to the deformation parameter δ_2 of the parameterized KRZ BH. Interestingly, we found that more mass and a stronger magnetic field are required for the proton to be accelerated to the same energy under the acceleration capability of the parameterized KRZ BH for the case of a negative deformation parameter $\delta_2 < 0$. However, the opposite is true for the case of a positive $\delta_2 > 0$. We also analyzed the GZK cutoff energy limit and showed the influence of the deformation parameter δ_2. Notably, the GZK cutoff limit can also be affected in a similar way in the parameterized KRZ BH spacetime. Furthermore, we studied how the energy of accelerated protons can be influenced under the combined effects of the deformation parameter δ_2 and the magnetic field B. We showed that the energy of accelerated protons increases with an increase in the deformation parameter δ_2 and the magnetic field strength B. The results suggest that the energy of accelerated protons is more sensitive to the background magnetic field B and the rotational deformation parameter δ_2 of the parameterized KRZ BH spacetime.

Astrophysically, it is often difficult for distant observers to differentiate between various BH geometries due to the similar radiation emitted by accretion disks in low-mass X-ray binaries. This similarity is a result of the inherent degeneracy in BH spacetimes. Based on these theoretical studies, the approach we utilized here is vital for uncovering the distinct and novel characteristics of the parameterized KRZ BH spacetime, providing deeper insights into its unique properties.

Main results and conclusions

The main results of the dissertation are presented below:

1. For the first time, the quantum correction parameter ξ of QCBH has been constrained as $\xi \leq 0.01869$ from Solar System tests, $\xi \leq 0.73528$ from the orbit of the S2 star around Sgr A*, and $\xi \leq 2.086$ from QPO observations of X-ray binaries.

2. For the first time, the efficiency of the Magnetic Penrose Process has been found to be 19.3% for loop quantum black hole (20.7% in the Kerr case) for $a = a_{\text{extremal}}$. It has been found that the efficiency of the MPP can also exceed 100% for the LQBH, similarly to the observed Kerr BH case.

3. For the first time, it has been shown that for the quantum correction parameter ϵ of the LQBH, $\epsilon = 0.2$, the energy of an escaping proton from M87 can reach $E_p^{\text{M87}} = 1.89 \times 10^{18}$ eV, corresponding to the ankle region of the cosmic-ray spectrum (10^{18}–10^{19} eV).

4. For the first time, it has been found that the energy efficiency of the Magnetic Penrose Process for the KRZ black hole approaches $\eta \sim 23.3\%$, which is greater than in the Kerr case.

5. For the first time, it has been shown that for the deformation parameter of the KRZ black hole, $\delta_2 = 0.2$, the energy of an escaping proton from SgrA*

can reach $E_p^{\mathrm{SgrA}^*} = 6.27 \times 10^{15}$ eV, corresponding to the knee region of the cosmic-ray spectrum (10^{15}–10^{16} eV).

Bibliography

[1] T. Xamidov, S. Shaymatov, P. Sheoran, and B. Ahmedov, “Astrophysical insights into magnetic Penrose process around parameterized Konoplya–Rezzolla–Zhidenko black hole,” *Eur. Phys. J. C*, vol. 84, no. 12, p. 1300, Dec. 2024.

[2] T. Xamidov, U. Uktamov, S. Shaymatov, and B. Ahmedov, “Quasiperiodic oscillations around a Schwarzschild black hole surrounded by a Dehnen type dark matter halo,” *Phys. Dark Universe*, vol. 47, p. 101805, Feb. 2025.

[3] T. Xamidov, M. Alloqulov, and S. Shaymatov, “Electric Penrose process and collisions of particles near five-dimensional weakly charged Schwarzschild black hole,” *European Physical Journal Plus*, vol. 140, no. 3, p. 182, Mar. 2025.

[4] T. Xamidov, P. Sheoran, S. Shaymatov, and T. Zhu, “Energy extraction from Loop Quantum Black Holes: the role of magnetic Penrose process and quantum gravity effects with astrophysical insights,” *J. Cosmol. Astropart. Phys.*, vol. 2025, no. 3, p. 053, Mar. 2025.

[5] T. Xamidov, S. Shaymatov, Q. Wu, and T. Zhu, “Probing the Schwarzschild black hole immersed in a dark matter halo through astrophysical tests,” *European Physical Journal C*, vol. 85, p. 1193, Oct. 2025.

[6] A. Einstein, “Die Grundlage der allgemeinen Relativitätstheorie,” *Annalen der Physik*, vol. 354, no. 7, pp. 769–822, Jan. 1916.

[7] B. P. Abbott and et al. (Virgo and LIGO Scientific Collaborations), “Observation of Gravitational Waves from a Binary Black Hole Merger,” *Phys. Rev. Lett.*, vol. 116, no. 6, p. 061102, Feb. 2016.

[8] B. P. Abbott and et al. (Virgo and LIGO Scientific Collaborations), “Properties of the Binary Black Hole Merger GW150914,” *Phys. Rev. Lett.*, vol. 116, no. 24, p. 241102, Jun. 2016.

[9] K. Akiyama and et al. (Event Horizon Telescope Collaboration), “First M87 Event Horizon Telescope Results. I. The Shadow of the Supermassive Black Hole,” *Astrophys. J.*, vol. 875, no. 1, p. L1, Apr 2019.

[10] K. Akiyama and et al. (Event Horizon Telescope Collaboration), “First M87 Event Horizon Telescope Results. VI. The Shadow and Mass of the Central Black Hole,” *Astrophys. J.*, vol. 875, no. 1, p. L6, Apr 2019.

[11] K. Akiyama and et al. (Event Horizon Telescope Collaboration), “First Sagittarius A* Event Horizon Telescope Results. I. The Shadow of the Supermassive Black Hole in the Center of the Milky Way,” *Astrophys. J. Lett.*, vol. 930, no. 2, p. L12, May 2022.

[12] K. Akiyama and et al. (Event Horizon Telescope Collaboration), “First Sagittarius A* Event Horizon Telescope Results. III. Imaging of the Galactic Center Supermassive Black Hole,” *Astrophys. J. Lett.*, vol. 930, no. 2, p. L14, May 2022.

[13] A. Ashtekar and E. Bianchi, “A short review of loop quantum gravity,” *Rept. Prog. Phys.*, vol. 84, no. 4, p. 042001, 2021.

[14] R. Penrose, “Gravitational Collapse and Space-Time Singularities,” *Phys. Rev. Lett.*, vol. 14, no. 3, pp. 57–59, Jan. 1965.

[15] S. W. Hawking and R. Penrose, “The Singularities of Gravitational Collapse and Cosmology,” *Proc R. Soc. Lond. A*, vol. 314, pp. 529–548, Jan. 1970.

[16] A. Ashtekar and J. Lewandowski, “Background independent quantum gravity: A Status report,” *Class. Quant. Grav.*, vol. 21, p. R53, 2004.

[17] T. Thiemann, *Modern Canonical Quantum General Relativity*, 2007.

[18] C. Zhang, J. Lewandowski, Y. Ma, and J. Yang, “Black Holes and Covariance in Effective Quantum Gravity,” *arXiv e-prints*, p. arXiv:2407.10168, Jul. 2024.

[19] R. Gambini and J. Pullin, “Black holes in loop quantum gravity: The Complete space-time,” *Phys. Rev. Lett.*, vol. 101, p. 161301, 2008.

[20] A. Perez, “Black Holes in Loop Quantum Gravity,” *Rept. Prog. Phys.*, vol. 80, no. 12, p. 126901, 2017.

[21] R. Gambini, J. Olmedo, and J. Pullin, “Quantum black holes in Loop Quantum Gravity,” *Class. Quant. Grav.*, vol. 31, p. 095009, 2014.

[22] P. G. S. Fernandes, “Charged black holes in AdS spaces in 4D Einstein Gauss-Bonnet gravity,” *Phys. Lett. B*, vol. 805, p. 135468, 2020.

[23] H.-W. Hu, C. Lan, and Y.-G. Miao, “A regular black hole as the final state of evolution of a singular black hole,” *Eur. Phys. J. C*, vol. 83, no. 11, p. 1047, 2023.

[24] C. Lan, H. Yang, Y. Guo, and Y.-G. Miao, “Regular Black Holes: A Short Topic Review,” *Int. J. Theor. Phys.*, vol. 62, no. 9, p. 202, 2023.

[25] L. Modesto, "Semiclassical loop quantum black hole," *Int. J. Theor. Phys.*, vol. 49, pp. 1649–1683, 2010.

[26] L. Modesto and I. Premont-Schwarz, "Self-dual Black Holes in LQG: Theory and Phenomenology," *Phys. Rev. D*, vol. 80, p. 064041, 2009.

[27] S. Sahu, K. Lochan, and D. Narasimha, "Gravitational lensing by self-dual black holes in loop quantum gravity," *Phys. Rev. D*, vol. 91, p. 063001, 2015.

[28] R. Konoplya, L. Rezzolla, and A. Zhidenko, "General parametrization of axisymmetric black holes in metric theories of gravity," *Phys. Rev. D*, vol. 93, no. 6, 2016.

[29] Y. Ni, J. Jiang, and C. Bambi, "Testing the kerr metric with the iron line and the krz parametrization," *Journal of Cosmology and Astroparticle Physics*, vol. 2016, no. 09, 2016.

[30] C. Liu, T. Zhu, Q. Wu, K. Jusufi, M. Jamil, M. Azreg-Aïnou, and A. Wang, "Shadow and quasinormal modes of a rotating loop quantum black hole," *Phys. Rev. D*, vol. 101, no. 8, p. 084001, 2020, [Erratum: Phys.Rev.D 103, 089902 (2021)].

[31] U. Uktamov, M. Alloqulov, S. Shaymatov, T. Zhu, and B. Ahmedov, "Particle dynamics and the accretion disk around a Self-dual Black Hole immersed in a magnetic field in Loop Quantum Gravity," *Phys. Dark Univ.*, vol. 47, p. 101743, 2025.

[32] T. Zhu and A. Wang, "Observational tests of the self-dual spacetime in loop quantum gravity," *Phys. Rev. D*, vol. 102, p. 124042, 2020.

[33] Z.-Y. Tu, T. Zhu, and A. Wang, "Periodic orbits and their gravitational wave radiations in a polymer black hole in loop quantum gravity," *Phys. Rev. D*, vol. 108, no. 2, p. 024035, 2023.

[34] C. Liu, H. Siew, T. Zhu, Q. Wu, Y. Sun, Y. Zhao, and H. Xu, "Constraints on the rotating self-dual black hole with quasi-periodic oscillations," *JCAP*, vol. 11, p. 096, 2023.

[35] H.-X. Jiang, C. Liu, I. K. Dihingia, Y. Mizuno, H. Xu, T. Zhu, and Q. Wu, "Shadows of loop quantum black holes: semi-analytical simulations of loop quantum gravity effects on Sagittarius A* and M87*," *JCAP*, vol. 01, p. 059, 2024.

[36] H.-X. Jiang, I. K. Dihingia, C. Liu, Y. Mizuno, and T. Zhu, "Enhanced Blandford Znajek jet in loop quantum black hole," *JCAP*, vol. 05, p. 101, 2024.

[37] H. Jiang, M. Alloqulov, Q. Wu, S. Shaymatov, and T. Zhu, "Periodic orbits and plasma effects on gravitational weak lensing by self-dual black hole in loop quantum gravity," *Phys. Dark Univ.*, vol. 46, p. 101627, 2024.

[38] J.-M. Yan, Q. Wu, C. Liu, T. Zhu, and A. Wang, "Constraints on self-dual black hole in loop quantum gravity with S0-2 star in the galactic center," *JCAP*, vol. 09, p. 008, 2022.

[39] J.-M. Yan, C. Liu, T. Zhu, Q. Wu, and A. Wang, "Observational tests of a quantum extension of Schwarzschild spacetime in loop quantum gravity with stars in the Galactic Center," *Phys. Rev. D*, vol. 107, no. 8, p. 084043, 2023.

[40] M. Momennia, “Quasinormal modes of self-dual black holes in loop quantum gravity,” *Phys. Rev. D*, vol. 106, no. 2, p. 024052, 2022.

[41] M. A. Abramowicz and P. C. Fragile, “Foundations of Black Hole Accretion Disk Theory,” *Living Rev. Relativ.*, vol. 16, no. 1, p. 1, Jan. 2013.

[42] C. Bambi, “Testing the Kerr nature of stellar-mass black hole candidates by combining the continuum-fitting method and the power estimate of transient ballistic jets,” *Phys. Rev. D*, vol. 85, no. 4, p. 043002, Feb 2012.

[43] C. Bambi, J. Jiang, and J. F. Steiner, “Testing the no-hair theorem with the continuum-fitting and the iron line methods: a short review,” *Classical and Quantum Gravity*, vol. 33, no. 6, p. 064001, Mar. 2016.

[44] A. Tripathi, J. Yan, Y. Yang, Y. Yan, M. Garnham, Y. Yao, S. Li, Z. Ding, A. B. Abdikamalov, D. Ayzenberg, C. Bambi, T. Dauser, J. A. Garcia, J. Jiang, and S. Nampalliwar, “Constraints on the spacetime metric around seven “bare” AGN using X-ray reflection spectroscopy,” *arXiv e-prints*, Jan. 2019.

[45] R. A. Konoplya and O. S. Stashko, “Probing the Effective Quantum Gravity via Quasinormal Modes and Shadows of Black Holes,” *arXiv e-prints*, p. arXiv:2408.02578, Aug. 2024.

[46] Y.-H. Shu and J.-H. Huang, “Circular orbits and thin accretion disk around a quantum corrected black hole,” *arXiv e-prints*, p. arXiv:2412.05670, Dec. 2024.

[47] M. Skvortsova, “Quantum corrected black holes: testing the correspondence between grey-body factors and quasinormal modes,” *arXiv e-prints*, p. arXiv:2411.06007, Nov. 2024.

[48] W. Liu, D. Wu, and J. Wang, “Light rings and shadows of static black holes in effective quantum gravity,” *Phys. Lett. B*, vol. 858, p. 139052, 2024.

[49] H. Liu, M.-Y. Lai, X.-Y. Pan, H. Huang, and D.-C. Zou, “Gravitational lensing effect of black holes in effective quantum gravity,” *Phys. Rev. D*, vol. 110, no. 10, p. 104039, 2024.

[50] Y.-H. Shu and J.-H. Huang, “Circular orbits and thin accretion disk around a quantum corrected black hole,” 12 2024.

[51] H. Jiang, M. Alloqulov, Q. Wu, S. Shaymatov, and T. Zhu, “Periodic orbits and plasma effects on gravitational weak lensing by self-dual black hole in loop quantum gravity,” *Phys. Dark Universe*, vol. 46, p. 101627, Dec. 2024.

[52] Y. Du, Y. Liu, and X. Zhang, “Spinning Particle Dynamics and ISCO in Covariant Loop Quantum Gravity,” 11 2024.

[53] Z. Ban, J. Chen, and J. Yang, “Shadows of rotating black holes in effective quantum gravity,” 11 2024.

[54] Y. Wang, A. Vachher, Q. Wu, T. Zhu, and S. G. Ghosh, “Strong Gravitational Lensing by Static Black Holes in Effective Quantum Gravity,” 10 2024.

[55] U. Uktamov, M. Alloqulov, S. Shaymatov, T. Zhu, and B. Ahmedov, “Particle dynamics and the accretion disk around a Self-dual Black Hole immersed in a magnetic field in Loop Quantum Gravity,” *Phys. Dark Universe*, vol. 47, p. 101743, Feb. 2025.

[56] A. Ashtekar, T. Pawlowski, and P. Singh, “Quantum nature of the big bang: Improved dynamics,” *Phys. Rev. D*, vol. 74, no. 8, p. 084003, Oct. 2006.

[57] M. Domagala and J. Lewandowski, "Black-hole entropy from quantum geometry," *Classical and Quantum Gravity*, vol. 21, no. 22, pp. 5233–5243, Nov. 2004.

[58] K. A. Meissner, "Black-hole entropy in loop quantum gravity," *Classical and Quantum Gravity*, vol. 21, no. 22, pp. 5245–5251, Nov. 2004.

[59] C. W. Misner, K. S. Thorne, and J. A. Wheeler, *Gravitation.* San Francisco: W. H. Freeman, 1973.

[60] S. Shaymatov, P. Sheoran, and S. Siwach, "Motion of charged and spinning particles influenced by dark matter field surrounding a charged dyonic black hole," *Phys. Rev. D*, vol. 105, no. 10, p. 104059, May 2022.

[61] S. Shaymatov, K. Jusufi, M. Alloqulov, and B. Ahmedov, "Epicyclic motions and constraints on the charged stringy black hole spacetime," *Eur. Phys. J. Plus*, vol. 138, no. 11, p. 997, Nov. 2023.

[62] G. S. Adkins and J. McDonnell, "Orbital precession due to central-force perturbations," *Phys. Rev. D*, vol. 75, no. 8, p. 082001, Apr. 2007.

[63] S. Benczik, L. N. Chang, D. Minic, N. Okamura, S. Rayyan, and T. Takeuchi, "Short distance versus long distance physics: The classical limit of the minimal length uncertainty relation," *Phys. Rev. D*, vol. 66, no. 2, p. 026003, Jun. 2002.

[64] L. Iorio, "Gravitational anomalies in the solar system?" *Int. J. Mod. Phys. D*, vol. 24, no. 6, pp. 1 530 015–343, Feb. 2015.

[65] L. Iorio, "Calculation of the Uncertainties in the Planetary Precessions with the Recent EPM2017 Ephemerides and their Use in Fundamental Physics and Beyond," *Astrophys. J.*, vol. 157, no. 6, p. 220, Jun. 2019.

[66] S. Shaymatov, B. Ahmedov, M. De Laurentis, M. Jamil, Q. Wu, A. Wang, and M. Azreg-Aïnou, "On the Parameters of the Spherically Symmetric Parameterized Rezzolla-Zhidenko Spacetime through Solar System Tests, the Orbit of the S2 Star about Sgr A*, and Quasiperiodic Oscillations," *Astrophys. J.*, vol. 959, no. 1, p. 6, Dec. 2023.

[67] GRAVITY Collaboration, "Detection of the Schwarzschild precession in the orbit of the star S2 near the Galactic centre massive black hole," *Astron. Astrophys.*, vol. 636, p. L5, Apr. 2020.

[68] S. Shaymatov, J. Vrba, D. Malafarina, B. Ahmedov, and Z. Stuchlík, "Charged particle and epicyclic motions around 4 D Einstein-Gauss-Bonnet black hole immersed in an external magnetic field," *Phys. Dark Universe*, vol. 30, p. 100648, Dec. 2020.

[69] Z. Stuchlík and J. Vrba, "Epicyclic orbits in the field of Einstein-Dirac-Maxwell traversable wormholes applied to the quasiperiodic oscillations observed in microquasars and active galactic nuclei," *Eur. Phys. J. Plus*, vol. 136, no. 11, p. 1127, Nov. 2021.

[70] E. Deligianni, B. Kleihaus, J. Kunz, P. Nedkova, and S. Yazadjiev, "Quasiperiodic oscillations in rotating ellis wormhole spacetimes," *Phys. Rev. D*, vol. 104, p. 064043, Sep 2021. [Online]. Available: https://link.aps.org/doi/10.1103/PhysRevD.104.064043

[71] I. Banerjee, "Testing black holes in non-linear electrodynamics from the observed quasi-periodic oscillations," *Journal of Cosmology and Astroparticle Physics*, vol. 2022, no. 08, p. 034, aug 2022. [Online]. Available: https://dx.doi.org/10.1088/1475-7516/2022/08/034

[72] R. A. Remillard and J. E. McClintock, “X-Ray Properties of Black-Hole Binaries,” *Annu. Rev. Astron. Astrophys.*, vol. 44, no. 1, pp. 49–92, Sep. 2006.

[73] A. A. Molla, S. K. Chakrabarti, D. Debnath, and S. Mondal, “Estimation of Mass of Compact Object in H 1743-322 from 2010 and 2011 Outbursts using TCAF Solution and Spectral Index-QPO Frequency Correlation,” *Astrophys. J.*, vol. 834, no. 1, p. 88, Jan. 2017.

[74] A. Ingram and S. Motta, “Solutions to the relativistic precession model,” *Mon. Not. R. Astron. Soc.*, vol. 444, no. 3, pp. 2065–2070, Nov. 2014.

[75] R. A. Remillard, M. P. Muno, J. E. McClintock, and J. A. Orosz, “Evidence for Harmonic Relationships in the High-Frequency Quasi-periodic Oscillations of XTE J1550-564 and GRO J1655-40,” *Astrophys. J.*, vol. 580, no. 2, pp. 1030–1042, Dec. 2002.

[76] J. A. Orosz, J. F. Steiner, J. E. McClintock, M. A. P. Torres, R. A. Remillard, C. D. Bailyn, and J. M. Miller, “An Improved Dynamical Model for the Microquasar XTE J1550-564,” *Astrophys. J.*, vol. 730, no. 2, p. 75, Apr. 2011.

[77] S. E. Motta, T. M. Belloni, L. Stella, T. Muñoz-Darias, and R. Fender, “Precise mass and spin measurements for a stellar-mass black hole through X-ray timing: the case of GRO J1655-40,” *Mon. Not. R. Astron. Soc.*, vol. 437, no. 3, pp. 2554–2565, Jan. 2014.

[78] D. Foreman-Mackey, D. W. Hogg, D. Lang, and J. Goodman, “emcee: The MCMC Hammer,” *Publ. Astron. Soc. Pac.*, vol. 125, no. 925, p. 306, Mar. 2013.

[79] A. Ashtekar and M. Bojowald, "Quantum geometry and the Schwarzschild singularity," *Class. Quant. Grav.*, vol. 23, pp. 391–411, 2006.

[80] L. Modesto, "Semiclassical Loop Quantum Black Hole," *Int. J. Theor. Phys.*, vol. 49, no. 8, pp. 1649–1683, Aug. 2010.

[81] R. D. Blandford and R. L. Znajek, "Electromagnetic extraction of energy from Kerr black holes," *Mon. Not. Roy. Astron. Soc.*, vol. 179, pp. 433–456, May 1977.

[82] T. Damour, R. S. Hanni, R. Ruffini, and J. R. Wilson, "Regions of magnetic support of a plasma around a black hole," *Phys. Rev. D*, vol. 17, pp. 1518–1523, Mar 1978. [Online]. Available: https://link.aps.org/doi/10.1103/PhysRevD.17.1518

[83] M. Y. Piotrovich, N. A. Silant'ev, Y. N. Gnedin, and T. M. Natsvlishvili, "Magnetic Fields of Black Holes and the Variability Plane," *ArXiv e-prints*, Feb. 2010.

[84] A.-K. Baczko, R. Schulz, and et al., "A highly magnetized twin-jet base pinpoints a supermassive black hole," *Astron. Astrophys.*, vol. 593, p. A47, Sep. 2016.

[85] R. A. Daly, "Black Hole Spin and Accretion Disk Magnetic Field Strength Estimates for More Than 750 Active Galactic Nuclei and Multiple Galactic Black Holes," *Astrophys. J.*, vol. 886, no. 1, p. 37, Nov. 2019.

[86] Event Horizon Telescope Collaboration, "First M87 Event Horizon Telescope Results. VIII. Magnetic Field Structure near The Event Horizon," *Astrophys. J. Lett.*, vol. 910, no. 1, p. L13, Mar. 2021.

[87] R. Narayan, D. C. M. Palumbo, M. D. Johnson, and et al., "The Polarized Image of a Synchrotron-emitting Ring of Gas Orbiting a Black Hole," *Astrophys. J.*, vol. 912, no. 1, p. 35, May 2021.

[88] A. N. Aliev and N. Özdemir, "Motion of charged particles around a rotating black hole in a magnetic field," *Mon. Not. R. Astron. Soc.*, vol. 336, pp. 241–248, Oct. 2002.

[89] V. P. Frolov and A. A. Shoom, "Motion of charged particles near a weakly magnetized Schwarzschild black hole," *Phys. Rev. D*, vol. 82, no. 8, p. 084034, Oct. 2010.

[90] A. Tursunov, Z. Stuchlík, and M. Kološ, "Circular orbits and related quasi-harmonic oscillatory motion of charged particles around weakly magnetized rotating black holes," *Phys. Rev. D*, vol. 93, no. 8, p. 084012, Apr. 2016.

[91] S. Shaymatov, D. Malafarina, and B. Ahmedov, "Effect of perfect fluid dark matter on particle motion around a static black hole immersed in an external magnetic field," *Phys. Dark Universe*, vol. 34, p. 100891, Oct. 2021.

[92] S. Shaymatov, B. Narzilloev, A. Abdujabbarov, and C. Bambi, "Charged particle motion around a magnetized Reissner-Nordström black hole," *Phys. Rev. D*, vol. 103, no. 12, p. 124066, Jun. 2021.

[93] Hussain, S, Hussain, I, and Jamil, M., "Dynamics of a charged particle around a slowly rotating kerr black hole immersed in magnetic field," *Eur. Phys. J. C*, vol. 74, no. 3, p. 210, 2014. [Online]. Available: https://doi.org/10.1140/epjc/s10052-014-3210-y

[94] S. Shaymatov, M. Jamil, K. Jusufi, and K. Bamba, "Constraints on the magnetized Ernst black hole spacetime through quasiperiodic oscillations," *Eur. Phys. J. C*, vol. 82, no. 7, p. 636, Jul. 2022.

[95] S. Shaymatov and B. Ahmedov, "Overcharging process around a magnetized black hole: can the backreaction effect of magnetic field restore cosmic censorship conjecture?" *Gen. Relativ. Gravit.*, vol. 55, no. 2, p. 36, Feb. 2023.

[96] S. Shaymatov, B. Ahmedov, Z. Stuchlík, and A. Abdujabbarov, "Effect of an external magnetic field on particle acceleration by a rotating black hole surrounded with quintessential energy," *International Journal of Modern Physics D*, vol. 27, no. 8, p. 1850088, Jan. 2018.

[97] R. M. Wald, "Black hole in a uniform magnetic field," *Phys. Rev. D*, vol. 10, pp. 1680–1685, Sep. 1974.

[98] S. Shaymatov, N. Dadhich, and A. Tursunov, "Energetics of Buchdahl stars and the magnetic Penrose process," *arXiv e-prints*, p. arXiv:2404.06870, Apr. 2024.

[99] S. Parthasarathy, S. M. Wagh, S. V. Dhurandhar, and N. Dadhich, "High Efficiency of the Penrose Process of Energy Extraction from Rotating Black Holes Immersed in Electromagnetic Fields," *Astrophys. J.*, vol. 307, p. 38, Aug 1986. [Online]. Available: https://ui.adsabs.harvard.edu/abs/1986ApJ...307...38P

[100] S. M. Wagh, S. V. Dhurandhar, and N. Dadhich, "Revival of the Penrose Process for Astrophysical Applications," *Astrophys. J.*, vol. 290, p. 12, Mar. 1985.

[101] S. Shaymatov, P. Sheoran, R. Becerril, U. Nucamendi, and B. Ahmedov, "Efficiency of Penrose process in spacetime of axially symmetric magnetized Reissner-Nordström black hole," *Phys. Rev. D*, vol. 106, no. 2, p. 024039, 2022.

[102] R. Penrose, "Gravitational Collapse: the Role of General Relativity," *Riv. Nuovo Cim.*, vol. 1, p. 252, Jan. 1969.

[103] R. Penrose and R. Floyd, "Extraction of rotational energy from a black hole," *Nature Physical Science*, vol. 229, pp. 177–179, 1971.

[104] M. Bhat, S. Dhurandhar, and N. Dadhich, "Energetics of the kerr-newman black hole by the penrose process," *Journal of Astrophysics and Astronomy*, vol. 6, pp. 85–100, 1985.

[105] K. Prabhu and N. Dadhich, "Energetics of a rotating charged black hole in 5-dimensional supergravity," *Phys. Rev. D*, vol. 81, no. 2, p. 024011, Jan. 2010.

[106] A. A. Abdujabbarov, B. J. Ahmedov, S. R. Shaymatov, and A. S. Rakhmatov, "Penrose process in Kerr-Taub-NUT spacetime," *Astrophys Space Sci*, vol. 334, pp. 237–241, Aug. 2011.

[107] M. Nozawa and K.-I. Maeda, "Energy extraction from higher dimensional black holes and black rings," *Phys. Rev. D*, vol. 71, no. 8, p. 084028, Apr. 2005.

[108] S. M. Wagh and N. Dadhich, "The energetics of black holes in electromagnetic fields by the penrose process," *Phys. Rept.*, vol. 183, no. 4, pp. 137–192, 1989.

[109] S. Koide, "Magnetic extraction of black hole rotational energy: Method and results of general relativistic magnetohydrodynamic simulations in Kerr space-time," *Phys. Rev. D*, vol. 67, p. 104010, 2003.

[110] S. Shaymatov, "Efficiency of magnetic Penrose process in higher dimensional Myers-Perry black hole spacetimes," *Phys. Rev. D*, vol. 110, no. 4, p. 044042, Aug. 2024.

[111] S. Shaymatov, N. Dadhich, and A. Tursunov, "Energetics of Buchdahl stars and the magnetic Penrose process," *Eur. Phys. J. C*, vol. 84, no. 10, p. 1015, Oct. 2024.

[112] J. C. McKinney, A. Tchekhovskoy, and R. D. Blandford, "Alignment of Magnetized Accretion Disks and Relativistic Jets with Spinning Black Holes," *Science*, vol. 339, pp. 49–52, 2013.

[113] M. Banados, J. Silk, and S. M. West, "Kerr Black Holes as Particle Accelerators to Arbitrarily High Energy," *Phys. Rev. Lett.*, vol. 103, p. 111102, 2009.

[114] R. Blandford, D. Meier, and A. Readhead, "Relativistic Jets from Active Galactic Nuclei," *Ann. Rev. Astron. Astrophys.*, vol. 57, pp. 467–509, 2019.

[115] E. Battista, "Quantum Schwarzschild geometry in effective field theory models of gravity," *Phys. Rev. D*, vol. 109, no. 2, p. 026004, 2024.

[116] U. P. Suresh, K. R, K. M. Ajith, K. Hegde, S. Punacha, and A. N. Kumara, "Spinning LQG black hole as a particle accelerator," 8 2024.

[117] K. Akiyama *et al.*, "First Sagittarius A* Event Horizon Telescope Results. I. The Shadow of the Supermassive Black Hole in the Center of the Milky Way," *Astrophys. J. Lett.*, vol. 930, no. 2, p. L12, 2022.

[118] R. P. Eatough *et al.*, "A strong magnetic field around the supermassive black hole at the centre of the galaxy," *Nature*, vol. 501, no. 7467, p. 391–394, Aug. 2013. [Online]. Available: http://dx.doi.org/10.1038/nature12499

[119] J. Tarrant, G. Beck, and S. Colafrancesco, "Probing quantum gravity using high-energy astrophysics," *PoS*, vol. HEASA2018, p. 022, 2019.

[120] G. Calcagni and S. Kuroyanagi, "Stochastic gravitational-wave background in quantum gravity," *JCAP*, vol. 03, p. 019, 2021.

[121] P. Majumdar, "A possible quantum gravity hint in binary black hole merger," *Phys. Lett. B*, vol. 849, p. 138467, 2024.

[122] S. U. Islam, J. Kumar, R. Kumar Walia, and S. G. Ghosh, "Investigating Loop Quantum Gravity with Event Horizon Telescope Observations of the Effects of Rotating Black Holes," *Astrophys. J.*, vol. 943, no. 1, p. 22, 2023.

[123] M. Afrin, S. Vagnozzi, and S. G. Ghosh, "Tests of Loop Quantum Gravity from the Event Horizon Telescope Results of Sgr A*," *Astrophys. J.*, vol. 944, no. 2, p. 149, 2023.

[124] J. Kumar, S. U. Islam, and S. G. Ghosh, "Strong gravitational lensing by loop quantum gravity motivated rotating black holes and EHT observations," *Eur. Phys. J. C*, vol. 83, no. 11, p. 1014, 2023.

[125] L. Zhao, M. Tang, and Z. Xu, "The lensing effect of quantum-corrected black hole and parameter constraints from EHT observations," *Eur. Phys. J. C*, vol. 84, no. 9, p. 971, 2024.

[126] J. M. Bardeen, W. H. Press, and S. A. Teukolsky, "Rotating Black Holes: Locally Nonrotating Frames, Energy Extraction, and Scalar Synchrotron Radiation," *Astrophys. J.*, vol. 178, pp. 347–370, Dec. 1972.

[127] R. M. Wald, "Energy Limits on the Penrose Process," *Astrophys. J.*, vol. 191, pp. 231–234, Jul. 1974.

[128] M. Bhat, S. Dhurandhar, and N. Dadhich, "Energetics of the Kerr-Newman black hole by the Penrose process," *Journal of Astrophysics and Astronomy*, vol. 6, pp. 85–100, Jun. 1985.

[129] S. Parthasarathy, S. M. Wagh, S. V. Dhurandhar, and N. Dadhich, "High Efficiency of the Penrose Process of Energy Extraction from Rotating Black Holes Immersed in Electromagnetic Fields," *Astrophys. J*, vol. 307, p. 38, Aug. 1986.

[130] S. M. Wagh and N. Dadhich, "The energetics of black holes in electromagnetic fields by the penrose process," *Phys. Rep.*, vol. 183, no. 4, pp. 137–192, Nov. 1989.

[131] D. Alic, P. Moesta, L. Rezzolla, O. Zanotti, and J. L. Jaramillo, "Accurate Simulations of Binary Black Hole Mergers in Force-free Electrodynamics," *Astrophys. J.*, vol. 754, no. 1, p. 36, Jul. 2012.

[132] P. Moesta, D. Alic, L. Rezzolla, O. Zanotti, and C. Palenzuela, "On the Detectability of Dual Jets from Binary Black Holes," *Astrophys. J.*, vol. 749, no. 2, p. L32, Apr. 2012.

[133] N. Dadhich, A. Tursunov, B. Ahmedov, and Z. Stuchlík, "The distinguishing signature of Magnetic Penrose Process," *Mon. Not. Roy. Astron. Soc.*, vol. 478, no. 1, pp. L89–L94, 2018.

[134] A. Tursunov and N. Dadhich, "Fifty years of energy extraction from rotating black hole: revisiting magnetic Penrose process," *Universe*, vol. 5, no. 5, p. 125, 2019.

[135] A. Tursunov, Z. Stuchlík, M. Kološ, N. Dadhich, and B. Ahmedov, "Supermassive Black Holes as Possible Sources of Ultrahigh-energy Cosmic Rays," *Astrophys. J.*, vol. 895, no. 1, p. 14, May 2020.

[136] S. Shaymatov, P. Sheoran, R. Becerril, U. Nucamendi, and B. Ahmedov, "Efficiency of Penrose process in spacetime of axially symmetric magnetized Reissner-Nordström black hole," *Phys. Rev. D*, vol. 106, no. 2, p. 024039, Jul. 2022.

[137] G. Denardo and R. Ruffini, "On the energetics of Reissner Nordstr$\omega mgeometries,'' Phys. Lett. B, vol. \quad 45, no. \quad 3, pp.259 \quad - -262, Jul.1973.$

[138] A. Tursunov, B. Juraev, Z. Stuchlík, and M. Kološ, "Electric Penrose process: High-energy acceleration of ionized particles by nonrotating weakly charged black hole," *Phys. Rev. D*, vol. 104, no. 8, p. 084099, Oct. 2021.

[139] Z. Stuchlík, M. Kološ, and A. Tursunov, "Penrose process: Its variants and astrophysical applications," *Universe*, vol. 7, no. 11, 2021. [Online]. Available: https://www.mdpi.com/2218-1997/7/11/416

[140] M. Alloqulov, B. Narzilloev, I. Hussain, A. Abdujabbarov, and B. Ahmedov, "Energetic processes around electromagnetically charged black hole in the rastall gravity," *Chin. J. Phys.*, vol. 85, pp. 302–317, 2023. [Online]. Available: https://www.sciencedirect.com/science/article/pii/S0577907323001144

[141] A. Baez, N. Breton, and I. Cabrera-Munguia, "Energy extraction from the Reissner-Nordström de Sitter black hole," *arXiv e-prints*, p. arXiv:2406.12088, Jun. 2024.

[142] M. Alloqulov and S. Shaymatov, "Electric Penrose process and the accretion disk around a 4D-charged Einstein-Gauss-Bonnet black hole," *Eur. Phys. J. Plus*, vol. 139, no. 8, p. 731, Aug. 2024.

[143] N. Kurbonov, J. Rayimbaev, M. Alloqulov, M. Zahid, F. Abdulxamidov, A. Abdujabbarov, and M. Kurbanova, "Charged particles and penrose process near charged black holes in einstein–maxwell-scalar theory," *The European Physical Journal C*, vol. 83, no. 6, p. 506, Jun 2023. [Online]. Available: https://doi.org/10.1140/epjc/s10052-023-11691-9

[144] R. F. Penna, "Black hole meissner effect and blandford-znajek jets," *Physical Review D*, vol. 89, no. 10, May 2014. [Online]. Available: http://dx.doi.org/10.1103/PhysRevD.89.104057

[145] A. Aab *et al.*, "An Indication of anisotropy in arrival directions of ultra-high-energy cosmic rays through comparison to the flux pattern of extragalactic gamma-ray sources," *Astrophys. J. Lett.*, vol. 853, no. 2, p. L29, 2018.

[146] A. Tursunov, Z. Stuchlík, M. Kološ, N. Dadhich, and B. Ahmedov, "Supermassive Black Holes as Possible Sources of Ultrahigh-energy Cosmic Rays," *Astrophys. J.*, vol. 895, no. 1, p. 14, 2020.

[147] A. Tursunov, M. Kološ, and Z. Stuchlík, "Constraints on Cosmic Ray Acceleration Capabilities of Black Holes in X-ray Binaries and Active Galactic Nuclei," *Symmetry*, vol. 14, no. 3, p. 482, Feb. 2022.

[148] A. Eckart *et al.*, "Millimeter to X-ray flares from Sagittarius A*," *Astron. Astrophys.*, vol. 537, p. A52, 2012.

[149] K. Greisen, “End to the cosmic-ray spectrum?” *Phys. Rev. Lett.*, vol. 16, pp. 748–750, Apr 1966. [Online]. Available: https://link.aps.org/doi/10.1103/PhysRevLett.16.748

[150] J. C. McKinney and R. D. Blandford, “Stability of Relativistic Jets from Rotating, Accreting Black Holes via Fully Three-Dimensional Magnetohydrodynamic Simulations,” *Mon. Not. Roy. Astron. Soc.*, vol. 394, p. 126, 2009.

[151] R. M. Wald, *General Relativity.* Chicago, USA: Chicago Univ. Pr., 1984.

[152] S. K. Jha, M. Khodadi, A. Rahaman, and A. Sheykhi, “Superradiant energy extraction from rotating hairy Horndeski black holes,” *Phys. Rev. D*, vol. 107, no. 8, p. 084052, 2023.

[153] L. Comisso and F. A. Asenjo, “Magnetic reconnection as a mechanism for energy extraction from rotating black holes,” *Phys. Rev. D*, vol. 103, no. 2, p. 023014, Jan. 2021.

[154] W. Liu, “Energy Extraction via Magnetic Reconnection in the Ergosphere of a Rotating Non-Kerr Black Hole,” *Astrophys. J.*, vol. 925, no. 2, p. 149, Feb. 2022.

[155] S. Koide and K. Arai, “Energy extraction from a rotating black hole by magnetic reconnection in the ergosphere,” *Astrophys. J.*, vol. 682, no. 2, p. 1124, aug 2008. [Online]. Available: https://dx.doi.org/10.1086/589497

[156] M. Khodadi, “Magnetic reconnection and energy extraction from a spinning black hole with broken Lorentz symmetry,” *Phys. Rev. D*, vol. 105, no. 2, p. 023025, 2022.

[157] M. Khodadi, D. F. Mota, and A. Sheykhi, "Harvesting energy driven by Comisso-Asenjo process from Kerr-MOG black holes," *JCAP*, vol. 10, p. 034, 2023.

[158] S. Shaymatov, M. Alloqulov, B. Ahmedov, and A. Wang, "Kerr-Newman-modified-gravity black hole's impact on the magnetic reconnection," *Phys. Rev. D*, vol. 110, no. 4, p. 044005, Aug. 2024.

[159] S. M. Wagh, S. V. Dhurandhar, and N. Dadhich, "Revival of the Penrose Process for Astrophysical Applications," *Atrophys. J.*, vol. 290, p. 12, Mar. 1985.

[160] R. D. Blandford and R. L. Znajek, "Electromagnetic extraction of energy from Kerr black holes," *Mon. Not. Roy. Astron. Soc.*, vol. 179, pp. 433–456, 1977.

[161] S. S. Komissarov, "Magnetized Tori around Kerr Black Holes: Analytic Solutions with a Toroidal Magnetic Field," *Mon. Not. Roy. Astron. Soc.*, vol. 368, pp. 993–1000, 2006.

[162] R. D. Blandford and D. G. Payne, "Hydromagnetic flows from accretion discs and the production of radio jets," *Mon. Not. Roy. Astron. Soc.*, vol. 199, p. 883, 1982.

[163] A. P. Marscher *et al.*, "The inner jet of an active galactic nucleus as revealed by a radio - to - gamma-ray outburst," *Nature*, vol. 452, pp. 966–969, 2008.

[164] K. Kotera and A. V. Olinto, "The Astrophysics of Ultrahigh-Energy Cosmic Rays," *Annual Reviews*, vol. 49, no. 1, pp. 119–153, Sep. 2011.

[165] G. E. Romero, "Introduction to black holes," 5 2008.

[166] S.-J. Zhang, "Energy extraction via magnetic reconnection in Konoplya-Rezzolla-Zhidenko parametrized black holes," *Phys. Rev. D*, vol. 109, no. 8, p. 084066, 2024.

[167] S. Shaymatov, B. Ahmedov, M. De Laurentis, M. Jamil, Q. Wu, A. Wang, and M. Azreg-Aïnou, "On the Parameters of the Spherically Symmetric Parameterized Rezzolla–Zhidenko Spacetime through Solar System Tests, the Orbit of the S2 Star about Sgr A*, and Quasiperiodic Oscillations," *Astrophys. J.*, vol. 959, no. 1, p. 6, 2023.

[168] R. Ruffini and J. R. Wilson, "Relativistic Magnetohydrodynamical Effects of Plasma Accreting Into a Black Hole," *Phys. Rev. D*, vol. 12, p. 2959, 1975.

[169] K. S. Thorne, R. H. Price, and D. A. MacDonald, *Black holes: The membrane paradigm.* USA: New Haven: Yale University Press, 1986.

[170] S. Nampalliwar, S. Xin, S. Srivastava, A. B. Abdikamalov, D. Ayzenberg, C. Bambi, T. Dauser, J. A. García, and A. Tripathi, "Testing general relativity with x-ray reflection spectroscopy: The konoplya-rezzolla-zhidenko parametrization," *Phys. Rev. D*, vol. 102, no. 12, 2020.

[171] Y. Dallilar and et al., "A precise measurement of the magnetic field in the corona of the black hole binary v404 cygni," *Science*, vol. 358, no. 6368, pp. 1299–1302, 2017. [Online]. Available: http://science.sciencemag.org/content/358/6368/1299

[172] R. M. Wald, "Black hole in a uniform magnetic field," *Phys. Rev. D*, vol. 10, pp. 1680–1685, 1974.

[173] R. P. Fender, T. M. Belloni, and E. Gallo, "Towards a unified model for black hole X-ray binary jets," *Mon. Not. R. Astron. Soc.*, vol. 355, no. 4, pp. 1105–1118, Dec. 2004.

[174] K. Auchettl, J. Guillochon, and E. Ramirez-Ruiz, "New Physical Insights about Tidal Disruption Events from a Comprehensive Observational Inventory at X-Ray Wavelengths," *Astrophys. J.*, vol. 838, no. 2, p. 149, Apr. 2017.

[175] The IceCube Collaboration and et al., "Multimessenger observations of a flaring blazar coincident with high-energy neutrino IceCube-170922A," *Science*, vol. 361, no. 6398, p. eaat1378, Jul. 2018.

[176] J. C. McKinney and R. Narayan, "Disc-jet coupling in black hole accretion systems - II. Force-free electrodynamical models," *Mon. Not. Roy. Astron. Soc.*, vol. 375, no. 2, pp. 531–547, Feb 2007.

[177] M. Parsa, A. Eckart, B. Shahzamanian, V. Karas, M. Zajaček, J. A. Zensus, and C. Straubmeier, "Investigating the Relativistic Motion of the Stars Near the Supermassive Black Hole in the Galactic Center," *The American Astronomical Society*, vol. 845, no. 1, p. 22, 2017.

[178] A. K. Baczko *et al.*, "A highly magnetized twin-jet base pinpoints a supermassive black hole," *Astron. Astrophys.*, vol. 593, p. A47, 2016.

[179] M. Kino, F. Takahara, K. Hada, K. Akiyama, H. Nagai, and B. W. Sohn, "Magnetization degree at the jet base of m87 derived from the event horizon telescope data: Testing the magnetically driven jet paradigm," *Astrophys. J.*, vol. 803, no. 1, p. 30, Apr. 2015. [Online]. Available: http://dx.doi.org/10.1088/0004-637X/803/1/30